The Dissertation Committee for Arturo Gutierrez Certifies that this is the approved version of the following dissertation:

LOW-TEMPERATURE SYNTHESIS AND ELECTROCHEMICAL PROPERTIES OF ALIOVALENTLY-DOPED PHOSPHATES AND SPINEL OXIDES

Committee:

Arumugam Manthiram, Supervisor

John B. Goodenough

Llewellyn K. Rabenberg

Paulo J. Ferreira

Charles B. Mullins

LOW-TEMPERATURE SYNTHESIS AND ELECTROCHEMICAL PROPERTIES OF ALIOVALENTLY-DOPED PHOSPHATES AND SPINEL OXIDES

by

Arturo Gutierrez, B. S. Mat. Sci.

Dissertation

Presented to the Faculty of the Graduate School of

The University of Texas at Austin

in Partial Fulfillment

of the Requirements

for the Degree of

Doctor of Philosophy

The University of Texas at Austin

May 2014

Dedication

Dedicated to my beautiful wife, Annie, and our children, Alma, Gozo, Luz, Matalynn, Emma, Elaiza and Kimball.

Acknowledgements

I would like to express my sincere gratitude to Professor Arumugam Manthiram for pushing me beyond my natural capabilities. Without his guidance I could not have completed this work. Also, I would like to thank Professors John B. Goodenough, Paulo Ferreira, Llewellyn Rabenberg, and Charles B. Mullins for serving on my committee.

Additionally, financial support by the Department of Energy under Batteries for Advanced Transportation Technologies (BATT) program, National Science Foundation IGERT Fellowship, and Welch Foundation is gratefully acknowledged.

Finally, I would like to express my eternal gratitude to my extensive family who collectively nurtured me through my childhood, taught me the importance of cultivating a relationship with my Father in heaven, and guided me to manhood.

LOW-TEMPERATURE SYNTHESIS AND ELECTROCHEMICAL PROPERTIES OF ALIOVALENTLY-DOPED PHOSPHATES AND SPINEL OXIDES

Arturo Gutierrez, Ph. D.

The University of Texas at Austin, 2014

Supervisor: Arumugam Manthiram

Lithium-ion batteries are being intensely pursued as energy storage devices because they provide higher energy and power densities compared to other battery systems such as lead-acid and nickel-metal hydride batteries. This dissertation (i) explores the use of a low-temperature microwave-assisted synthesis process to obtain aliovalently-doped lithium transition-metal phosphates and lower-valent vanadium oxide spinels, some of which are difficult to obtain by conventional high-temperature processes, and (ii) presents an investigation of the electrochemical properties of the aliovantly-doped phosphate cathodes and doped lithium manganese oxide and oxyfluoride spinel cathodes in lithium-ion batteries.

Following the introduction and general experimental procedures, respectively, in Chapters 1 and 2, Chapter 3 first focuses on understanding of how the inductive effect and structural features in lithium transition-metal borate, silicate, and phosphate cathodes affect the $M^{2+/3+}$ redox energies. It is found that the magnitude of the voltages delivered by the polyanion cathodes can be predicted based simply on the coordination of the transition-metal ion. Furthermore, the differences in the voltages delivered by the

phosphates and pyrophosphates are explained by considering the resonance structures and their contribution to the covalency of the polyanion.

Chapter 4 presents a low-temperature microwave-assisted solvothermal process to substitute 20 atom % V^{3+} for Mn^{2+} in $LiMnPO_4$. It is shown that the solubility of vanadium in $LiMnPO_4$ decreases upon heating the doped samples to ≥ 575 °C, demonstrating the importance of employing a low-temperature process to achieve aliovalent doping in $LiMnPO_4$. It is further demonstrated that by increasing the vanadium content in the material, the discharge capacity in the first cycle could be increased without any additional carbon coating. Subsequent X-ray absorption spectroscopy data reveal that the better performance is facilitated by enhanced Mn-O hybridization upon incorporating vanadium into the lattice.

Chapter 5 explores the influence of various factors, such as the oxidation state of Mn, electronegativity of the dopant cation M^{n+}, and the dissociation energy of M-O bond, on the electrochemical properties of cation-doped oxide and oxyfluoride spinel cathodes. As an extension, Chapter 6 presents the effect of processing conditions on the surface concentration of the dopant cation M^{n+}.

Chapter 7 presents an extension of the low-temperature microwave-assisted synthesis process to obtain AV_2O_4 (Mg, Fe, Mn, and Co) spinel oxides. The method is remarkably effective in reducing the synthesis time and energy use due to the efficiency of dielectric heating compared to conventional heating. The ability to access V^{3+} is facilitated by the relative positions of the energy levels of the cations in solution, which is lower than that in the solid, and the use of a strong reducing solvent like TEG.

Finally, Chapter 8 provides a summary of the salient findings in this dissertation.

Table of Contents

List of Tables

List of Figures

Chapter 1: Introduction

1.1 Lithium-ion batteries

Every electrochemical system contains two electrodes that are separated by an electrolyte and connected by an external circuit. A lithium-based battery is an electrochemical system with at least one electrode containing lithium. Lithium is the most electronegative metal (~ -3.0 V vs. SHE), which translates into a high cell voltage when matched with certain cathodes. Furthermore, lithium is the lightest metal (0.534 g cm^{-3}) making it an anode of high specific capacity (3.86 Ah/g). These two key factors pushed early research to focus towards using lithium metal as an anode. However, due to dendritic growth (needlelike lithium crystals) on the surface causing difficulties with cycle life and safety, the research was soon redirected.[1-3] What arose from the research that followed were intercalation structures used as "hosts" for lithium.[4-6]

The lithium-ion battery, as we know it today, made its breakthrough when carbonaceous materials were exploited as anodes. The commercialization of lithium-ion batteries soon followed when both Sony and Moli announced cells based on $LiCoO_2$ and petroleum coke. By 2000 lithium-ion batteries accounted for more than 90 % of the rechargeable battery market and more than 60 % of total sales in portable batteries.[7] Although lithium-ion batteries have seized the portable electronics market, they still fall short of meeting demands dictated by "emerging markets". For example, the demand to exploit renewable energy can only transpire when Li-ion technology improves beyond its current state. Furthermore, concerns about limited fossil-fuel supplies and increased pollution are driving the transportation sector towards electrification.

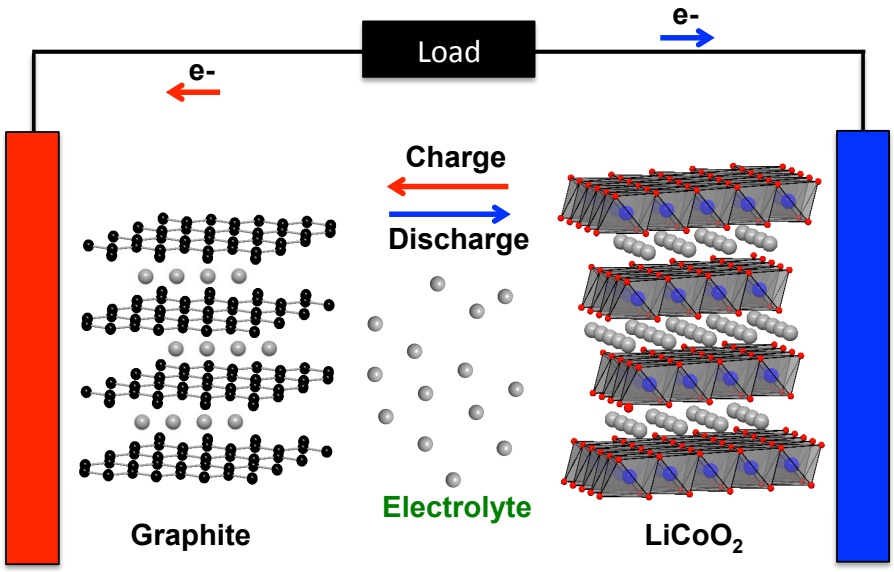

Figure 1.1. Schematic illustration of the charge/discharge process in a lithium-ion battery consisting of graphite as the anode and $LiCoO_2$ as the cathode.

1.1.1 Principle of operation

In a battery, electrical energy is generated by conversion of chemical energy through simultaneous redox reactions that occur at the anode (graphite) and cathode (intercalation or host structure). The anode is designated as the negative electrode, and the anode reactions occur at lower electrode potentials in comparison to that at the cathode (positive electrode). This designation changes depending on whether the battery is being charged or discharged. For the sake of this discussion, cathode and anode will be used in terms of a Galvanic cell (discharging battery). The charging process of a lithium-ion battery involves the extraction of lithium ions from the cathode host structure and then flowing through the electrolyte to the anode (See Figure 1.1). Simultaneously, electrons flow through an external circuit from the cathode to the anode to maintain charge neutrality. This process is reversible in rechargeable (secondary) batteries.

The net useful energy available from a given electrochemical reaction is given by:

$$\Delta G = -nFE \tag{1.1}$$

where n is the number of electrons transferred per mole of reactants, F is the Faraday constant (equal to the charge of 1 mole of electrons), and E is the voltage of the cell.
The amount of electricity produced, nF, is determined by the amount of materials available for reaction and can be thought of as a capacity factor; the cell voltage can be considered as an intensity factor.

The cell voltage is unique for each reaction couple. Figure 1.2 shows a schematic energy diagram of a cell at open circuit. The difference in the lithium-chemical potential between the cathode ($\mu_{Li(c)}$) and anode ($\mu_{Li(a)}$) at equilibrium is the open-circuit voltage V_{oc} of a lithium-ion battery:

$$V_{oc} = \frac{\mu_{Li(c)} - \mu_{Li(a)}}{F} \tag{1.2}$$

where F is the Faraday constant. Special consideration should be taken to ensure that the redox energies of the cathode (E_c) and anode (E_a) lie within the bandgap (E_g) of the electrolyte (shown in Figure 1.2) to avoid unwanted reduction or oxidation reactions of the electrolyte.

When a current is drawn, the cell moves away from equilibrium and the voltage drops off (electrode polarization) due to kinetic limitations associated with the reactions occurring. Battery electrodes undergo a series of steps including charge-transfer and

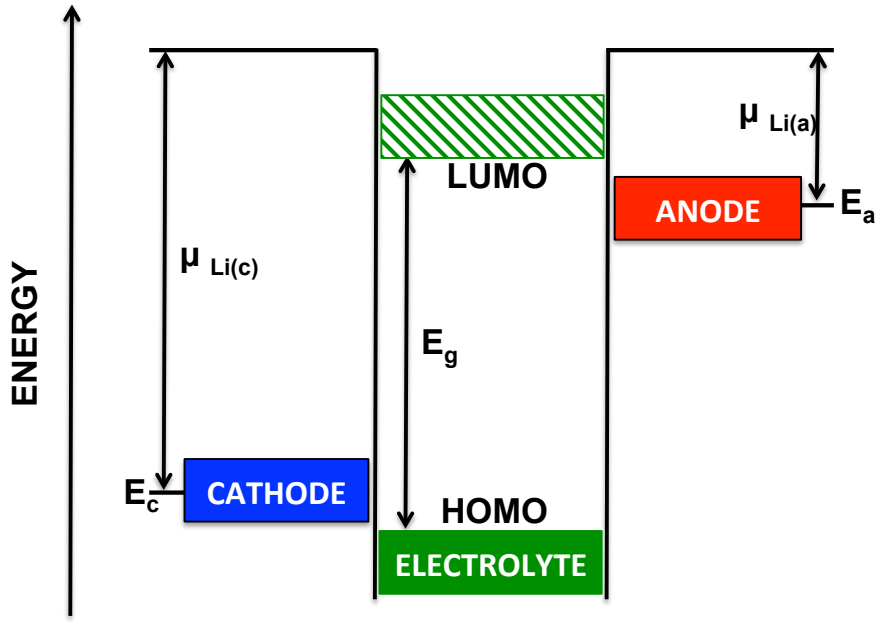

Figure 1.2. A schematic energy diagram of a lithium-ion battery at open circuit. HOMO refers to the highest occupied molecular orbital; LUMO refers to the lowest unoccupied molecular orbital in the electrolyte.

charge-transport reactions. The rates of the individual steps determine the kinetics of the electrode (and therefore the battery). The total polarization of an electrode has three contributing kinetic effects (activation polarization, ohmic polarization, and concentration polarization) and is given by:

$$\eta = E_{oc} - E_T \tag{1.3}$$

where E_{oc} is the open-circuit voltage of the cell and E_T (terminal voltage) is the cell voltage with current flowing.

Activation polarization is related to the charge-transfer reactions taking place at the electrode/electrolyte interfaces of the anode and cathode. In treating this type of kinetics, it is assumed that the rate-limiting step is the dissociation of an activated complex. The rate of a charge-transfer reaction is given by the Butler-Volmer equation:

$$i = i_0 exp\left(\frac{\alpha F \eta}{RT}\right) - exp\left(\frac{(1-\alpha) F \eta}{RT}\right) \quad (1.4)$$

where η is the polarization (or overpotential; see Equation 1.3), and α is the transfer coefficient, which describes how much of the overpotential is used at the electrode/electrolyte interface in lowering the free energy barrier for charge-transfer to occur. The exchange current density, i_0, is the current in the absence of net electrolysis and at zero potential. For an illustration, consider a cell at equilibrium (open circuit). Electron transfer still occurs at the electrode/solution interface of both the anode and cathode but is completely balanced ($i_a = i_c$). The exchange-current density is this "background" current which is used to normalize the net current. The Tafel equation is used to describe the activation polarization and is derived from the Butler-Volmer equation (Equation 1.4):

$$\eta = a - b\left[log\left(\frac{i}{i_0}\right)\right] \quad (1.5)$$

where a and b are constants.

Ohmic polarization represents the total resistance felt by the charge carriers as they travel between the two electrodes. There is an electronic portion due to the resistivity of battery components (electrodes, current collectors, terminals, etc.) and an ionic portion due to the resistance of the electrolyte, materials used to construct the

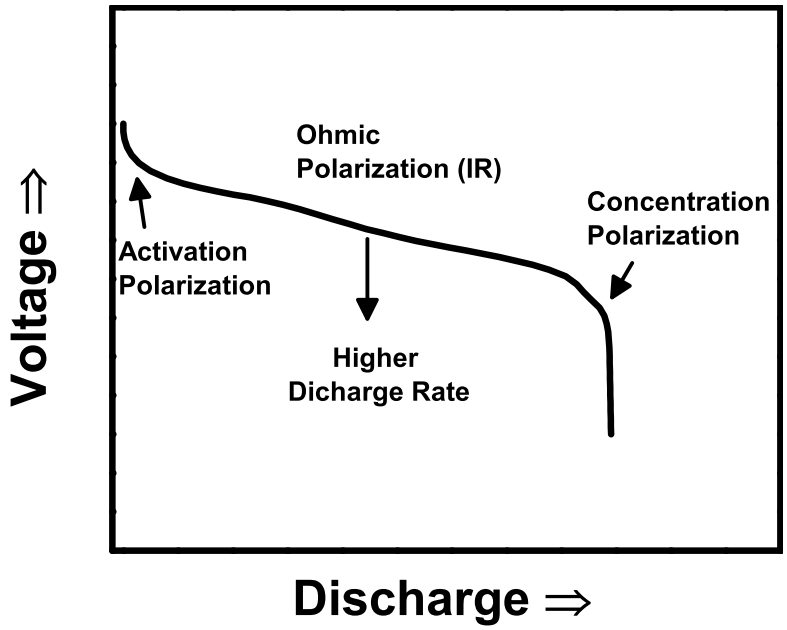

Figure 1.3. Typical discharge curve of a battery, demonstrating the influence of the various types of polarization.

electrodes, surface films, and contact between particles of the active mass. As the name suggests, an Ohm's law relationship is used to describe this type of polarization:

$$\eta = IR \tag{1.6}$$

Concentration polarization arises from the differences between the rate of reaction on the electrode and the rate of ion migration through the electrolyte to the electrode surface. With an assumption of limited diffusion in the electrolyte, the concentration polarization can be expressed as:

$$\eta = \left(\frac{RT}{n}\right) ln\left(\frac{C}{C_0}\right) \tag{1.7}$$

where the concentration of the ion at the electrode surface and in the bulk are, respectively, C and C_0. The discharge curve of a battery, shown in Figure 1.3, reveals the influence of the various types of polarization.

1.1.2 Cathode materials

The energy density of a battery is the product of its capacity and its potential. The energy density of lithium-ion batteries is limited largely by the cathode materials.[8] Accordingly, our emphasis is on finding cathodes with larger capacities and/or greater operating potentials. To achieve larger capacities we need to identify materials with the capability of reversibly accepting more than one lithium/electron per transition-metal ion. Maximizing the cell voltage involves decreasing the chemical potential of lithium ($\mu_{Li(c)}$) in the cathode, which can be done by tailoring the energy of the redox couple in a couple of ways. First, the oxidation state of the transition-metal ion should be high enough since the redox energy is lower (or the operating voltage is higher) for higher oxidation states. Another approach for tuning the redox energy involves modifying the iono-covalent character of the transition metal-oxygen bond either through the inductive effect or structural features.[9-12]

Although increasing the energy density is of prominent importance, consideration must be given to other key requirements such as the following:

- The electrodes should be chemically compatible with the electrolyte during cycling.
- All materials used for battery components should be lightweight, environmentally benign, and inexpensive.

- The electrodes should have good electronic conductivity and lithium-ion conductivity.

The cathode materials relevant to this work are introduced in the discussion that follows.

1.1.2.1 Spinel structure

Spinel oxides have the general formula AB_2O_4, (space group F*d-3m*) where the A and B ions are in 8a tetrahedral and 16d octahedral sites (as shown in Figure 1.4), respectively. The interest in spinel electrodes for lithium-ion batteries first came after it

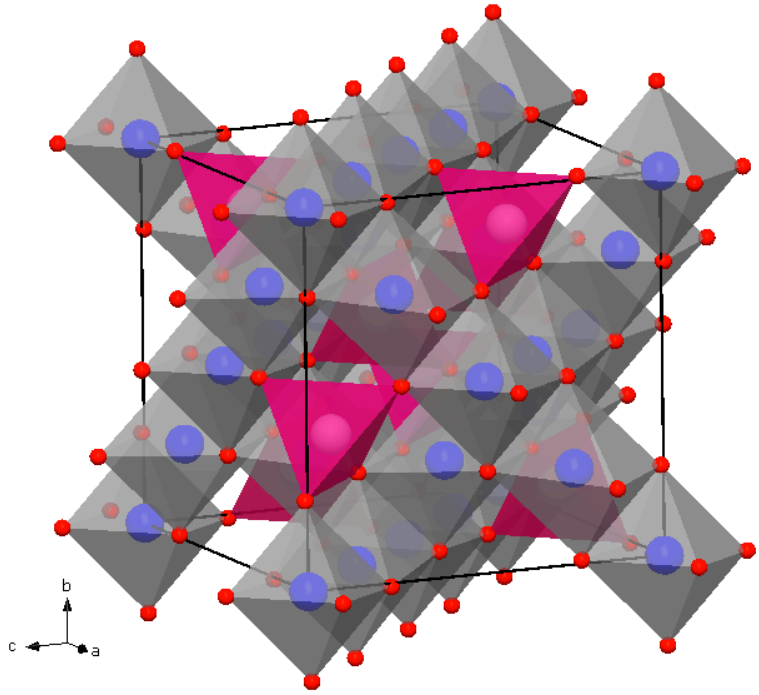

Figure 1.4. Crystal structure of spinel $LiMn_2O_4$. The pink and grey polyhedra indicate the tetrahedral and octahedral sites, respectively. Oxygen atoms are shown in red.

was shown to provide good structural stability during the charge-discharge of Fe_3O_4,[13] Mn_3O_4,[14] and $LiMn_2O_4$.[14, 15] In general, metal oxides with structures that have cubic-close-

packed (ccp) oxygen arrays, like the spinel structure, are more stable to lithium insertion/extraction than hexagonally-close-packed (hcp) arrays.[16] The structure also provides a path for high electrical conductivity through direct B-B interactions facilitated by edge sharing between BO_6 octahedra. Likewise, the three-dimensional structure provides an uninterrupted interstitial pathway for Li^+-ion diffusion through the structure, which enables high-rate capability. $LiMn_2O_4$ is most appealing among the LiM_2O_4 spinels because along with the properties described above, Mn is inexpensive and less toxic than Co and Ni.

A total of two lithium ions can be inserted into the Mn_2O_4 spinel framework, which results in two distinct voltage plateaus during cycling. The first lithium is inserted into the 8a tetrahedral sites at around 4 V in a two-step process that occurs due to the ordering of the lithium ions on one half of the 8a tetrahedral sites. The overall reaction occurs at a high voltage because the lithium ions must move between two 8a sites via an energetically unfavorable 16c octahedral site. The lithium ions are then placed in 16c sites upon insertion beyond $1 < x \leq 2$ in $Li_xMn_2O_4$. Electrostatic interactions between lithium ions in 8a and 16c sites, which share faces, force the lithium ions in 8a tetrahedral sites into vacant 16c sites.[17] A first-order phase transition from cubic $LiMn_2O_4$ to tetragonal $Li_2Mn_2O_4$ occurs due to the Jahn-Teller distortion associated with Mn^{3+} ions on inserting the second lithium.

Lithium manganese oxide spinel $LiMn_2O_4$, however, has two problems associated with its redox center. The first vulnerability is chemical in nature and is related to manganese disproportionation that occurs as shown below:

$$2Mn^{3+}{}_{(solid)} \rightarrow Mn^{4+}{}_{(solid)} + Mn^{2+}{}_{(solution)} \qquad (1.8)$$

The Mn^{2+} in solution represents capacity lost as the amount of Mn^{3+} available for the redox reaction is lowered as a result. Another damaging consequence of the Mn^{2+} in solution is that it travels to the anode and gets reduced on the anode surface, causing a rise in impedance and fast capacity fade during cycling. The second difficulty is rooted in the electronic structure of high-spin Mn^{3+}: $t_{2g}^{3}e_{g}^{1}$, where the lone ground state is doubly degenerate. The MnO_6 octahedra distort along one of the crystallographic axes to eliminate any orbital degeneracy and lower the overall energy. The distortion results in a macroscopic cubic to tetragonal transition and degradation of the structural integrity of the material.

Both of these instabilities have been attributed for the inherent capacity fade of $LiMn_2O_4$ cathode materials. One effective technique in improving the performance has been to substitute either Li^+ and/or other cations for Mn, but at the cost of lowering the capacity. The lower capacity comes as a result of less Mn^{3+} available upon substitution. Fluorine has been substituted for oxygen to make up for the lost capacity. This technique reduces Mn^{4+} in the structure to Mn^{3+} on account of fluorine being monovalent and oxygen being divalent.

1.1.2.2 Polyanion cathodes

$LiMPO_4$ (M = Mn, Fe, Co, and Ni) has the ordered olivine structure, with the space group P*nma*. As shown in Figure 1.5, the P^{5+} ions occupy tetrahedral sites; the M^{2+} and Li^+ ions both occupy the octahedral sites. The oxide ions adopt a slightly distorted, hexagonal-close-packed (hcp) arrangement. The MO_6 octahedra share four edges with other MO_6 octahedra in the b-c plane. One MO_6 octahedron shares edges with two LiO_6 octahedra. The LiO_6 octahedra share edges along the b-axis. The PO_4 groups share two edges with LiO_6 octahedra and one edge with a MO_6 octahedron.

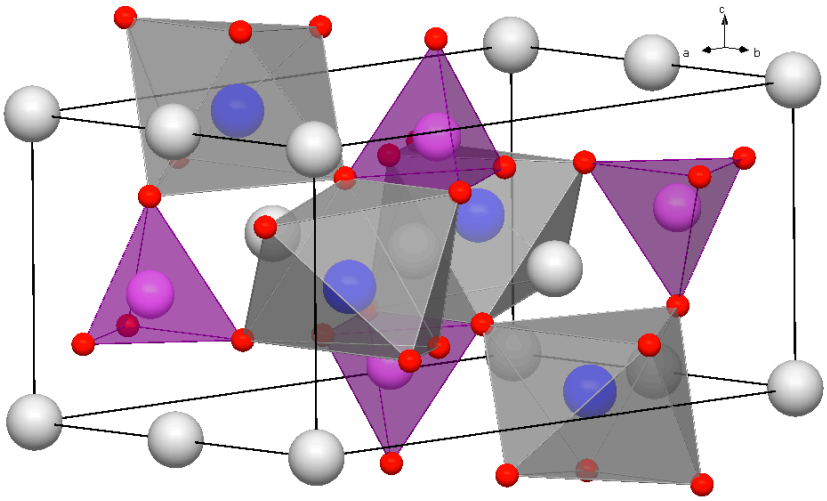

Figure 1.5. Crystal structure of olivine $LiMPO_4$ (M = Fe, Mn, Co, and Ni). The purple and grey polyhedra indicate the tetrahedral and octahedral sites, respectively. Oxygen is shown in red; lithium is shown in light grey.

$LiFePO_4$ has excellent thermal stability due to the strong covalent bonding in the PO_4 polyanion. The strong bonding is also credited for producing higher voltages in comparison to oxides with the same $M^{2+/3+}$ redox couple. $LiFePO_4$ delivers its capacity (theoretical ~ 170 mAh/g) at ~ 3.5 V as a two-phase reaction occurs between $LiFePO_4$ and $FePO_4$. Because these two phases do not have any significant Fe^{3+}/Fe^{2+} mixing, the material has poor electronic conductivity. The olivine structure is also kinetically limited by its one-dimensional diffusion of Li^+ ions. Synthesizing nanoparticles and coating the nanoparticles with carbon can overcome the conductivity problems.

Both $LiCoPO_4$ and $LiNiPO_4$ deliver the capacities at voltages near or above the electrolyte LUMO so they have not been studied elaborately. $LiMnPO_4$ is a better candidate for investigation with a discharge potential at 4.1 V, which is well within the band gap of the electrolyte. $LiMnPO_4$ would provide a higher energy density than

$LiFePO_4$ on account of its higher voltage but it is hindered by an even lower conductivity than $LiFePO_4$.

In addition to the olivine structure, new polyanion chemistries are being studied with the hopes of exploiting the higher discharge potential inherent in these materials. Among these new chemistries are the silicates Li_2MSiO_4 and pyrophosphates $Li_2MP_2O_7$ (M = Fe, Mn, Co, and Ni). These two materials offer the possibility of extracting more than one lithium per transition metal, which would increase the theoretical capacity of the former to ~ 330 mAh/g and the latter to ~ 220 mAh/g. $LiMBO_3$ is another polyanion chemistry that offers a high capacity (~ 200 mAhg/g) on account of it having a light polyanion unit (BO_3).

1.1.3 Anode materials

Since 1990, when Dahn *et al*.[18] reported that the decomposition of electrolyte solvents formed a protective film (SEI layer) on carbonaceous anodes, graphite has been the anode of choice for lithium-ion batteries. Graphite anodes are attractive because their redox activity with Li^+ ions is well below the cathodic stability limit of all relevant electrolyte solutions. In addition, they have exhibited adequate cycling performance due to their dimensional stability. The insertion/extraction of lithium into graphite can be written as below:

$$C_n + Li^+ + e^- \rightleftharpoons Li_xC_n \qquad (1.9)$$

One drawback for Li-intercalated graphite is the fragility of the material, making it vulnerable to cracking and exfoliation. The problem occurs when co-intercalated solvent molecules (with Li^+ ions) are subsequently reduced and form ionic compounds

and gases that damage the particles.[19] Furthermore, surface films are known to stress and crack during prolonged cycling, especially at elevated temperatures.

Several families of materials have been identified as potential candidates to replace the graphite anode, which include Sn and Si-based alloys and composites,[20] metal-oxides (for conversion reactions),[21] and $Li_4Ti_5O_{12}$.[22] Each of these candidates faces some challenges in replacing graphite. For instance, although the $Li_4Ti_5O_{12}$ spinel has demonstrated high stability and very fast discharge/charge rates, its limited capacity (~ 160 mAh/g vs. ~ 372 mAh/g for graphite) and higher operating voltages (~1.5 V vs. L/Li^+) make it almost irrelevant for high-energy density applications. Furthermore, although an anode that undergoes a conversion reaction offers much higher capacities than graphite, they also pose additional problems such as a large voltage difference between the charge and discharge processes and enhanced side reactions with the electrolyte because of their need for nanostructuring and high surface area.[23] Alloy anodes offer much higher capacities when compared to graphite, but the volume changes can reach as high as 400% upon lithiation as in the case of Si, destroying the structural integrity of the material. Significant research is ongoing to overcome these challenges, but for now, graphite remains the anode of choice.

1.1.4 Electrolytes

The electrolyte serves as the medium for the transfer of ionic charge between a pair of electrodes. Conceptually, the electrolyte should not undergo any net chemical changes during the operation of the battery, and all faradaic processes are expected to occur within the electrodes. The range (in volts) between oxidative and reductive decomposition limits (known as the bandgap (see Figure 1.2) or "electrochemical window") of the electrolyte gives a measure of its stability. Therefore, a wide

electrochemical window is optimal to avoid electrolyte decomposition during cycling. An electrolyte should be a good ionic conductor to facilitate fast ion transport and it should be an electronic insulator to minimize the amount of self-discharge. All electrolyte components should be inert to other cell components at all stages of cycling. They should also be robust against electrical, mechanical, and thermal abuses.

The majority of the electrolytes are solution-types that are in a liquid state in the service temperature range. These types of electrolyte consist of salts dissolved in nonaqueous solvents because aqueous solvents with active protons are reactive towards lithium.[7]

An ideal electrolyte solvent should have a high dielectric constant (a measure of its ability to dissolve salts at high concentrations). In addition, an electrolyte solvent should have a low melting point and a high boiling point guaranteeing that it remains in the liquid state in a wide temperature range. Lastly, to provide good safety, the solvent should have a high flash point.

In connection to the solvent properties, the electrolyte solute should be highly soluble in the solvent. After solvation, the ions should be highly mobile and remain inert. Special consideration should be given to ensure that the anion is stable against oxidative decomposition at the cathode and to thermally induced reactions with the electrolyte solvent.

A wide range of polar solvents has been investigated for use in nonaqueous electrolytes. The majority of them are either organic esters or ethers. Ethylene carbonate mixed with diethyl carbonate or dimethyl carbonate is widely used as the solvent in combination with $LiPF_6$ as the salt due to a combination of its well-balanced properties.[7] Nevertheless, carbonate-based electrolytes are flammable and undergo oxidation above

about 4.5 V. Consequently alternative electrolytes are being investigated which include: polymer electrolytes,[24] ionic liquids,[25] and inorganic solid electrolytes.[26]

1.1.5 Separators

Separators play a key role in all batteries. They are placed between the cathode and anode to prevent electrical short circuits. They must be permeable to the ionic charge carriers allowing the flow of charge in an electrochemical cell. When selecting the best separator for a particular battery or application, there are a number of additional factors to consider as given below:[27]

- Electronically insulating
- Minimal ionic resistance
- Mechanical stability for easy handling
- Chemical resistance to degradation
- Effective in preventing migration of other species between the electrodes
- Readily wetted by the electrolyte
- Uniform thickness

Separators that are used in batteries are either made of nonwoven fabrics or microporous films. When the battery operates near ambient temperatures, the separator can be made of organic or inorganic materials. In alkaline batteries, the separators are either polymer films or regenerated cellulose. Lithium-ion batteries using organic electrolytes use microporous polyolefin films.

1.2 OBJECTIVES

The task to improve energy storage materials/devices and the efficient distribution of that stored energy is one of the major technological challenges of this century. The energy density of lithium-ion batteries must increase significantly, the cost must be

reduced, and the cycle life and safety must be improved if they are to compete with gasoline in the transportation sector.[8] Our success in this regard greatly depends on improving our fundamental understanding of the structure-composition-property relationships and utilizing the knowledge to develop new low-cost, long-life, safe, high-energy density materials.

As pointed out above, the polyanion cathodes offer important safety advantages and have the potential to insert/extract reversibly more than one lithium ion per transition-metal ion. With an aim to understand the intricacies involved in tuning the redox energies, after providing an introduction and the general experimental procedures, respectively, in Chapters 1 and 2, Chapter 3 focuses on reviewing the structural features of a variety of polyanion cathodes (*e.g.*, $LiMBO_3$, Li_2MSiO_4, $LiMPO_4$, $Li_2MP_2O_7$ with M = Fe, Mn, Co, and Ni) and understanding the differences/variations in the $M^{2+/3+}$ redox energies.

Equally important to our success in designing new materials is our ability to exploit novel low-temperature synthesis approaches to stabilize metastable compositions that are otherwise inaccessible by conventional high-temperature processes. Accordingly, Chapter 4 focuses on the use of microwave-assisted solvothermal (MW-ST) synthesis to aliovalently dope $LiMnPO_4$ to give $LiMn_{1-3x/2}V_x\square_{x/2}PO_4$ ($0 < x \leq 0.20$) and on understanding their electrochemical performance.

Because of the several intrinsic advantages of spinel cathodes (e.g., lower cost and high rate capability), they are employed in both Chevy Volt and Nissan Leaf. With an aim to enhance our understanding of the role of cationic and anionic substitutions in spinel cathodes, Chapter 5 focuses on fluorine-substituted $Li_{1.1}Mn_{1.8}M_{0.1}O_4$ (M = Al, Ti, Cr, Fe, Co, and Ni). The analysis of these samples includes a look at how the basic chemical properties of the dopant M affect the electrochemical performance of the

material. As an extension of the spinel cathodes, Chapter 6 describes the role of surface segregation in the performance of spinel cathode materials.

As an extension of the exploitation of low-temperature synthesis approaches, Chapter 7 focuses on the use of MW-ST process to form spinel MV_2O_4 (Mg, Mn, Fe, and Co) that are difficult to synthesize by conventional high-temperature synthesis in reducing atmospheres.

Chapter 2: General experimental procedures

2.1 Materials Synthesis

2.1.1 Microwave-assisted solvothermal process

$LiMn_{1-3x/2}V_x\square_{x/2}PO_4$ ($0 \leq x \leq 0.20$) samples were prepared by mixing appropriate amounts of lithium hydroxide monohydrate (Alfa Aesar, 98%), manganese actetate tetrahydrate (Acros Organics, 99%), phosphoric acid (Fisher, 85%), and vanadium triisopropoxide oxide (Alfa Aesar, 96%) in tetraethylene glycol (Alfa Aesar) and stirring continuously until the precursors were dissolved. The solution was then transferred into quartz vessels, sealed, and placed in the microwave (Anton Paar Synthos 3000) where a constant power of 600 W at a frequency of 2.45 GHz was applied until a temperature of 280 °C was reached in the vessel (generally took ~ 30 min to reach maximum temperature). After reaching the desired temperature, the reaction was allowed to occur at that temperature for 15 – 20 min. The pressure inside of the quartz vessels reached different levels (20 – 70 bar) depending on the amount of vanadium precursor used in the reaction (higher pressures for larger amounts of the vanadium precursor).

After the cooling cycle was completed, the products were sonicated, centrifuged, and washed with acetone until the decanted solution was clear. The samples were then dried in air overnight before any additional characterization was carried out. The un-doped $LiMnPO_4$ powder was white in color and the color changed from beige to a light brown with increasing amounts of vanadium doping ($x = 0.05 – 0.20$).

AV_2O_4 (A = Mg, Fe, Mn, and Co) samples were prepared by first mixing vanadium triisopropoxide oxide (Alfa Aesar, 96%) with the appropriate divalent metal acetate tetrahydrate (Mg, Fe, Mn, or Co) in TEG (Alfa Aesar) and stirring continuously for several hours to allow the precursors to dissolve. The solution was then placed in an

Anton-Paar Monowave 300 microwave synthesis reactor, where it was heated as fast as possible to 300 °C (generally reached in 2 min). The mixture was stirred during the reaction at 800 rpm with a magnetic stir bar and held at the maximum temperature of 300 °C for 30 min while being monitored by an infrared temperature sensor. The pressure inside of the vessels generally stayed between 15 – 25 bar. After the cooling cycle was completed, the products were sonicated, centrifuged, and washed with acetone until the decanted solution was clear. The samples were then dried in air overnight before post-heating to temperatures between 450 – 900 °C in a flowing 5 % H_2 – 95 % Ar or 100 % Ar atmosphere. The length of time for the post-heating treatment varied between 3 – 48 h.

2.1.2 Solid-state synthesis

The cation-doped $Li_{1.1}Mn_{1.8}M_{0.1}O_4$ and $Li_{1+x}Mn_{2-2x}M_xO_4$ (M = Al, Ti, Cr, Fe, Co, and Ni) spinel oxides were synthesized by firing required amounts of Li_2CO_3 and Mn_2O_3 with Al_2O_3, TiO_2, Cr_2O_3, Fe_2O_3, Co_3O_4, or NiO at 800 °C for 48 h in air. Fluorine was incorporated by firing the $Li_{1.1}Mn_{1.8}M_{0.1}O_4$ or $Li_{1+x}Mn_{2-2x}M_xO_4$ spinel oxide with a required amount of NH_4HF_2 at 450 °C for 5 h in air. In general, an excess amount (~ 50 % excess for Cr-doped samples and ~ 10 % excess for all other doped samples) of NH_4HF_2 was needed to reach the amount of fluorination desired for each of the fluorinated series.

2.2 MATERIALS CHARACTERIZATION

2.2.1 X-ray diffraction (XRD)

X-ray powder diffraction (XRD) data were collected with a Rigaku Ultima IV and Philips X-ray diffractometer 3550 (both with Cu Kα radiation).

2.2.2 Scanning electron microscopy (SEM)

The morphology of the samples was investigated with JEOL JSM-5610 and Hitachi S5500 scanning electron microscopes (SEM). Elemental dot maps were taken on the Hitachi S5500 equipped with energy dispersive spectroscopic (EDS) capability.

2.2.3 Inductively coupled plasma-atomic emission spectrometry (ICP-AES)

Elemental ratios in the samples were analyzed with a Varian 715-ES inductively coupled plasma – atomic emission spectrometer (ICP-AES). Each sample was fully dissolved in concentrated acid (HCl : HNO_3 = 3 : 1) and then diluted with deionized water to fall within the concentration range of prepared standard solutions. The calibration of the instrument was achieved with four standard solutions for each element tested.

2.2.4 Determining the amount of manganese dissolution

The active material was soaked for 7 days at 55 °C in an electrolyte consisting of 1 M $LiPF_6$ in 1:1 ethylene carbonate/diethyl carbonate. Afterwards, the remaining material was filtered out while the electrolyte/deionized water solution was used to determine the amount of manganese dissolved in the electrolyte by inductively coupled plasma (ICP) analysis.

It has been shown that Mn dissolution occurs at both the charged and discharged states. For example, Gummow *et. al.*[28] demonstrated that Mn dissolution occurs at lower potentials due to the higher concentrations of Mn^{3+}, while Jang *et. al.*[29] determined that larger amounts of Mn dissolution occur at higher states of charge (SOC) due to the oxidative reactions that occur with the conductive additive (carbon) used to make the cathode. Since the purpose of this test was to understand the role of the dopants on Mn

dissolution, we chose to test the Mn dissolution of the samples in the fully discharged state.

2.2.5 Determining the amount of fluorine substitution

The average oxidation state of manganese was determined by a redox titration involving sodium oxalate ($Na_2C_2O_4$) and potassium permanganate ($KMnO_4$). The fluorine contents were calculated based on the oxidation state of manganese, employing charge neutrality and assuming the total anion (O + F) content to be 4.0. This assumption is reasonable as the oxygen non-stoichiometric range in spinels is negligible.[30]

2.2.6 Fourier transform infrared (FTIR) spectroscopy

Fourier transform infrared (FTIR) spectra were collected with a PerkinElmer BX FTIR with pellets prepared by grinding and pressing samples with dried KBr powder.

2.2.7 Secondary-ion mass spectroscopy (SIMS)

The depth profiles of elemental concentrations were examined by time-of-flight – secondary ion mass spectroscopy (TOF-SIMS) (TOF.SIMS 5 instrument, ION-TOF GmbH, Germany 2010). Shallow depth profiles of the elements were recorded in dynamic SIMS mode using the primary ion gun (Bi_1^+ at 30 keV energy and 3.1 pA measured sample current) for both sputtering and analysis. All profiles were reconstructed from the initial TOF-SIMS data files using a circular region of interest of 15 μm diameter centered on the squared 20 x 20 μm^2 acquisition area to avoid the inherent edge effects of dynamic SIMS profiling. TOF-SIMS was performed under UHV (base pressure of about 1 x 10^{-9} mbar) on samples consisting of cathode powders that were compactly attached onto a carbon tape. All detected secondary ions had positive polarity.

2.2.8 X-ray absorption spectra (XAS)

V-edge/Mn-edge X-ray absorption near edge spectroscopy (XANES) data were collected in transmission mode at beamline X18A at the National Synchrotron Light Source of Brookhaven National Laboratory with a Si (111) double-crystal monochromator. Reference spectra of a metallic (V and Mn) foil were simultaneously collected with the corresponding spectra for energy calibration.

For soft X-ray absorption spectroscopy (XAS) characterization, including Mn/V *K*-edge and O *K*-edge, $LiMn_{1-3x/2}V_x\square_{x/2}PO_4$ cells were electrochemically cycled to certain stages. Afterwards, the cells were disassembled and the cathode materials were rinsed with DMC and dried in a glove box to remove any residue. The cathode materials were pressed onto conducting carbon tapes and loaded into our special sample transfer chamber inside the argon glove box. The sample transfer chamber was then sealed and mounted directly onto the ultra-high vacuum XAS characterization chamber to avoid any air-exposure effects.[31] The soft XAS was performed at Beamline 8.0.1 of the Advanced Light Source (ALS) in Lawrence Berkeley National Laboratory (LBNL).[32] The undulator and spherical grating monochromator supply a linearly polarized photon beam with resolving power up to 6000. The experimental energy resolution is better than 0.2 eV. Experiments were performed at room temperature and with the linear polarization of the incident beam at 45 ° to sample surfaces. All the spectra were normalized to the beam flux measured by the upstream gold mesh.

2.2.9 Electrochemical characterization

2.2.9.1 Electrode preparation

Each composite electrode weighed between 5 and 8 mg and was rolled into thin sheets and punched out into 0.64 cm^2 circular electrodes. The electrodes were dried in a vacuum oven at 115 °C overnight. The electrodes were then transferred into an Ar-filled glovebox where CR2032 coin cells were assembled with metallic lithium as the anode, Celgard polypropylene separator, and 1 M $LiPF_6$ in 1:1 diethyl carbonate/ ethylene carbonate electrolyte. The composite electrode was prepared with slightly different ratios of active material, conductive carbon, and binder depending on the material being tested. The details are as follows.

Electrodes made with spinel materials were prepared by mixing the active material powder (75 wt. %) with conductive carbon (Denka black - 20 wt. %) and polytetrafluoroethylene (PTFE) binder (5 wt. %).

Electrodes made with phosphate materials were prepared by mixing the active material (75 wt. %) with conductive carbon (Super P - 12.5 wt. %) and teflonated acetylene black (TAB) (12.5 wt. %).

2.2.9.2 Cycle performance and rate capability tests

The electrochemical data were collected with an Arbin battery cycler. The current rate and voltage windows were dependent on the sample being tested. The cycle performance was evaluated by charging/discharging at a fixed current density.

2.3 COMPUTATIONS

2.3.1 Calculating the electrostatic site potential for the transition-metal ions

The process for calculating the electrostatic site potentials for each of the systems was performed with the General Utility Lattice Program (GULP) and included a

verification of the potential parameters used from the literature. The Buckingham potential parameters taken from reported literature were verified by reproducing the experimental unit cell parameters and then used to calculate the electrostatic site potential. The results of the structural simulation are provided below for Li_2MSiO_4, $LiMPO_4$, and $Li_2MP_2O_7$ (Table 2.3, 2.6, and 2.9) along with a comparison to the experimental parameters. The crystallographic and potential parameters used as inputs are also provided below.

Table 2.1 provides the short-range potential parameters used for optimizing the lattice parameters for Li_2MSiO_4 (M = Fe[33], Mn[34], and Co). Since we found no parameters in the literature used for calculating lattice parameters in Li_2CoSiO_4, we used the two-body parameters used for calculations done on $LiCoPO_4$[35] as was done in Reference 33 and 34 for Fe and Mn, respectively.

Legend of short-range potential parameters:

Y – shell charge

k – core-shell spring constant

A, C, ϱ – ion-ion potential parameters

Θ – bond angle between countercation (Si or P) and O

Cutoff values – cutoff distance used to shorten calculation (there are only negligible contributions to the potential beyond short distances)

Table 2.1. Short-Range Potential Parameters for Li_2MSiO_4 (M = Fe, Mn, Co)

(a) Two-Body					
Interaction	A (eV)	ϱ (Å)	*C* (eV*Å^6)	*Y* (e)	*k* (eV* Å^{-2})
Li^+ - O^{2-}	632.1018	0.2906	0.0	1.0	99999.0
Fe^{2+} - O^{2-}	1105.2409	0.3106	0.0	2.997	19.26
Mn^{2+} - O^{2-}	2601.394	0.278	0.0	3.42	95.0
Co^{2+} - O^{2-}	1670.2416	0.2859	0.0	3.503	110.5
Si^{4+} - O^{2-}	1283.91	0.32052	10.66	4.0	99999.0
O^{2-} - O^{2-}	22764.3	0.149	27.89	-2.96	65.0
(b) Three-Body					
bond type	K (eV*rad^{-2})	Θ_o (deg)		Cutoff P-O (Å)	Cutoff O-O (Å)
O^{2-} - Si^{4+} - O^{2-}	2.09724	109.28		1.7	3.4

Table 2.2 provides the crystallographic input parameters for optimization at constant pressure (0 Pa) of Li_2MSiO_4 (M = Fe, Mn, Co), space group $P2_1/n$.

Table 2.2. Crystallographic Parameters of Li_2MSiO_4 (M = Fe, Mn, Co)

Atom	x/a	y/b	z/c	Occupancy
Li_2FeSiO_4[33]				
Li1	0.6696	0.782	0.6661	1
Li2	0.5502	0.198	0.1014	1
Fe1	0.2898	0.7958	0.5410	1
Si1	0.0369	0.8081	0.7917	1
O1	0.8591	0.7018	0.8213	1
O2	0.4229	0.2092	0.8836	1
O3	0.6891	0.7758	0.4339	1
O4	0.9639	0.8544	0.2175	1
Li_2MnSiO_4[36]				
Li1	0.009	0.1601	0.300	1
Li2	0.2344	0.0770	0.7127	1
Mn1	0.5050	0.1659	0.3019	1
Si1	0.2538	0.4137	0.3123	1
O1	0.2589	0.4116	0.6371	1
O2	0.2516	0.5556	0.1959	1
O3	0.0392	0.3389	0.2125	1
O4	0.4647	0.3435	0.1981	1

Table 2.2 cont'd		Li_2CoSiO_4[37]		
Li1	-0.0047	0.1631	0.3072	1
Li2	0.2385	0.0760	0.7145	1
Co1	0.4968	0.1656	0.3074	1
Si1	0.2480	0.41233	0.3135	1
O1	0.2475	0.40939	0.6381	1
O2	0.2539	0.55630	0.2071	1
O3	0.0334	0.3409	0.2081	1
O4	0.4604	0.3400	0.2079	1

Table 2.3 provides the calculated and experimental lattice parameters of Li_2MSiO_4 (M = Fe, Mn, Co).

Table 2.3. Calculated and Experimental Lattice Parameters of Li_2MSiO_4 (M = Fe, Mn, and Co)

	a (Å)	*b* (Å)	*c* (Å)
Li_2FeSiO_4			
Calculated	8.076	4.9491	8.1142
Experimental[33]	8.2385	5.0034	8.2338
Δ	0.1625	0.0543	0.1196
Li_2MnSiO_4			
Calculated	6.3005	10.8349	5.0426
Experimental[36]	6.3361	10.9146	5.0730
Δ	0.0356	0.0797	0.0304
Li_2CoSiO_4			
Calculated	6.1302	10.7782	4.925
Experimental[37]	6.27433	10.6854	5.0163
Δ	0.1441	-0.09281	0.0913

Table 2.4 provides the short-range potential parameters used for optimizing the lattice parameters of $LiMPO_4$ (M = Fe, Mn, and Co)[35].

Table 2.4. Short-Range Potential Parameters for $LiMPO_4$ (M = Fe, Mn, and Co)

(a) Two-Body					
Interaction	A (eV)	ρ (Å)	C (eV*Å^6)	Y (e)	k (eV* Å^{-2})
$Li^+ - O^{2-}$	632.1018	0.2906	0.0	1.0	9999.0
$Fe^{2+} - O^{2-}$	1105.2409	0.3106	0.0	2.997	19.26
$Mn^{2+} - O^{2-}$	2601.394	0.278	0.0	3.42	95.0
$Co^{2+} - O^{2-}$	1670.2416	0.2859	0.0	3.503	110.5
$P^{5+} - O^{2-}$	897.2648	0.35898	0.0	5.0	9999.0
$O^{2-} - O^{2-}$	22764.3	0.149	44.53	-2.96	65.0
(b) Three-Body					
bond type	K (eV*rad^{-2})	Θ_o (deg)	Cutoff P-O (Å)	Cutoff O-O (Å)	
$O^{2-} - P^{5+} - O^{2-}$	1.322626	109.47	1.6	3.2	

Table 2.5 provides the crystallographic input parameters for optimization at constant pressure (0 Pa) of $LiMPO_4$ (M = Fe, Mn, Co), space group Pnma.

Table 2.5. Crystallographic Parameters of $LiMPO_4$ (M = Fe, Mn, Co)

Atom	x/a	y/b	z/c	Occupancy
		$LiFePO_4$[38]		
Li1	0	0	0	1
Fe1	0.2822	0.25	0.9738	1
P1	0.0950	0.25	0.418	1
O1	0.09713	0.25	0.7428	1
O2	0.4573	0.25	0.2067	1
O3	0.166	0.0464	0.2851	1
		$LiMnPO_4$[39]		
Li1	0	0	0	1
Mn1	0.2826	0.25	0.972	1
P1	0.096	0.25	0.413	1
O1	0.099	0.25	0.732	1
O2	0.456	0.25	0.216	1
O3	0.157	0.047	0.274	1
		$LiCoPO_4$[40]		
Li1	0.5	0.5	0.5	1
Co1	0.27859	0.25	0.9793	1
P1	0.09447	0.25	0.4184	1
O1	0.0977	0.25	0.7410	

Table 2.5 cont'd

O2	0.4550	0.25	0.2043	1
O3	0.1663	0.0446	0.2820	1

Table 2.6 provides the calculated and experimental lattice parameters for $LiMPO_4$ (M = Fe, Mn, Co).

Table 2.6. Calculated and Experimental Lattice Parameters of $LiMPO_4$ (M = Fe, Mn, Co)

	a (Å)	*b* (Å)	*c* (Å)
		$LiFePO_4$	
Calculated	10.2325	5.9500	4.6472
Experimental[38]	10.3377	6.0112	4.6950
Δ	0.1052	0.0612	0.0478
		$LiMnPO_4$	
Calculated	10.3158	6.0274	4.6837
Experimental[39]	10.431	6.0947	4.7366
Δ	0.1152	0.0673	0.0529
		$LiCoPO_4$	
Calculated	10.0812	5.8282	4.6375
Experimental[40]	10.2001	5.9199	4.6900
Δ	0.1189	0.0917	0.0525

Table 2.7 provides the short-range potential parameters used for optimizing the lattice parameters for $Li_2MP_2O_7$ (M = Fe, Mn, and Co)[41].

Table 2.7. Short-Range Potential Parameters for $Li_2MP_2O_7$ (M = Fe, Mn, and Co)

(a) Two-Body					
Interaction	A (eV)	ϱ (Å)	*C* (eV*Å^6)	*Y* (e)	*k* (eV* Å^{-2})
Li^+ - O^{2-}	632.1018	0.2906	0.0	1.0	9999.0
Fe^{2+} - O^{2-}	1105.2409	0.3106	0.0	2.997	19.26
Mn^{2+} - O^{2-}	2601.394	0.278	0.0	3.42	95.0
Co^{2+} - O^{2-}	1670.2416	0.2859	0.0	3.503	110.5
P^{5+} - O^{2-}	897.2648	0.35898	0.0	5.0	9999.0
O^{2-} - O^{2-}	22764.3	0.149	44.53	-2.96	65.0
(b) Three-Body					
bond type	K (eV*rad^{-2})	Θ_o (deg)	Cutoff P-O (Å)	Cutoff O-O (Å)	
O^{2-} - P^{5+} - O^{2-}	1.322626	109.47	1.6	3.2	

Table 2.8 provides the crystallographic input parameters for optimization at constant pressure (0 Pa) of $Li_2MP_2O_7$ (M = Fe, Mn, Co), space group $P2_1/c$.

Table 2.8. Crystallographic Parameters of $Li_2MP_2O_7$ (M = Fe, Mn, Co)

Atom	x/a	y/b	z/c	Occupancy
		$Li_2FeP_2O_7$[42]		
Fe1	0.6723	0.5715	0.6947	1
Fe2	0.8233	0.2872	0.7557	0.67
Fe3	0.0369	0.069	0.655	0.33
P1	0.5737	0.648	0.3764	1
P2	0.2456	0.5689	0.565	1
P3	0.8894	0.7976	0.6159	1
P4	0.7577	0.0434	0.5258	1
O1	0.8548	0.137	0.6183	1
O2	0.7863	0.0319	0.3739	1
O3	0.375	0.5841	0.9843	1
O4	0.1091	0.5658	0.5693	1
O5	0.6909	0.3244	0.3385	1
O6	0.7335	0.4132	0.5859	1
O7	0.0727	0.2754	0.0159	1
O8	0.4156	0.2902	0.1869	1
O9	0.8459	0.6667	0.6833	1
O10	-0.0058	0.8669	0.7157	1
O11	0.4817	0.9339	0.7775	1

Table 2.8 cont'd

O12	0.5528	0.6609	0.5243	1
O13	0.2922	0.0744	0.1168	1
O14	0.2258	0.1038	0.4004	1
Li1	0.445	0.727	0.106	1
Li2	0.972	0.625	0.429	1
Li3	0.436	0.584	0.813	1
Li4	0.0369	0.069	0.655	1
$Li_2MnP_2O_7$[43]				
Mn1	0.24502	0.71349	0.1785	1
Mn2	0.29847	0.41987	0.32451	1
P1	0.37664	0.65002	0.57237	1
P2	0.05902	0.93196	0.24432	1
P3	0.02599	0.45499	0.76037	1
P4	0.61877	0.79625	-0.10854	1
O1	0.16246	0.82821	0.3135	1
O2	0.48113	0.77732	-0.07557	1
O3	0.38378	0.86486	0.14432	1
O4	0.02156	0.84084	0.55022	1
O5	0.43627	0.4344	-0.11127	1
O6	0.18198	0.83005	-0.15145	1
O7	0.02235	0.41597	0.62905	1
O8	0.18629	0.2894	0.41843	1
O9	0.09527	0.60349	0.77455	1

Table 2.8 cont'd

O10	0.3883	0.5802	0.70422	1
O11	0.41492	0.58835	0.26962	1
O12	0.27481	0.56376	0.48188	1
O13	0.37991	1.03269	-0.21286	1
O14	0.22241	0.63316	-0.0038	1
Li1	0.6548	0.0866	0.0422	1
Li2	0.0855	0.1081	0.0288	1
Li3	0.6654	0.0748	0.5423	1
Li4	0.3898	0.2223	0.5523	1
$Li_2CoP_2O_7$[42]				
Co1	0.6737	0.5704	0.6977	1
Co2	0.823	0.285	0.756	0.71
Co3	0.051	0.096	0.665	0.29
P1	0.5776	0.6504	0.3761	1
P2	0.2433	0.5702	0.5636	1
P3	0.8877	0.7945	0.6176	1
P4	0.7582	0.0466	0.52	1
O1	0.8552	0.1373	0.6132	1
O2	0.7857	0.0327	0.375	1
O3	0.3754	0.5841	0.9808	1
O4	0.1056	0.5685	0.5706	1
O5	0.69	0.321	0.3368	1
O6	0.7353	0.4126	0.5856	1

Table 2.8 cont'd

O7	0.0777	0.2771	0.0238	1
O8	0.4148	0.2907	0.1859	1
O9	0.8451	0.6656	0.6786	1
O10	-0.0032	0.8641	0.7165	1
O11	0.4811	0.9349	0.7757	1
O12	0.5569	0.6573	0.5271	1
O13	0.2916	0.0768	0.1169	1
O14	0.2289	0.1046	0.4046	1
Li1	0.444	0.7336	0.1144	1
Li2	0.9728	0.6167	0.416	1
Li3	0.4544	0.568	0.82	1
Li4	0.051	0.096	0.665	1

Table 2.9 provides the calculated and experimental lattice parameters for $Li_2MP_2O_7$ (M = Fe, Mn, Co).

Table 2.9. Calculated and Experimental Lattice Parameters of $Li_2MP_2O_7$ (M = Fe, Mn, Co)

	a (Å)	*b* (Å)	*c* (Å)
	$Li_2FeP_2O_7$		
Calculated	10.905	9.5586	9.939
Experimental[42]	11.0192	9.7488	9.8057
Δ	0.1142	0.1902	-0.1333
	$Li_2MnP_2O_7$		
Calculated	11.233	9.7395	10.0234
Experimental[43]	11.18	9.8289	9.9158
Δ	-0.053	0.0894	-0.1076
	$Li_2CoP_2O_7$		
Calculated	10.8374	9.5808	9.6635
Experimental[42]	10.9574	9.6921	9.7611
Δ	0.12	0.1113	0.0976

Chapter 3: A Crystal-chemical Guide for Understanding Redox Energy Variations of $M^{2+/3+}$ Couples in Polyanion Cathodes for Lithium-ion Batteries[1]

3.1 INTRODUCTION

The research on polyanion cathodes for lithium-ion batteries has continued to gain momentum since Padhi et al. reported the electrochemical properties of $LiFePO_4$ in 1997.[12] The interest in polyanion cathodes comes from added safety and higher voltage values in comparison to the oxide analogues with the same $M^{2+/3+}$ redox couples. The increased safety and higher voltage values have been attributed to strong covalent bonding within the polyanion units. Over the years these inherent characteristics of polyanion cathodes have promoted the investigation of additional polyanion chemistries for use in lithium-ion batteries.

Among the other chemistries being investigated are the Li_2MSiO_4 silicates, $Li_2MP_2O_7$ pyrophosphates, and $LiMBO_3$ borates (M = Mn, Fe, Co, and Ni). Each of these chemistries possesses additional favorable characteristics as cathode materials. The borates contain the lightest of the polyanion units (BO_3) and, therefore, have a higher theoretical capacity (~ 200 mAh g^{-1}) than $LiFePO_4$ (~ 170 mAh g^{-1}). The pyrophosphates and silicates offer the appealing possibility of extracting/inserting two lithium ions per transition metal ion in the material, further increasing the theoretical capacity, respectively, to ~ 220 and 330 mAh g^{-1}. Additionally, silicon is one of the most abundant elements on earth's crust, offering reduction in cost for the silicates.

The voltage of a given cathode material is determined by the location of the $M^{n+/(n+1)+}$ redox couple relative to that of the Li/Li^+ couple. The ability of the polyanion to

[1] This chapter is based on previously published work: A. Gutierrez, N. A. Benedek, and A. Manthiram, "Crystal-Chemical Guide for Understanding Redox Energy Variations of $M^{2+/3+}$ Couples in Polyanion Cathodes for Lithium-ion Batteries," *Chemistry of Materials*, 25, 4010 - 4016 (2013). Dr. Manthiram supervised the project and Dr. Benedek provided help with the computation of the electrostatic site potential. A. G. performed all other analysis.

shift the $M^{n+/(n+1)+}$ redox couple, known as the inductive effect, was originally used to explain the increased voltages of the polyanion cathodes compared to their oxide analogs. It was postulated that a more covalent polyanion lowers the $M^{n+/(n+1)+}$ redox couple compared to that in an oxide, resulting in a higher cell voltage vs. Li/Li^+. For example, the voltage was found to increase from 3.0 to 3.6 V on going from $Fe_2(MoO_4)_3$ to $Fe_2(SO_4)_3$, which have similar crystal structures, due to a larger covalence of the SO_4 units compared to the MoO_4 units arising from a higher electronegativity of S. [9, 10]

However, the various polyanion cathodes, viz., $LiMPO_4$, Li_2MSiO_4, $Li_2MP_2O_7$, and $LiMBO_3$ all have different crystal structures and consequently different local environments. For instance, the transition metal and the counter-cations in each of these compounds have different coordination numbers. These structural differences have an effect on the redox energy. Padhi et al. provided some guidance as to how structural differences may shift the $M^{n+/(n+1)+}$ redox energies. For example, it was pointed out that edge sharing of the MO_6 octahedra within the olivine structure further increases the voltage compared to compounds that do not have edge sharing.[12, 44] Therefore, it may be useful to analyze how edge sharing affects the voltage of the new polyanion chemistries. With the increased research interest in polyanion chemistries it is important to broaden our understanding of (i) how the coordination of the transition metal ions shifts the redox energy, (ii) how to assess the covalency of the polyanion beyond the electronegativity of the countercation, and (iii) how edge sharing between polyhedra affects the discharge potential of the polyanion chemistries.

Accordingly, the goal of this work was to provide an understanding of how the structural differences among the polyanion cathodes affects the cell voltage. We also consider additional methods for determining the covalency of the polyanion units by looking at the hybridization and resonance forms occurring in the polyanions. The results

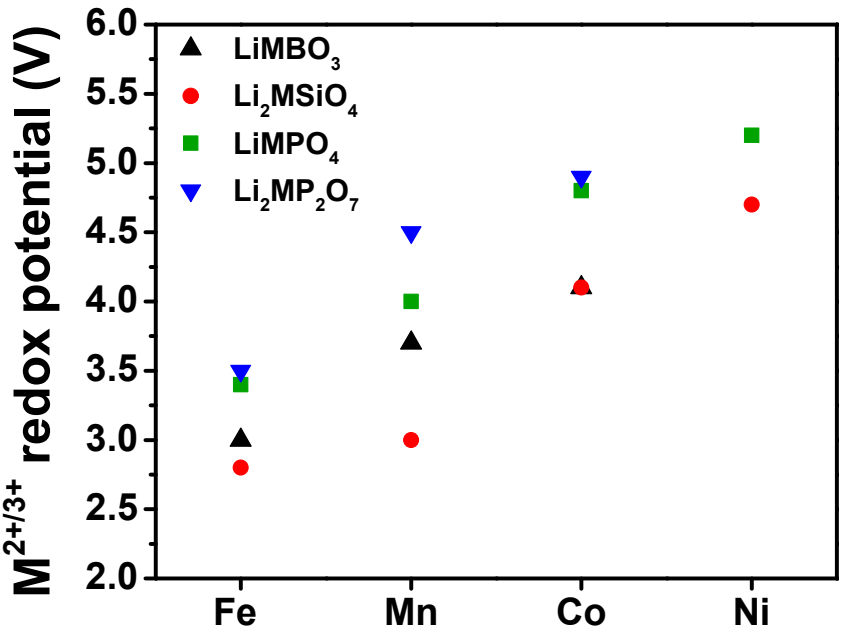

Figure 3.1. Discharge potential values for the $M^{2+/3+}$ redox couples in borate, silicate, phosphate and pyrophosphate polyanion cathode materials. Both experimental and predicted values were used. See the text for explanation as to how the values were chosen.

presented herein could become useful for the design of high-performance cathode materials for lithium-ion batteries.

3.2 Results and Discussion

3.2.1 Structure and voltage

To begin, we provide a brief review of the structure of each of the polyanion cathodes and the voltages we have chosen for our work. In general, we have used the experimental value of the voltage when one has been reported in the literature. In cases

where the predicted voltage is used instead, we provide an explanation as to why this was done.

Although other structures ($P2_1/n$, Pbca,[45] and Cmcm[46]) have been reported for the phosphates, their limited electrochemical activity has kept the olivine structure at the forefront of research interest. The olivine phosphates $LiMPO_4$ with M = Mn, Fe, and Co have all been synthesized and electrochemically tested. The discharge curves for the phosphates exhibit a plateau indicating the occurrence of a two-phase reaction during charge/discharge. The discharge potential values are 3.4 V (Fe),[47] 4.1 V (Mn),[48] and 4.8 V (Co).[49] The Ni-phosphate has also been synthesized but the voltage for $Ni^{2+/3+}$ in olivine has not been observed.[50] Therefore, we use the predicted voltage based on computation for Ni (5.2 V)[51] in our discussion.

The $LiMBO_3$ borates with M = Mn, Fe, and Co have been reported with a C2/c monoclinic structure. The sloping discharge curve for the borate compounds indicates a single-phase reaction. The reported discharge potential values for the Fe and Mn compounds are, respectively, 3.0[52] and 3.7 V.[53] In the case of single-phase reactions, the amount of lithium extracted will affect the reported discharge potential value because of the sloping nature of the discharge curve. Therefore, we note that 80% of the theoretical capacity (~ 220 mAh g^{-1}) was realized with the Fe-compound while only 45% was obtained with the Mn-compound. We note that if a comparable percentage of lithium were extracted from the two compounds, the average discharge potential for the Mn-compound would be lower than the currently reported value. The experimental discharge potential for the Co-compound was reported on a material that delivered only ~ 2 % of the theoretical capacity.[54] Because of the possible error in estimating the discharge potential in a material where such a low capacity was achieved, we chose to use the

predicted value of 4.1 V.[55] No data are available on the experimental or predicted values for the $Ni^{2+/3+}$ redox couple in the borates.

The $Li_2MP_2O_7$ pyrophosphates with M = Mn, Fe, and Co all have a $P2_1/c$ monoclinic structure. The charge/discharge in $Li_2MP_2O_7$ occurs via a two-phase reaction as indicated by the flat discharge curves in the literature. The values for the discharge potential are 3.5 V (Fe),[56] 4.5 V (Mn),[57] and 4.9 V (Co).[42] To our knowledge the Ni-pyrophosphate has not been synthesized nor has a predicted value been put forth in the literature for the $Ni^{2+/3+}$ redox couple.

The Li_2MSiO_4 silicates belong to a family of materials in which the transition-metal (TM) ions have tetrahedral coordination. They are rich in polymorphism and can be divided into two families (β and γ, related to the Li_3PO_4 polymorphs). The two families differ in the ordering/distribution of cations within the available tetrahedral sites. In the β family, the cations are distributed such that the tetrahedra all point in the same direction and share only corners. In the γ family, the tetrahedra point in opposite directions and share both corners and edges. The literature denotes that structural changes occur during the first few cycles and continues until the most thermodynamically stable phase is formed. Along with the structural changes, a change in the charge/discharge potential value is also reported during the first few cycles. Because of similar formation energies between the polymorphs, several phases may be present and contribute to the difficulty in interpreting the charge/discharge potentials for some of the silicate compounds reported in the literature.

Sirisopanaporn et al.[58] synthesized three "very well-defined crystallographically pure" polymorphs of Li_2FeSiO_4 and studied how the local environment of Fe^{2+} may affect the voltage values. The results revealed that of the three polymorphs studied, two of them exhibited a value of 2.8 V for the first discharge potential with no subsequent changes

upon further cycling. The third polymorph used in that study gave two reduction peaks during the first discharge process, one at 3.0 V and another at 2.8 V. By the fifth cycle, the reduction peak at 3.0 V disappeared and only the peak at 2.8 V remained. Because the discharge potential at 3.0 V was associated with unstable phases and structural rearrangement, we use the reported value of 2.8 V for the Fe-compound.

To our knowledge, similar studies do not exist for the Mn and Co compounds, although similar changes in the potential have been reported to occur during the first few cycles, which is indicative of structural rearrangements.[36, 59, 60] Adding complexity to the interpretation of the voltage trends is that the delithiation of Li_2FeSiO_4 has been reported as a two-phase reaction,[61] while the discharge curve for the Mn-compound shows indications of a single-phase reaction. For the Mn-compound, we use a discharge potential of 3.0 V where ~ 70 % of the theoretical capacity (~ 330 mAh g^{-1}) was achieved.[62] Although not all of the theoretical capacity was achieved and the discharge curve is sloping, the value of 3.0 V is a good estimate for our work here since we are comparing the $M^{2+/3+}$ redox couples and extraction of the second lithium would involve the $Mn^{3+/4+}$ redox couple. For the Co-compound, it appears that a plateau is formed at ~ 4.1 V, which indicates that delithiation may be occurring as a two-phase reaction similar to that in the Fe-compound.[60, 63] The Ni-compound has not been synthesized. Therefore, we use the predicted value of 4.7 V given in the literature.[64] As can be seen from Figure 3.1, for a given TM ion, the discharge potential values of the polyanion cathodes exhibit a general trend of $P_2O_7 > PO_4 > BO_3 > SiO_4$.

3.2.2 Transition-metal coordination

As stated previously, the cell voltage (V_{oc}) is a measure of the position of the $M^{2+/3+}$ redox couple relative to that of Li/Li^+. The position of the $M^{2+/3+}$ redox couple can

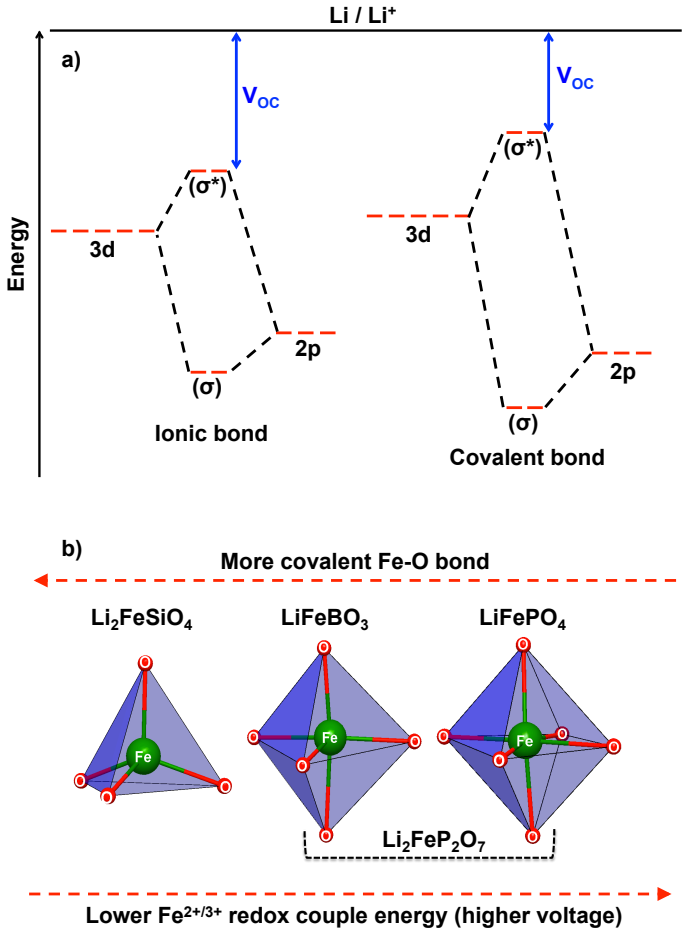

Figure 3.2. a) A more covalent bond increases the repulsion between the bonding and antibonding orbitals. The increase in repulsion raises the antibonding orbitals closer to the Fermi level in lithium and lowers the voltage vs. Li/Li^+. b) The polyhedra in the borate, silicate, phosphate, and pyrophosphate compounds. As the coordination number decreases, the M-O bond becomes more covalent.

be lowered/raised by changing the covalent character of the M-O bond. A more covalent M-O bond will introduce quantum mechanical repulsion between the bonding and antibonding orbitals, raising the antibonding orbitals closer to the Fermi level in lithium

and thereby decreasing the voltage (Figure 3.2a). When the M-O bond is more ionic, the antibonding orbitals will be raised to a lesser extent, resulting in a higher voltage vs. Li/Li^+. There are several ways that the covalent character of the M-O bond can be altered, one of which is the coordination geometry of M.

The TM ion is either in four, five, or six-fold coordination in the polyanion cathodes analyzed in this work. For example, the coordination of the TM ions in the silicates, borates, and phosphates is, respectively, tetrahedral,[65] trigonal bipyramidal,[52-54] and octahedral. Furthermore, the TM ions in the pyrophosphate structure are in both octahedral and trigonal bipyramidal coordination. A schematic of how the M-O covalency changes based on the TM ion coordination and the associated lowering/raising of the redox couple is shown in Figure 3.2b. As the coordination number decreases (following the top arrow), less steric hindrance renders a more stable (covalent) M-O bond. As a result, a system that contains TM ions with a higher coordination number will deliver a higher voltage (following the bottom arrow in Figure 3.2b). Based on the coordination of the TM ions, the voltage delivered by the polyanion cathodes can be anticipated as: $P_2O_7 \approx PO_4 > BO_3 > SiO_4$. As can be seen from Figure 3.1, a correct prediction of the relative voltages (except for the Co silicate and borate compounds) can be made based solely on the coordination of the TM ions.

Although the coordination can be used to gauge the voltage trends of the compounds, it provides no explanation as to why the pyrophosphate system exhibits a slightly higher discharge potential than the phosphate system. The reason may be associated with differences in the polyanion structure and will be discussed further below.

3.2.3 Polyhedra connectivity

Another way to shift the location of the redox energy in each of the polyanion cathodes is by the strength of the Madelung electric field felt by the TM ions. Because the Madelung electric field (or potential) destabilizes (raises) the $M^{2+/3+}$ redox energy, a stronger electric field results in a lower discharge potential vs. Li/Li^+. There are two cooperative points that are important to remember when considering the strength of the electric field felt by a cation. First, the *magnitude* of the electric field is inversely proportional to the nearest-neighbor (NN) distances. Second, the "contribution" of cation-cation electrostatic repulsion is to *reduce* the magnitude of the electric field. Therefore, increased repulsion through shorter cation-cation distances results in a reduced electric field and higher voltage vs. Li/Li^+.

The distance between two cations is decreased in a structure where the polyhedra of the two cations share edges or faces instead of only sharing corners. Hence, it follows that the $M^{2+/3+}$ redox couple will shift to a lower energy (higher voltage vs. Li/Li^+) when the cation polyhedron share edges or faces compared to when they shares only corners. Padhi et al.[12] used this reasoning to explain why the $Fe^{2+/3+}$ redox energy in olivine lies lower than that in the NASICON framework. They concluded that the voltage was higher for the olivine than for the NASICON structure because the FeO_6 octahedra in the olivine structure share an edge with the PO_4 tetrahedra whereas the FeO_6 octahedra in NASICON do not share edges with the polyanions.

Of the polyanion materials considered in this work, only the phosphates have TM ion polyhedra that share edges with the polyanion as described above. The BO_3, SiO_4, and P_2O_7 polyanion only share corners with the TM ion polyhedra in their respective structures. This means that the $M^{2+/3+}$ redox energy in these materials is unaffected by edge sharing with the polyanion, although all of the structures do share edges with other

cation polyhedra. Therefore, we must take a closer look at how edge sharing with other cation polyhedra may affect the $M^{2+/3+}$ redox energy.

We start by looking at edge sharing with LiO_x polyhedra. The TM ion polyhedra in phosphates, pyrophosphates, and silicates share at least one edge with lithium polyhedra. In the phosphate structure, the FeO_6 polyhedra share two edges with the LiO_6 octahedra.[66] The TM ion polyhedra in the pyrophosphate structure share one edge with LiO_5 polyhedra but share an additional edge with at least one more TM polyhedra.[67] Because the TM ion polyhedra in the phosphate and pyrophosphate structures share edges with multiple cation polyhedra, an interpretation of the effect of edge sharing with lithium polyhedra may be a bit convoluted. Fortunately, the TM ion polyhedra in the silicates only share edges with lithium polyhedra. In fact, the silicates may provide the ideal scenario because there are silicate polymorphs that contain edge sharing (ES) while others have no edge sharing (NES) and they deliver different voltages vs. Li/Li^+.

Two of the three silicate polymorphs investigated by Sirisopanaporn[58] contain FeO_4 polyhedra sharing edges with LiO_4. The ES polymorphs deliver a *lower* voltage than the NES polymorph. This result is opposite to when edge sharing occurs in $LiFePO_4$. Nevertheless, Sirisopanaporn[58] provided evidence that a shorter, more covalent Fe-O bond length results when FeO_4 polyhedra accommodate the shorter LiO_4 edge length. This seems to explain the difference, except that P-O bond lengths are even shorter (~ 1.5 Å)[68] than the Li-O bond lengths (~ 2.0 Å) reported by Sirisopanaporn[58] and yet the $M^{2+/3+}$ redox energy is lowered in $LiFePO_4$ where FeO_6 octahedra share an edge with PO_4 despite the shorter P-O bond length. In order to understand completely how edge sharing with LiO_4 and PO_4 differs, the strength of the repulsive forces between two cations must be considered. In general, as the charge of either cation increases (1+ to 2+ to 3+ etc.) the repulsive force between them will also increase. The TM ion charge in both of these

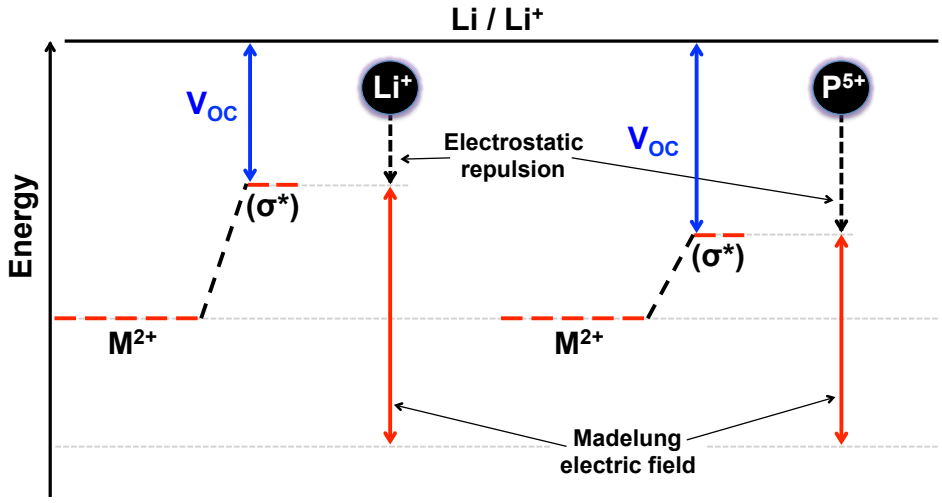

Figure 3.3. The antibonding orbitals of the M^{2+} cation are raised closer to the Fermi level in lithium when the magnitude of the Madelung electric field is larger. The repulsion exerted by P^{5+} on the transition-metal ion is large enough to reduce the magnitude of the electric field and lower the antibonding orbitals, resulting in a larger voltage vs. Li/Li+.

studies is +2, so we can gauge the strength of the repulsion based on the charge of the countercation (*i.e.*, Li and P). As shown in Figure 3.3, the repulsion felt by the TM ion sharing an edge with LiO_4 does not reduce the Madelung electric field (red arrows) greatly. In contrast, despite the P-O bond length being shorter than the Li-O bond length, the greater repulsion felt by the TM ion sharing an edge with PO_4 further reduces the Madelung electric field and lowers the $M^{2+/3+}$ redox energy.

Some of the polyanion chemistries considered in this work also contain TM ion polyhedra that share edges with other TM ion polyhedra. Within the borate structure, each MO_5 polyhedron shares two edges with other MO_5 polyhedra.[69] The TM ion polyhedra in the pyrophosphate exhibit edge sharing that is dependent on the TM ion within the structure. For example, in the Co and Fe compounds the TM polyhedra share

two edges with other TM polyhedra,[42] whereas in the Mn compound the TM polyhedra share only one edge.[43] Still, no ideal scenario exists (similar to the one with the silicate polymorphs) to provide an idea of how the TM-TM repulsion might affect the $M^{2+/3+}$ redox energy. However, from our evaluation of edge sharing occurring in the structure we conclude that not all edge sharing lowers the $M^{2+/3+}$ redox energy. Consideration must be given to the strength of the cation-cation repulsion and its ability to lower the Madelung electric field.

3.2.3 Inductive effect

The strength of the M-O covalency can also be tailored through the inductive effect. The strength of the inductive effect is most commonly fine tuned by using more electronegative counter-cations X in the M-O-X (X = B, Si, P) linkage. The electronegativity values for Si, B, and P are, respectively, 1.8, 2.0, and 2.2. A prediction of the relative voltage values based on the electronegativity of the counter-cation would render the same trend as the one predicted by the coordination of the transition metal, namely: $P_2O_7 \approx PO_4 > BO_3 > SiO_4$.

Another way to measure the covalency of the polyanion unit is by considering the electron delocalization or resonance occurring within the polyanion. Phosphorous is able to expand its octet and accommodate 10 bonding electrons in the PO_4 polyanion.[70] The expanded octet accommodates double bonds between P and O. This produces four resonance forms for phosphate. In general, the stability of a structure increases with the number of resonance forms it has. Therefore, P_2O_7 is a more covalent polyanion in comparison to PO_4 because it has more resonance forms. This explains the slightly higher voltage exhibited by the pyrophosphate compounds despite having the same

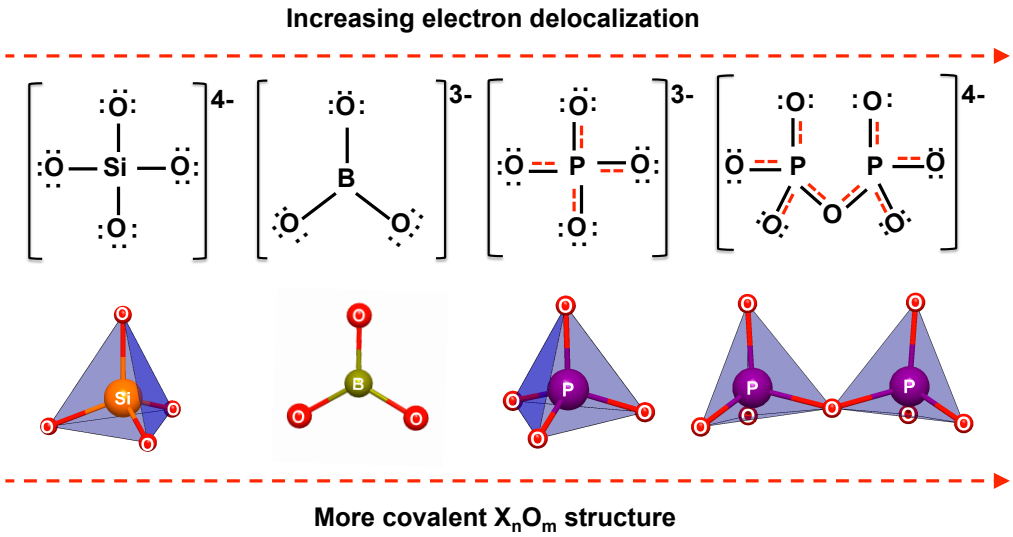

Figure 3.4. The Lewis dot representation and polyhedra for each of the polyanion. P_2O_7 is a more covalent polyanion than PO_4 due to more electron delocalization occurring as indicated by the increased number of resonance hybrids shown.

countercation (P). The resonance hybrids for the phosphate and pyrophosphate polyanion are shown in Figure 3.4.

Silicon has the ability to expand its octet when pentacoordinated.[71, 72] Nevertheless, it does not need to expand its octet to accommodate its valence electrons in SiO_4 unlike phosphorous in PO_4, which has five valence electrons. Boron in the BO_3 polyanion has an incomplete octet with only six electrons in the valence shell after bonding. Consequently, the borate and silicate polyanions do not generate any resonance forms. Electron delocalization in these structures can be discussed in terms of either the electronegativity or hybridization of the counter-cation. Both of these factors render the same prediction for the covalency of these two polyanions (BO_3 > SiO_4), so an analysis based on hybridization is unnecessary. Still, an evaluation of the hybridization may be

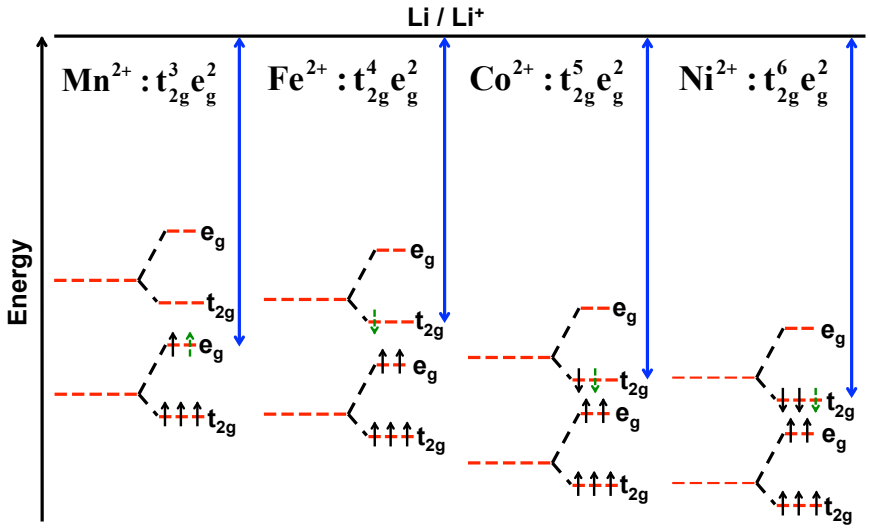

Figure 3.5. Crystal field splitting of the M^{2+} cations in octahedral coordination. The Fe compound delivers a lower voltage vs. Li/Li^+ compared to the Mn compound because of a shift in the $Fe^{2+/3+}$ redox energy due to the pairing energy of the sixth electron in the t_{2g} orbital.

useful in understanding the design of future materials. The boron counter-cation is sp^2 hybridized because of its trigonal planar coordination, whereas silicon is sp^3 hybridized due to its tetrahedral coordination. It is known that an s-orbital holds electrons more tightly to the nucleus than p-orbitals. Consequently, an sp^2 hybrid, which has 33% s character, is more electronegative than an sp^3 hybrid with only 25% s character.[73, 74] The strength of the inductive effect for the silicate and borate can be predicted correctly based simply on the electronegativity. Nevertheless, it is only by considering the resonance forms within the phosphorous containing polyanions that we gain an understanding as to why the pyrophosphates exhibit a higher discharge potential than the phosphates. Figure 3.4 summarizes the covalency of the polyanions as $P_2O_7 > PO_4 > BO_3 > SiO_4$.

3.2.3 d – orbital splitting

The trend seen in Figure 3.1, where the discharge potential of Fe < Mn < Co < Ni in each of the polyanion systems, has been discussed previously and will only be mentioned briefly here.[64, 75] The crystal field splitting that occurs for each of the M^{2+} cations in octahedral coordination is shown in Figure 3.5. The dashed arrow (green online) is the

electron involved in the redox reaction during charge/discharge. It is well-known that Fe-compounds deliver a lower voltage than Mn-compounds even though Fe sits to the right of Mn in the periodic table. This is attributed to the pairing energy needed to place the sixth electron in the t_{2g} orbital in Fe^{2+}: $3d^6$. Since Fe^{2+}: $3d^6$ always pays a pairing energy cost and Mn^{2+}: $3d^5$ does not, the voltage delivered by the Fe-compounds is expected to be lower than the Mn-compounds in each of the polyanion structures. The Co and Ni compounds also pay a pairing energy, but the cost is not sufficient to raise the Co and Ni redox couples above the $Mn^{2+/3+}$ redox energy. With the pairing energy in play, the redox energies lower in the order $Fe^{2+/3+} > Co^{2+/3+} > Ni^{2+/3+}$, as one would expect based on their position in the periodic table.

The coordination of the transition metal in each of the structures will result in unique splitting of the 3d orbitals as shown in Figure 3.6a (drawn to scale) for the Mn^{2+}: $3d^5$ compounds.[76] A prediction of the voltage delivered (shown by the blue arrows) based only on crystal field splitting would render: $BO_3 < PO_4 < SiO_4$, which does not match the trend for the experimental results shown in Figure 3.1. This suggests that crystal-field splitting considerations alone may not be adequate to understand the differences in the discharge potentials. We provide a schematic of how the antibonding orbitals of Mn^{2+}: $3d^5$ would shift in Figure 3.6b when considering the M-O covalency based on the structure and inductive effect. The dashed lines (red online) without electrons in Figure

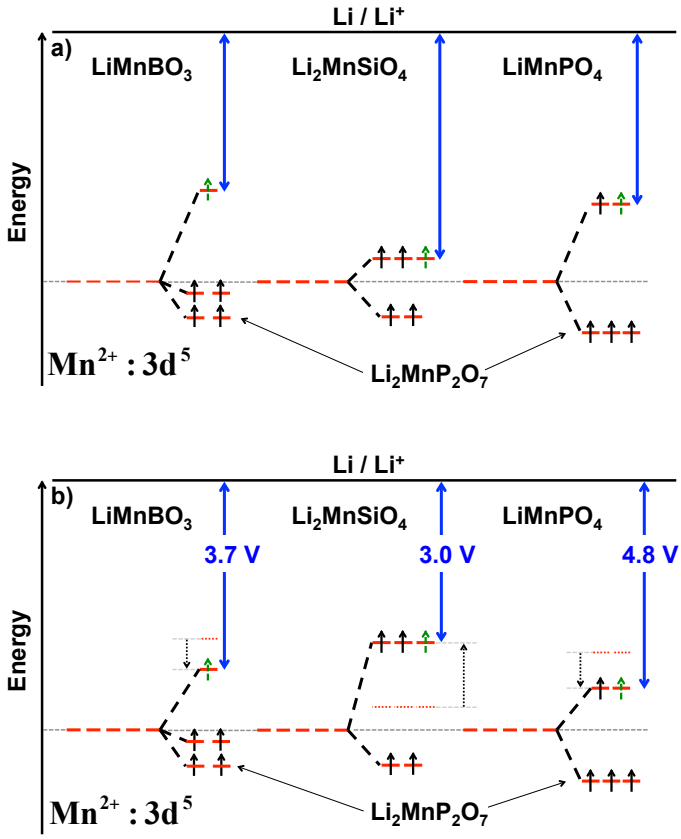

Figure 3.6. a) Crystal field splitting (drawn to scale with values from Reference 39) of the 3d orbitals in different coordination. A prediction of the voltage delivered (magnitude represented by the blue arrows) based solely on crystal field splitting would render: BO_3 < PO_4 < SiO_4, which does not match the trend for the results shown in Figure 3.1. b) Schematic of how the $Mn^{2+/3+}$ redox energy shifts in each material when consideration is given to the structure and inductive effect. The shifts are not drawn to scale.

3.6b represent the location of the orbital before any consideration is given to the structure and inductive effect. The TM coordination and inductive effect both predicted the silicates to have the most covalent M-O bond. In addition, edge sharing in the silicates

was also shown to increase the covalency of the M-O bond. Therefore, each of these factors contributes in shifting (dashed arrow pointing up) the $Mn^{2+/3+}$ redox energy up in Li_2MnSiO_4 as shown in Figure 3.6b. On the other hand, each factor (TM coordination, inductive effect, and edge sharing) predicted the phosphates to have the least covalent M-O bond, which lowers (dashed arrow pointing down in Figure 3.6b) the $Mn^{2+/3+}$ redox energy. The M-O bond in the borates was always more covalent than that in the phosphates according to our assessment. Therefore, a shift to lower energy (shorter dashed arrow) in the borates would not be as large as that in the phosphates, as shown in Figure 3.6b.

The only difference from the Mn^{2+} compounds is that Fe^{2+}, Co^{2+}, and Ni^{2+} compounds all pay an energy cost ("Pairing energy" in Figure 3.7) for pairing electrons, as mentioned above. The energy cost is only dependent upon the spin multiplicity and total orbital angular momentum of the ion, which is the same regardless of the coordination of the TM ion.[77] As a result, an equivalent upward shift will occur for all compounds upon pairing electrons, as shown for Fe^{2+}: $3d^6$ in Figure 3.7. Similar shifts to the redox energy that occurred for the Mn^{2+} compounds based on the structure and polyanion covalency will occur in the Fe, Co, and Ni compounds (as shown for Fe in Figure 3.7).

Table 3.1 shows the electrostatic site potential (ESP) for the TM ions in the silicates, phosphates, and pyrophosphates (see Chapter 2 for details). The ESP value measures the potential felt by the TM ion due to its interaction with the point charges that make up the lattice. The ESP value for a given TM ion decreases in the order $SiO_4 > PO_4 > P_2O_7$, the same order seen for the $M^{2+/3+}$ redox energy discussed qualitatively in this work. This provides support for how each structural feature examined in this work contributes to the shifting of the redox couples in polyanion cathodes.

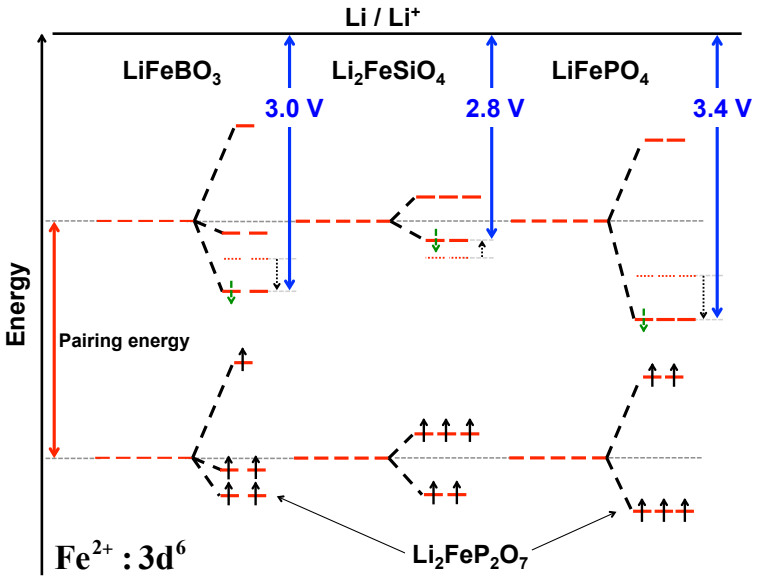

Figure 3.7. Schematic of how the $Fe^{2+/3+}$ redox energy will shift (dashed arrows) when consideration is given to the structure and inductive effect. The energy cost for pairing electrons is assumed to be the same in each of the compounds.

Table 3.1 The electrostatic site potentials (V_{Fe}, V_{Mn}, V_{Co}) for the iron, manganese, and cobalt sites in polyanion cathodes

Polyanion	V_{Fe} (V)	V_{Mn} (V)	V_{Co} (V)
Li_2MSiO_4	-16.29	-22.13	-22.71
$LiMPO_4$	-24.25	-23.16	-24.69
$Li_2MP_2O_7$	-25.83	-33.51	-25.76

3.4 CONCLUSIONS

A guide to how the $M^{2+/3+}$ redox energies in polyanion cathodes are affected by the structure and inductive effect was provided. Although we acknowledge there are other techniques available, which are more rigorous, the methods presented in this work are useful for their simplicity and accuracy. We show that the magnitude of the voltages delivered by the polyanion cathodes can be predicted based simply on the coordination of the TM ion. Additionally, edge sharing with the TM polyhedra has been viewed as producing a higher voltage vs. Li/Li^+, but our analysis provides some guidance as to when edge sharing produces the opposite effect. For example, edge sharing with LiO_4 polyhedra in the silicates raises the $M^{2+/3+}$ redox energy, while edge sharing with PO_4 polyhedra in the phosphates lowers the $M^{2+/3+}$ redox energy. Furthermore, we analyzed the covalency of the polyanion structure by considering the resonance occurring in the polyanion. Only by considering the resonance forms in the P_2O_7 and PO_4 polyanions can the differences in voltage delivered by the phosphates and pyrophosphates be explained. Lastly, the voltage delivered by polyanion cathodes cannot be understood based solely on crystal field splitting of the 3d orbitals. Only by considering shifts to the $M^{2+/3+}$ redox energy initiated by structural differences and by the covalency of the polyanion can we fully understand the voltage trends in polyanion cathode materials.

Chapter 4: High-capacity, Aliovalently-doped Olivine $LiMn_{1-3x/2}V_x\square_{x/2}PO_4$ Cathodes without Carbon Coating

4.1 INTRODUCTION

Lithium-ion batteries deliver energy densities that exceed that of other rechargeable battery systems by a factor of at least 2.5.[8] Nevertheless, there is immense interest to lower the cost, improve the safety and cycle life, and increase the energy and power. Polyanion cathodes are attractive in this regard as the strong covalent bonding within the polyanion unit enhances the thermal stability/safety and leads to higher operating voltages compared to their oxide counterparts with a given $M^{2+/3+}$ redox couple.

Following the initial work on $Fe_2(XO_4)_3$ (X = S, Mo, and W) by Manthiram and Goodenough in the 1980's,[9, 10] olivine $LiMPO_4$ (M = Mn, Fe, Co, and Ni) were discovered as potential cathodes in the 1990's by Goodenough's group.[12] Since then a majority of the work, particularly on $LiFePO_4$, has focused on overcoming its poor electronic and lithium-ion conductivities by decreasing the particle size and coating with carbon.[78, 79] Subsequently, aliovalent doping of $LiFePO_4$ was reported to increase the electronic conductivity by 10^8 times,[80] although it was later reported that a percolating nano-network of metal-rich phosphides was responsible for the enhanced conductivity.[81] While computational studies have suggested that aliovalent doping is not energetically favorable,[68, 82] there has been an increasing amount of literature demonstrating that doping can occur on the Li or Fe sites.[83-92] Our group showed recently by employing a low-temperature (< 300 °C) microwave-assisted solvothermal (MW-ST) synthesis approach that a significant amount (20 atom %) of V^{3+} can be substituted for Fe^{2+} in $LiFePO_4$.[85] However, an extrusion of vanadium from the lattice occurs when the samples are heated beyond a threshold temperature (525 °C), demonstrating the temperature-dependence of aliovalent V^{3+} doping for Fe^{2+}. The aliovalent doping of $LiFePO_4$ has also been reported

in the literature to improve the electrical conductivity and electrochemical performance.[83, 88, 93]

One of the drawbacks with $LiFePO_4$ is the low operating voltage of ~ 3.5 V. In this regard, $LiMnPO_4$ has become appealing as it offers higher operating voltage of 4.1 V, which is in the ideal regime to maintain good electrolyte stability. However, the performance of $LiMnPO_4$ is inferior to that of $LiFePO_4$ due to additional complications such as Jahn-Teller distortion associated with Mn^{3+} ions and lower electronic conductivity than that of $LiFePO_4$.[94, 95] By exploiting similar strategies applied to $LiFePO_4$ (nanoparticles and carbon coating),[96] some improvement has been made on the performance of $LiMnPO_4$, but it is still far below that of $LiFePO_4$. Recent literature reveals that isovalent substitution of Fe^{2+} for Mn^{2+} in $LiMnPO_4$ improves the performance, but with a voltage step. The use of other 2+ cations (Mg^{2+}, Ni^{2+}, Cu^{2+}, Zn^{2+}) has also been shown to improve the performance.[94, 97-99] Aliovalent substitution of Mn^{2+} in $LiMnPO_4$ has also been attempted, but in general, the incorporation of the aliovalent dopant concentration has been extremely small (~ 0.02 atom %).

We present here a successful substitution of Mn^{2+} by a significant amount of aliovalent V^{3+} in $LiMn_{1-3x/2}V_x\square_{x/2}PO_4$ ($0 \leq x \leq 0.20$) by the low-temperature (< 300 °C) MW-ST process. We demonstrate that the low-temperature synthesis method is crucial in obtaining a higher level of doping. We also show that the aliovalent doping, even without any carbon coating, enhances the reaction kinetics and increases the discharge capacity. Moreover, through X-ray absorption spectroscopy (XAS) data, we attribute the improved electrochemical performance to an increased Mn-O hybridization in the vanadium-doped samples.

4.2 EXPERIMENTAL

4.2.1 Microwave-assisted solvothermal synthesis

The $LiMn_{1-3x/2}V_x\square_{x/2}PO_4$ ($0 \leq x \leq 0.20$) samples were prepared via a microwave-assisted solvothermal process as described in Chapter 2. The $LiMn_{0.70}V_{0.20}PO_4$ sample was coated with PEDOT : PSS (poly(3,4-ethylenedioxythiophene) poly-(styrenesulfonate), Clevios P VP AI 4083 with a resistivity of 500–5000 Ω·cm) by mixing 10 mL of water, 0.1 mg of the active material, and enough PEDOT:PSS solution to incorporate 5 wt. % in the final product.[100]

Phase stability with increasing temperature. In order to determine the stability of the vanadium-doped samples at high temperatures, the $LiMn_{0.70}V_{0.20}\square_{0.10}PO_4$ sample was heated in flowing 5% H_2 – 95% Ar at various temperatures (525 – 725 °C) for 6 h, as was carried out before with the analogous $LiFe_{1-3x/2}V_x\square_{x/2}PO_4$ samples.[85]

Materials characterization. The chemical compositional analysis was carried out with inductively coupled plasma (ICP) as described in Chapter 2. X-ray powder diffraction (XRD) data were collected with a Rigaku Ultima IV instrument with Cu Kα radiation and analyzed by Rietveld refinement with Fullprof/WinPLOTR. Scanning electron microscopy (SEM) images and elemental dot maps were carried out with a Hitachi S5500 SEM/STEM microscope with energy dispersive spectroscopic (EDS) capability. Fourier transform infrared (FTIR) spectra were collected with a PerkinElmer BX FTIR with pellets prepared by grinding and pressing samples with dried KBr powder.

V-edge/Mn-edge X-ray absorption near edge spectroscopy (XANES) data were collected in transmission mode at Beamline X18A at the National Synchrotron Light Source of Brookhaven National Laboratory as described in Chapter 2. The soft XAS was performed at Beamline 8.0.1 of the Advanced Light Source (ALS) in Lawrence Berkeley National Laboratory (LBNL) as described in Chapter 2.[32]

Electrochemical Characterization. Electrochemical properties were evaluated with 2032-type coin cells and were assembled as detailed in Chapter 2. The coin cells were tested with an Arbin cycler at C/20 rate. A Radiometer Analytical Votalab PGZ402 potentiostat was used to collect cyclic voltammetry (CV) data with a two-electrode coin cell assembly at a rate of 0.1 mV/s. Electrochemical impedance spectra (EIS) were recorded with a Solartron 1260A impedance analyzer in the frequency of 100 kHz to 0.1 Hz with an ac voltage amplitude of 5 mV.

Table 4.1. Lattice parameters of undoped and V-doped $LiMnPO_4$ obtained by Rietveld refinement of X-ray diffraction data

Sample	a (Å)	b (Å)	c (Å)	V (Å^3)	χ^2
$LiMnPO_4$	10.45480	6.09010	4.74345	302.019	1.66
$LiMn_{0.925}V_{0.05}PO_4$	10.42722	6.08349	4.74407	300.936	1.81
$LiMn_{0.85}V_{0.10}PO_4$	10.42103	6.07047	4.74577	300.220	1.91
$LiMn_{0.775}V_{0.15}PO_4$	10.40757	6.06775	4.74678	299.762	1.74
$LiMn_{0.70}V_{0.20}PO_4$	10.40559	6.06580	4.74708	299.628	1.71

4.3 Results and Discussion

Phase-pure $LiMn_{1-3x/2}V_x\square_{x/2}PO_4$ samples were obtained with the low-temperature MW-ST process with x = 0.00, 0.05, 0.10, 0.15, and 0.20. All diffraction peaks could be indexed to the olivine structure (space group: *Pnma)*. The lattice parameters, obtained by Rietveld refinement, are shown in Table 4.1. As expected, the a and b lattice parameters, along with the volume, continuously decrease with increasing substitution of smaller V^{3+} ions for larger Mn^{2+} ions. The c lattice parameter increases slightly as the vanadium content increases.

Table 4.2. ICP data for undoped and V-doped $LiMnPO_4$ prepared according to $LiMn_{1-3x/2}V_x\square_{x/2}PO_4$

Sample	Li/P[a]	Mn/P[a]	V/P[a]
$LiMnPO_4$	1.00	0.97	0.00
$LiMn_{0.925}V_{0.05}PO_4$	1.03	0.91	0.06
$LiMn_{0.85}V_{0.10}PO_4$	0.98	0.82	0.11
$LiMn_{0.775}V_{0.15}PO_4$	1.02	0.74	0.15
$LiMn_{0.70}V_{0.20}PO_4$	1.00	0.67	0.17

[a]Errors in ICP ratios are estimated to be around 2 – 3 %.

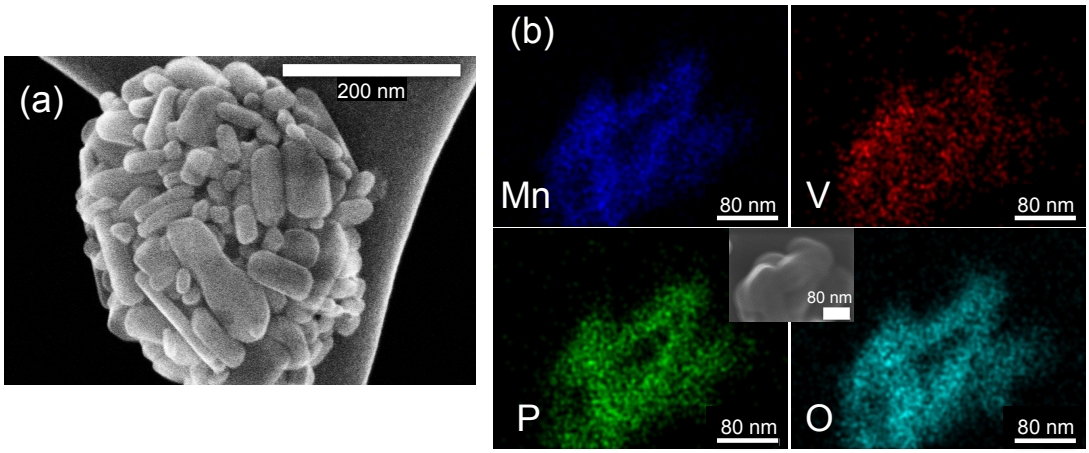

Figure 4.1. (a) SEM image of $LiMn_{0.70}V_{0.20}PO_4$ and (b) STEM image and corresponding elemental dot map of as-prepared $LiMn_{0.70}V_{0.20}PO_4$ demonstrating an even distribution of Mn, V, P, and O in sample particles.

The ICP results shown in Table 4.2 match well with the intended elemental ratios for each of the samples according to the formula $LiMn_{1-3x/2}V_x\square_{x/2}PO_4$, as previously determined for the vanadium-doped $LiFePO_4$.[85, 88] SEM images (Figure 4.1a) show the morphology to be nanorods 20 – 200 nm in length. In order to determine the elemental distribution, elemental dot mapping was carried out on each of the samples. We mapped a range of particle sizes in each of the samples and found no evidence of any elemental poor or rich regions; each sample showed a homogenous distribution of the elements as shown for the x = 0.2 sample (Figure 4.1b), providing further evidence of substitution of vanadium into the lattice. FTIR spectra of the undoped and vanadium-doped $LiMnPO_4$, $LiVOPO_4$, and $Li_3V_2(PO_4)_3$ are compared in Figure 4.2. The intramolecular vibrations of

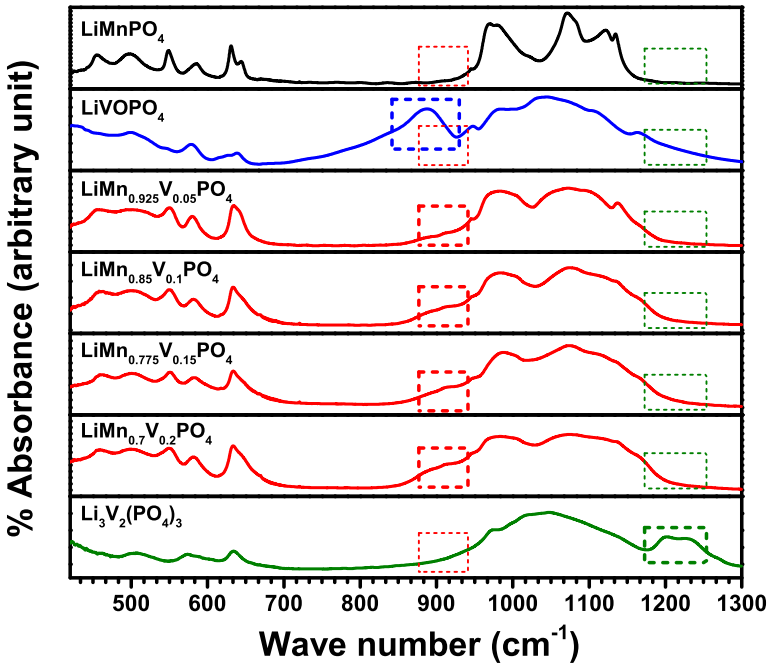

Figure 4.2. FTIR absorbance spectra of pristine and vanadium-doped $LiMnPO_4$ with $Li_3V_2(PO4)_3$ and $LiVOPO_4$ shown as reference spectra. The dashed boxes indicate features relevant for comparison of the spectra.

the PO_4^{3-} anion dominate the spectra of $LiMPO_4$ materials. The low energy bands at 493 and 502 cm^{-1} are due to the symmetric bending modes (ν_2) and/or lattice vibrations. Antisymmetric bending (ν_4) of the PO_4^{3-} anion is assigned to the peaks between 550 and 630 cm^{-1}. The peaks between 1070 and 1130 cm^{-1} are assigned to antisymmetric stretching (ν_3) of the PO_4^{3-} anion while the peak at 973 cm^{-1} is assigned to the symmetric stretching mode (ν_1).

There are minor differences between the spectra of undoped and vanadium-doped $LiMnPO_4$. The symmetric stretching band at 973 cm^{-1} remains in the same location but is broader in the doped samples. Some resolution is also lost in the doublet peak at 630 cm^{-1}, the two ν_3 bands (1150 and 970 cm^{-1}), and the ν_2 bands (493 and 502 cm^{-1}). In addition, the doped samples have a shoulder around 900 cm^{-1} as previously seen in the vanadium-doped $LiFePO_4$.[85, 101] $LiVOPO_4$ also has a band near 900 cm^{-1} associated with the vanadyl bond (See the blue dashed box in Figure 4.2). Since the vanadium is in an oxidation state (discussed further below) that does not form a V=O bond, we do not believe the shoulder observed in the vanadium-doped samples is due to a vanadyl bond. The FTIR spectra also confirm that the shoulder around 900 cm^{-1} is not associated with $Li_3V_2(PO_4)_3$, which is a common impurity formed while attempting to substitute vanadium into the olivine lattice.[83, 86-88, 92] Therefore, we believe it is unlikely that the observed differences in the spectra for the doped samples are caused by any impurity phase. The slight differences in the vibrational spectra and the shoulder seen near 900 cm^{-1} are likely due to minor changes in the local structure when cation vacancies are formed upon vanadium substitution.

XANES was used to determine the bulk oxidation state of vanadium and manganese in the samples. Figure 4.3a, which compares the V *K*-edge for $LiMn_{0.775}V_{0.15}\square$

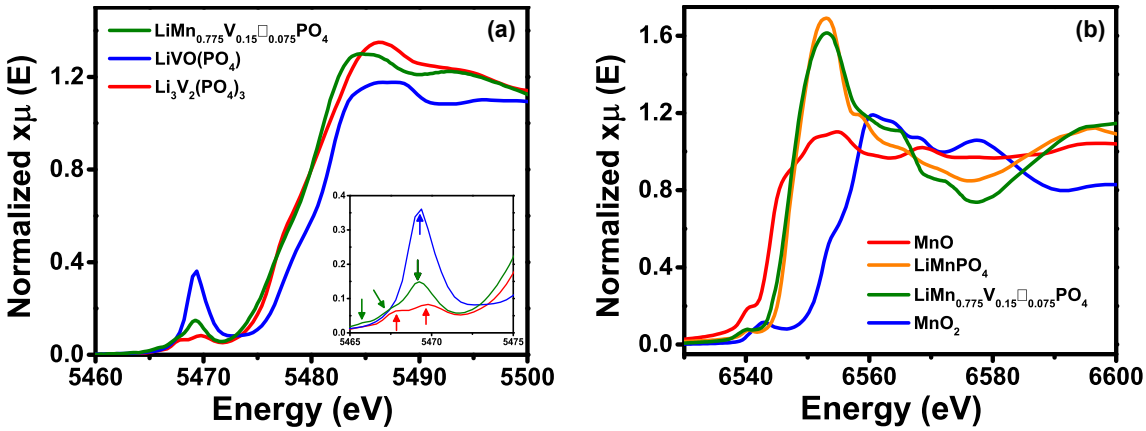

Figure 4.3. (a) V edge XANES data of $LiMn_{0.775}V_{0.15}\square_{0.075}PO_4$ with $Li_3V_2(PO4)_3$ and $LiVOPO_4$ shown as reference spectra for vanadium 3+ and 4+ oxidation state, respectively. Inset provided for a more detailed view of the pre-edge feature. (b) Mn edge XANES data of $LiMn_{0.775}V_{0.15}\square_{0.075}PO_4$ and $LiMnPO_4$ with MnO and MnO_2 shown as reference spectra for manganese 2+ and 4+ oxidation state, respectively.

$_{0.075}PO_4$, $LiVOPO_4$, and $Li_3V_2(PO_4)_3$, suggests a vanadium oxidation state of 3+ in the vanadium-doped $LiMnPO_4$ as the absorption edge is at an energy similar to that in $Li_3V_2(PO_4)_3$.[85, 89] The Mn edge (Figure 4.3b) in the undoped and vanadium-doped samples also match well, indicating that the oxidation state of Mn^{2+} is unaffected by the substitution of vanadium.

The pre-edge feature in the collected XANES data is indicative of distortion in the VO_6 octahedra (Figure 4.3a). The intensity of the peak increases as a result of stronger 3*d*-4*p* mixing and more overlap between metal 3*d* and ligand 2*p* orbitals caused by amplified distortion in the octahedra. As such, the intensity of the pre-edge feature for vanadium-

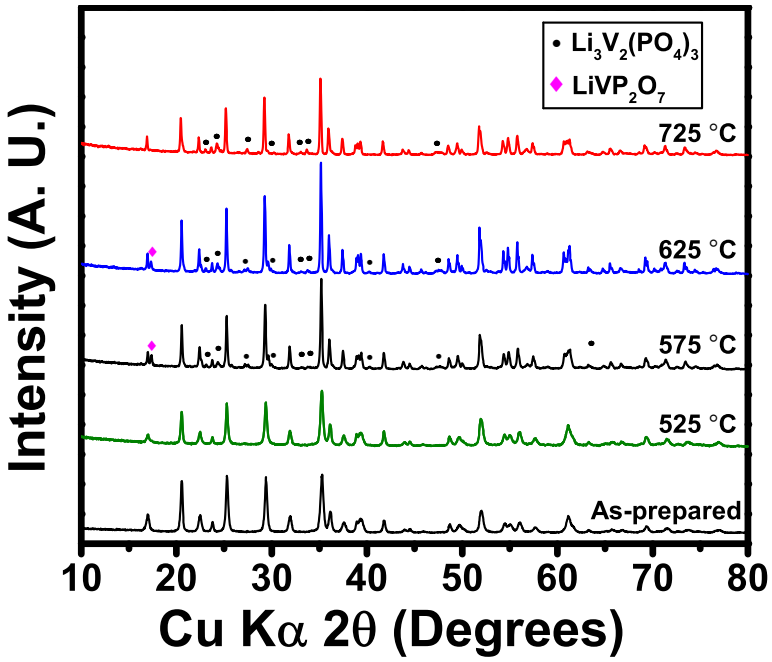

Figure 4.4. XRD patterns of the pristine and post-heated samples of $LiMn_{0.70}V_{0.20}\square_{0.10}PO_4$.

doped $LiMnPO_4$ (Figure 4.3a) suggests that the VO_6 octahedra are less distorted than that in $LiVOPO_4$, but more distorted than that in $Li_3V_2(PO_4)_3$. In addition, the pre-edge feature for the vanadium-doped $LiMnPO_4$ is characterized by a triplet peak (See inset of Figure 4.3a) as has been observed in vanadium-doped $LiFePO_4$.[89] The presence of multiple pre-edge peaks has been attributed to the simultaneous occurrence of dipole-allowed and quadrupole-allowed transitions.[102, 103] The pre-edge feature for $Li_3V_2(PO_4)_3$ is characterized by a double peak that has been identified as the crystal field splitting of the vanadium 3d orbitals into t_{2g} and e_g sets.[104, 105] The largest pre-edge feature was observed for $LiVOPO_4$ and it is due to the substantial distortion caused by the vanadyl bond in the VO_6 octahedra.

Our group previously demonstrated that the ability to dope higher levels of vanadium into the olivine lattice is directly related to the low-temperature MW-ST

synthesis process used.[11] Accordingly, we heated the $LiMn_{0.70}V_{0.20}\square_{0.10}PO_4$ sample to temperatures between 525 – 725 °C in 5% H_2 – 95% Ar for 6 h. XRD patterns for the heated and unheated samples are compared in Figure 4.4. The sample heated to 525 °C remains pure phase as no additional peaks are apparent after the heating process, which is consistent with the previous results with the vanadium-doped $LiFePO_4$ system.[85, 88] Upon heating to 575 °C and 625 °C, obvious impurity peaks corresponding to $Li_3V_2(PO_4)_3$ (major impurity) and $LiVP_2O_7$ (minor impurity) begin to show up in the XRD pattern. The formation of $Li_3V_2(PO_4)_3$ is expected as it is a common impurity observed when attempting to substitute vanadium into the olivine lattice by the conventional high-temperature processes.[84, 86-88] Yet, the amount of impurity observed is in slight contrast to the almost unnoticeable impurity peaks observed after post-heating the vanadium-doped $LiFePO_4$ to 625 °C.[85] The larger impurity peaks found in the vanadium-doped $LiMnPO_4$ suggests it is less stable at higher temperatures when compared to vanadium-doped $LiFePO_4$. Although the reason is unclear, the larger ionic radius difference between Mn^{2+} (0.83 Å vs. 0.78 Å for Fe^{2+}) and V^{3+} (0.64 Å) may play a role. After heating to 725 °C, the impurity peaks can be indexed to only one phase ($Li_3V_2(PO_4)_3$).

4.3.1Electrochemical Characterization.

The $V^{3+/4+}$ and $V^{2+/3+}$ redox couples have been reported to be active in vanadium-doped $LiFePO_4$ at 4.1 V and between 1.5 – 2.5 V, respectively.[85] An active $V^{3+/4+}$ couple in $LiMnPO_4$ would prove beneficial since the $Mn^{2+/3+}$ redox couple is active in the same voltage range. In the interest of also determining the activity of the $V^{2+/3+}$ and $V^{4+/5+}$ couples in $LiMnPO_4$, we expanded the voltage range from

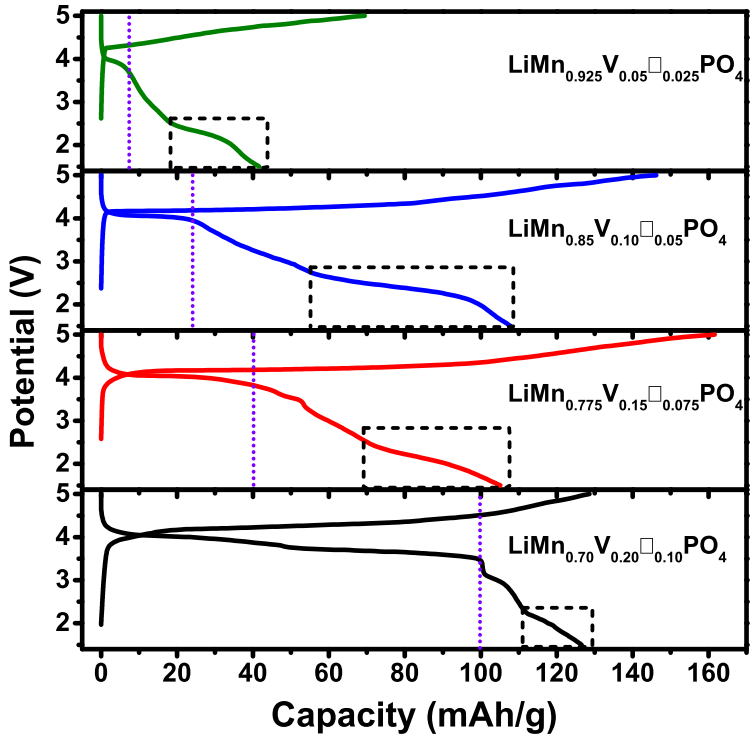

Figure 4.5. First charge/discharge curves for $LiMn_{1-3x/2}V_x\square_{x/2}PO_4$ (x = 0.05, 0.10, 0.15, and 0.20). The vertical dotted line indicates the capacity delivered near 4.1 V demonstrating the effect of the vanadium substitution. The capacity delivered between 1.5 – 2.5 V is attributed to vanadium redox couples.

1.5 to 5 V for the electrochemical characterization. Figure 4.5 shows the first charge-discharge curves for each of the vanadium-doped samples (x = 0.05, 0.10, 0.15, and 0.20). Several features change in the curves upon vanadium substitution.

Foremost, the vanadium substitution increases the capacity delivered at 4.1 V (shown by the location of the dotted vertical line) along with the total capacity. The maximum capacity achieved for the as-prepared vanadium-doped samples was ~ 130

mAh/g (x = 0.20 sample). Other reports have shown that substitution of Mn by other cations can improve the discharge capacity in the first cycle (~ 120 – 140 mAh/g), but in general, other optimization techniques have been employed simultaneously (*i.e.*, carbon coating or ball milling with conductive carbon after synthesis).[94, 97, 98, 99, 106, 107] The use of other optimization techniques in parallel with cation substitution makes the contribution of each method ambiguous. We did not optimize our samples with any of these techniques. Hence, the improved capacity observed for our samples can solely be attributed to the inclusion of vanadium and/or vacancies in the lattice. However, the capacity fades on cycling, and although *ex situ* PEDOT coating of the particles improved the discharge capacity in the first cycle, it did not improve the capacity fade (Figure 4.6).

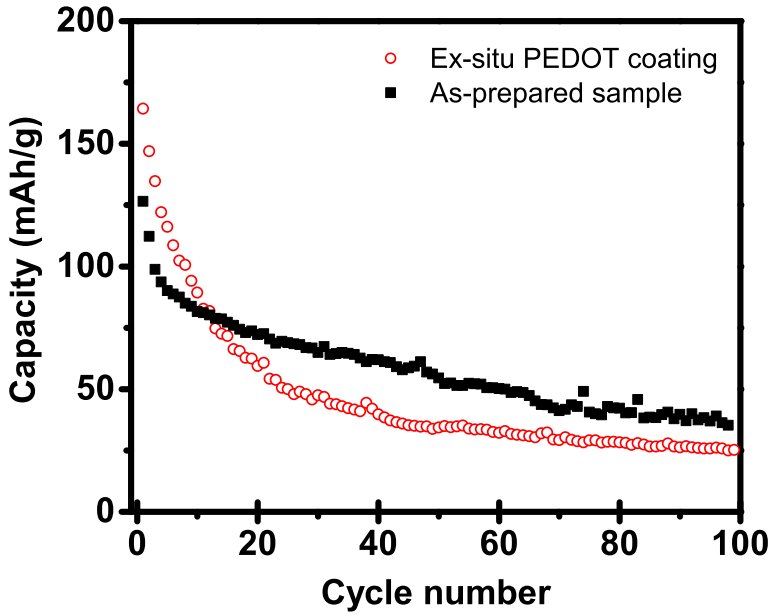

Figure 4.6. Cycling performance of the as prepared and *ex situ* coated $LiMn_{0.70}V_{0.20}\square_{0.10}PO_4$ sample.

Additionally, there is capacity delivered between 2.5 and 1.5 V (see dashed boxes in Figure 4.5) upon vanadium substitution. The capacity in the lower voltage region is the difference between the capacity delivered by the x = 0.05 sample (~ 40 mAh/g) and the undoped sample (~ 20 mAh/g). This capacity is most likely associated with the $V^{2+/3+}$ redox couple, as was shown for the vanadium-doped $LiFePO_4$.[85] The total capacity delivered by the x = 0.05, 0.15, and 0.20 samples in the lower voltage region is near or below the maximum possible $V^{2+/3+}$ contribution (~ 35 mAh/g). However, the capacity delivered by the x = 0.10 sample (~ 55 mAh/g) in the lower region is above the possible $V^{2+/3+}$ contribution. Therefore, it is likely that for the x = 0.10 sample, side reactions are contributing some of the capacity in the lower voltage region.

Site-disorder, where M (in LiMPO4) occupies the Li site, has been shown to occur in olivine materials synthesized at low-temperatures and to limit the amount of Li that can be extracted from the structure.[108] Because our samples were synthesized at a relatively low-temperature (< 300 °C), we investigated the possibility of site disorder playing a role in the low capacity delivered (15 mAh/g) by the undoped material. Therefore, we synthesized a second undoped material with a longer dwell time (1 h vs. 15 min) at the same temperature (280 °C). The discharge capacity did not increase significantly in the pristine sample with a 1 h dwell time (~ 20 mAh/g).

The improved capacity of aliovalently doped $LiMnPO_4$ may be associated with an additional conduction pathway (by vacancy formation) for Li^+ created upon vanadium substitution. The presence of vacancies in the lattice may provide an alternate route to bypass any Mn obstructing the diffusion of Li^+ ions and help improve the capacity. However, the comparison of the two pristine $LiMnPO_4$ samples (one obtained with a dwell time of 15 min and the other with 1 h) suggests that site disorder may not be a significant factor in causing the low capacity. This also insinuates that the significant

increase in capacity on substituting vanadium is beyond simply providing additional Li^+ conduction pathways by cation vacancies (see XAS section below).

Vanadium substitution also causes a noticeable slope in the discharge curve, which is most apparent in the x = 0.20 sample (Figure 4.5). This change might be expected since, in general, substitution leads to single-phase behavior.[109] Another key factor contributing to the change in the discharge curve is the formation of defects and cation vacancies,[109] which are inherent to the aliovalent doping of $LiMPO_4$ to maintain charge neutrality.[85, 88, 110, 111] There is also a distinct break in the continuity of the discharge curve for the x = 0.20 sample at ~ 3.8 V before it resumes in a sloping fashion down to ~ 3.45 V. This type of discontinuity implies an increase in reaction resistance as was shown to occur during the cycling of $NaFePO_4$,[112] although the exact origin is not known.

The defect chemistry in $LiMPO_4$ directly affects the resistance of Li^+-ion diffusion and is also temperature dependent.[35] Therefore, we tested the material heated to 525 °C (in 5% H_2 – 95% Ar for 6 h; See Figure 4.4) at C/20 rate. As seen in Figure 4.7, the discharge curve has the signature of the two-phase plateau of $LiMnPO_4$, suggesting the post-heating process improves the cation ordering/crystallinity of the material. The charge capacity in the first cycle (~ 156 mAh/g) is near the theoretical capacity (160 mAh/g assuming the $V^{3+/4}$ couple is active). The post-heated material demonstrates excellent Coulombic efficiency in the first cycle as ~ 155 mAh/g was delivered on discharge to 3.0 V. A significant amount of capacity (~ 60 mAh/g) was delivered upon further discharge to 1.5 V. Similar to the un-heated sample (x = 0.10), the $V^{2+/3+}$ couple only accounts for ~ 35 mAh/g of the capacity delivered in the lower-voltage region. This suggests that unwanted side reactions are contributing to the capacity in this lower region. The total discharge capacity delivered in the first cycle is near the theoretical capacity (~

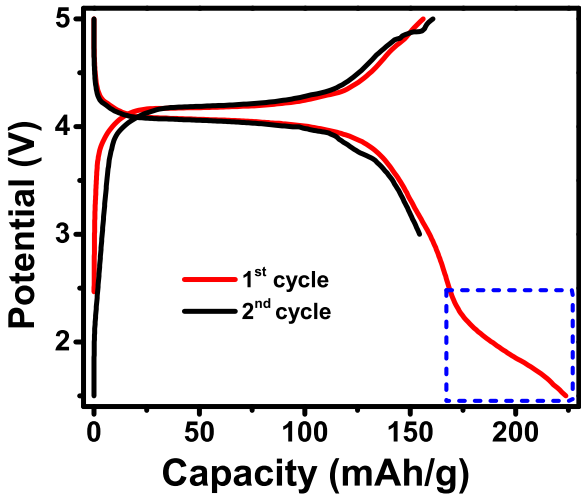

Figure 4.7. First and second charge/discharge curves for $LiMn_{0.70}V_{0.20}\square_{0.10}PO_4$ post-heated to 525 °C in in 5% H_2 – 95% Ar for 6 h. The first cycle was between 1.5 – 5 V; subsequent cycles were between 3 – 5 V. The capacity delivered between 1.5 – 2.5 V is attributed to vanadium redox couples.

230 mAh/g) with the scenario where all of the vanadium redox couples are active ($V^{2+/3+}$, $V^{3+/4+}$, and $V^{4+/5+}$).

During the second cycle, the lower voltage limit was changed to 3.0 V. The Coulombic efficiency dropped to 96 % as ~ 160 mAh/g was extracted and ~155 mAh/g was delivered upon discharge. There was a contribution to the charge capacity in the second cycle near 4.7 V as seen in Figure 4.7. By the fifth cycle, the discharge capacity dropped to ~ 100 mAh/g. The poor cyclability of the material was observed regardless of the lower voltage limit used in the first cycle (1.5 V vs. 3 V). *Ex-situ* XRD on an electrode of the post-heated sample after the 10th cycle (Figure 4.8) rules out structural degradation as the cause of the poor cyclability.

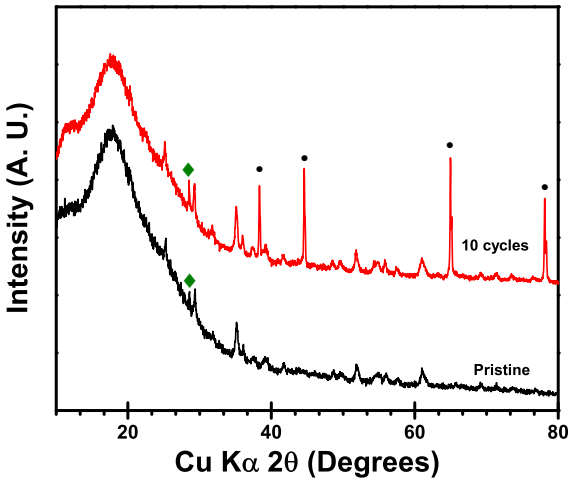

Figure 4.8. Ex-situ XRD of electrode with active material $LiMn_{0.70}V_{0.20}\square_{0.10}PO_4$ (heated to 525 °C) uncycled (Pristine) and after the 10th full cycle. The • indicate peaks attributed to the Al current collector. The ◆ indicate peaks that could not be indexed but believed to be associated with either the conductive carbon or PTFE used to make the electrode because peak was not present in XRD of the powder sample.

To study the kinetics of $LiMn_{1-3x/2}V_x\square_{x/2}PO_4$ (x = 0.0, 0.05, 0.10, and 0.15), EIS data were collected on fresh cells at OCV (Figure 4.9). All Nyquist plots consist of a semicircle in the high-to-medium frequency region, attributed to the complex charge-transfer process from the electrolyte to the electrode material. The semicircle is a combination of charge-transfer impedance and resistance of the electrode/electrolyte interface film. In addition, each Nyquist plot consists of the Warburg impedance associated with Li^+-ion diffusion in the bulk of the electrode (seen as a slope in the low frequency range). As shown in Figure 4.9a, the impedance associated with the charge-transfer process is greatly reduced upon vanadium substitution.

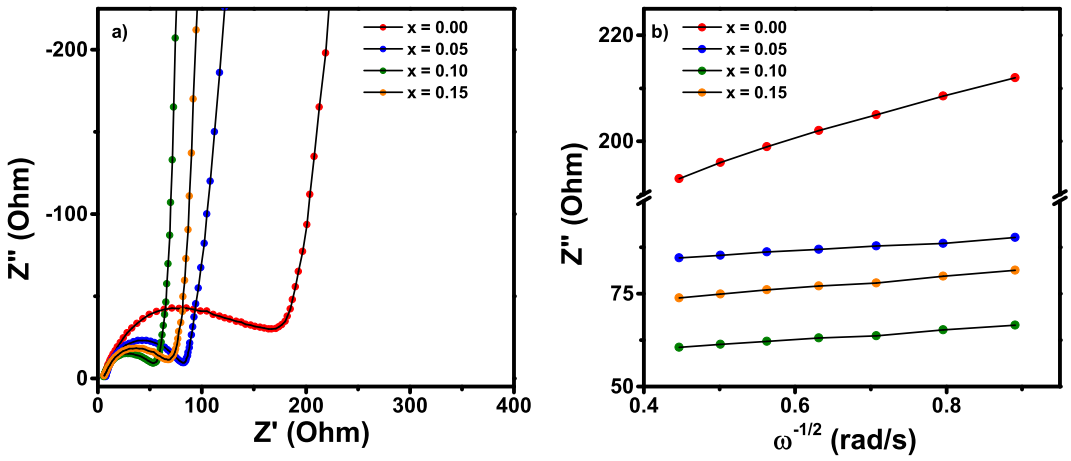

Figure 4.9. Electrochemical impedance spectra (EIS) for $LiMn_{1-3x/2}V_x\square_{x/2}PO_4$ (x = 0.05, 0.10, and 0.15) on fresh cells (OCV) at room temperature and linear fittings between real impedance (Z") and the reciprocal of the square root of the angular frequency in the low frequency region ($\omega^{-1/2}$) (slope of the lines used as the Warburg coefficient in the calculation of D_{Li^+}).

The lithium-ion diffusion coefficient (D_{Li^+}) was calculated using the following equation:

$$D_{Li^+} = \frac{R^2T^2}{2A^2n^4F^4C^2\sigma^2}$$

where R is the gas constant (8.314 J mol^{-1} K^{-1}), T is the absolute temperature (K), A is the contact area of the electrode, n is the number of electrons per molecule, F is the Faraday constant (96 486 C mol^{-1}), C is the concentration of Li ions (the ratio between the tap density of the prepared material and its molecular weight),[113] and σ is the Warburg coefficient (slope of the lines in Figure 4.9b). The D_{Li^+} value increased by an order of

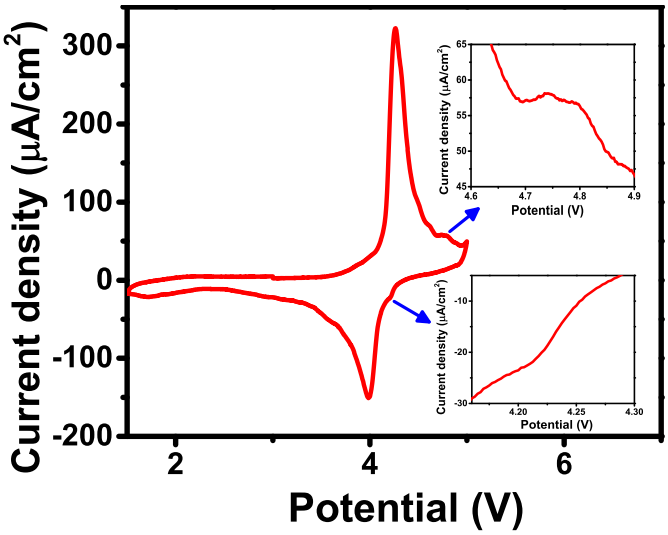

Figure 4.10. First cyclic voltammetry curve for $LiMn_{0.70}V_{0.20}\square_{0.10}PO_4$ post-heated to 525 °C in in 5% H_2 – 95% Ar for 6 h. Insets show enlarged portions of the curve for small peaks at 4.2 and 4.7 V.

magnitude upon vanadium substitution as shown in Table 4.3. The vacancies created upon aliovalent doping may contribute to the improvement in D_{Li^+} by providing additional pathways for lithium-ion diffusion during charge/discharge.

Table 4.3. Diffusion coefficient derived from EIS measurements of $LiMn_{0.70}V_{0.20}\square_{0.10}PO_4$ (x = 0.0, 0.05, 0.10, and 0.15)

Sample	D_{Li+}
$LiMnPO_4$	7.05×10^{-12}
$LiMn_{0.925}V_{0.05}PO_4$	8.68×10^{-11}
$LiMn_{0.85}V_{0.10}PO_4$	8.45×10^{-11}
$LiMn_{0.775}V_{0.15}PO_4$	7.91×10^{-11}

Cyclic voltammetry (CV) was also carried out on the material heated to 525 °C in order to provide insight into which redox couples are active (Figure 4.10). The cathodic and anodic peaks centered around 4.1 V are attributed to the $Mn^{2+/3+}$ and $V^{3+/4+}$ couples, since both are known to be active near the same voltage range and because the total capacity delivered between 3.0 and 5 V (~ 156 mAh/g) can only be accounted for if an additional redox couple (other than $Mn^{2+/3+}$) is active (either $V^{3+/4+}$ or $V^{4+/5+}$). Further activity is seen during charging (~ 4.76 V which coincides with the plateau seen in Figure 4.7) and upon discharge (~ 4.22 V). The cathodic peak becomes even more apparent in the second cycle similar to what occurred in Figure 4.7. The anodic peak is not as visible as it intersects with the larger peak associated with the $Mn^{2+/3+}$ (and $V^{3+/4+}$) couple. These additional peaks seen in the CV may correspond to the $V^{4+/5+}$ couple.

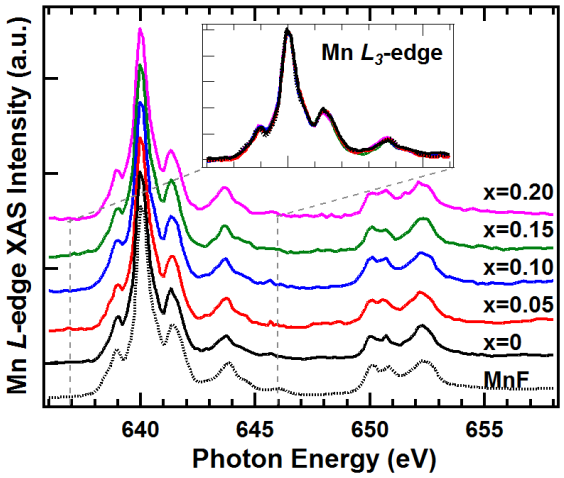

Figure 4.11. Mn *L*-edge XAS spectra of un-cycled (pristine) $LiMn_{1-3x/2}V_x\square_{x/2}PO_4$ (x = 0.0, 0.05, 0.10, 0.15, and 0.20) electrodes.

4.3.2 Soft X-ray Absorption Spectroscopy.

XAS has been used before to provide details about the changing electronic states of $LiFePO_4$ during lithiation.[114] Figure 4.11 shows the Mn *L*-edge XAS spectra of the undoped and doped $LiMnPO_4$ samples, which were collected in the surface-sensitive total electron yield (TEY) mode. The spectra consist of well-separated L_2 and L_3 absorption features, resulting from the *2p* core-hole spin-orbit splitting.[115] All the Mn-*L* XAS spectra collected on the un-cycled $LiMn_{1-3x/2}V_x\square_{x/2}PO_4$ (V = 0.00, 0.05, 0.10, 0.15, and 0.20) overlap with that of the MnF reference sample. This provides additional evidence, along with the XANES data, that V substitution does not affect the Mn oxidation state.

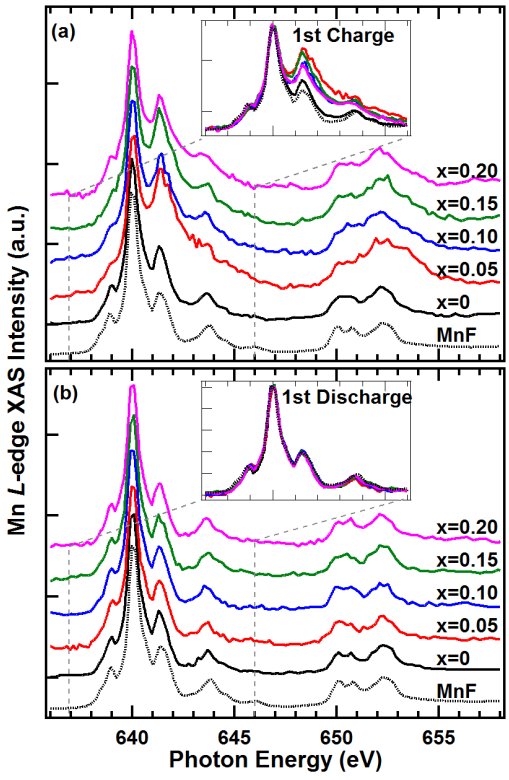

Figure 4.12. Mn *L*-edge XAS spectra of $LiMn_{1-3x/2}V_x\square_{x/2}PO_4$ (x = 0.0, 0.05, 0.10, 0.15, and 0.20) collected on the electrode after (a) 1st charge and (b) 1st discharge.

The Mn *L*-edge XAS spectra collected on the electrode after 1st charge display higher absorption intensity at 641.3 eV (Figure 4.12), indicating the oxidation of Mn^{2+} to Mn^{3+} during charging.[31] In particular, more Mn^{3+} is found in the vanadium-doped samples after 1st charge (see inset of Figure 4.12a), which suggests V substitution enhances the ability to charge (*i.e.*, oxidize Mn^{2+} to Mn^{3+}). However, the majority of the surface Mn stays in the 2+ state, which could be a contributor to the capacity fade during cycling as it has been linked to (i) the growth of the solid-electrolyte interphase film during cycling[116] and ii) the deposition of reaction products (*i.e.*, MnF_2 and LiF) on the surface of the electrode, increasing the interfacial impedance.[117-119]

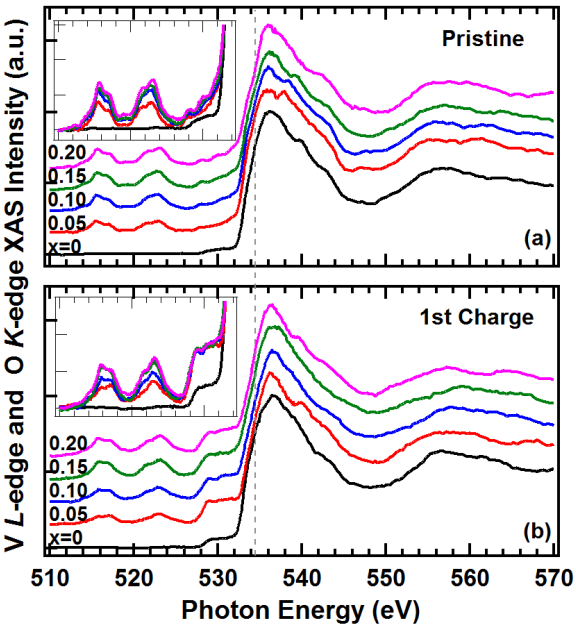

Figure 4.13. V *L*-edge and O *K*-edge XAS of $LiMn_{1-3x/2}V_x\square_{x/2}PO_4$ (x = 0.0, 0.05, 0.10, 0.15, and 0.20). The spectra were collected on the (a) un-cycled electrode (pristine) and (b) the electrode after 1st charge.

Figure 4.13 shows the V *L*-edge and O *K*-edge XAS spectra for the undoped and vanadium-doped $LiMnPO_4$ samples. XAS spectra were collected for each electrode sample in different states: uncharged (Figure 4.13a) and after 1st charge (Figure 4.13b). The XAS spectra in Figure 4.13 can be divided into two regions. The first region (510 – 525 eV) is attributed to the vanadium 2*p*-3*d* dipole transition.[120] The intensity of this region increases with vanadium substitution providing further evidence of vanadium incorporation into the lattice. The second region (525 – 570 eV) is attributed to the electron transition from oxygen 1*s* to oxygen 2*p* states, which is hybridized with metal 3*d* (525-531eV) and 4*s*,*p* (531-570eV) states.[120] The oxygen 2*p* and metal 3*d* hybridization feature (525-531eV) can provide important information on the covalence properties of the material.[31] In general, the delithiated samples (1st charge) show stronger metal 3*d*-O 2*p* hybridization than the lithiated ones (pristine and after 1st discharge), suggesting the extraction of lithium enhances the covalency of metal-oxygen bonds. Moreover, this hybridization feature is not apparent in the un-doped samples, but the intensity is obviously enhanced in the vanadium-substituted samples, providing evidence that the improved hybridization is due to the vanadium in the lattice. Hybridization between oxygen *p* and metal 3*d* orbitals has been shown to improve with a lower atomic number.[120] However, the enhancement on this hybridization feature is not dependent on the vanadium content, suggesting the improved hybridization is of Mn 3*d*-O 2*p* character. Thus, the vanadium substitution in $LiMnPO_4$ has enhanced the covalency of Mn-O bonding, leading to a more accessible $Mn^{2+/3+}$ couple during the initial cycling of the electrode, which is consistent with the Mn *L*-edge XAS results and the electrochemical performance.

4.3 CONCLUSIONS

We have shown that up to 20 atom % V^{3+} can be substituted for Mn^{2+} in $LiMnPO_4$ by employing a low-temperature microwave-assisted solvothermal synthesis process. The solubility of vanadium in $LiMnPO_4$ decreases upon heating the doped samples to ≥ 575 °C where impurity phases composed of vanadium begin to form. The discharge capacity in the first cycle is improved without any additional carbon coating by increasing the vanadium content in the material. The discharge capacity in the first cycle is further improved on post-heating (525 °C) the as-prepared sample, possibly due to the improvement in the cation ordering/crystallinity of the sample. Additionally, the overall kinetics is improved by means of lowering the charge-transfer impedance and increasing the lithium-ion diffusion coefficient upon vanadium substitution. From the XAS data provided, we are able to determine that the better performance is facilitated by enhanced Mn-O hybridization.

Chapter 5: Understanding the Effects of Cationic and Anionic Substitutions in Spinel Cathodes of Lithium-ion Batteries[2]

5.1 INTRODUCTION

The global demand for energy has reached epic proportions and is projected by the U.S Energy Information Administration (EIA) to continue to grow in the future. Efficient storage and utilization of electrical energy is critical if we are to exploit renewable energies like solar and wind to their full potential. In this regard, lithium-ion batteries are being intensely pursued as energy storage devices because they provide higher energy and power densities compared to other battery systems such as lead-acid and nickel metal – hydride batteries. In addition, they are also being pursued as a power source for transportation applications. Cost, safety, cycle life, and power capability are important criteria for these large battery applications. $LiMn_2O_4$ spinel as a cathode for lithium-ion batteries is appealing in this regard due to its lower cost and high rate capability. Yet severe capacity fade has plagued the spinel cathode and prevented it from becoming widely commercialized. Despite this, the spinel cathode has seen recent applications in electric vehicles, such as the Chevy Volt and Nissan Leaf, due to some of its attractive features. The capacity fade in $LiMn_2O_4$ cathodes has been attributed to many factors including loss of crystallinity,[121] Jahn-Teller distortion,[17, 122] manganese dissolution,[29, 123] a large lattice parameter difference between two cubic phases formed during the charge/discharge process,[124] particle microstructure,[125] and manganese valence.[126]

Many different approaches have been taken to improve the cyclability of the spinel cathode. The substitution of monovalent, divalent, and trivalent ions for

[2] This chapter is based on previously published work: A. Gutierrez and A. Manthiram, "Understanding the Effects of Cationic and Anionic Substitutions in the Spinel Cathodes of Lithium-ion Batteries," *Journal of The Electrochemical Society,* 160, A901 - A905 (2013). Dr. Manthiram supervised the project and A. G. performed all experiments.

manganese has been successfully used to decrease the capacity fade but with a sacrifice in capacity values.[127-130] Our group has shown that cation substitution followed by a partial substitution of fluorine for oxygen can increase the discharge capacity due to an increase in Mn^{3+} content,[131] while maintaining the improvement in capacity retention offered by the cationic substitutions; The cation-substituted oxy-fluoride spinels offer a combination of high capacity and good cyclability due to reduced Mn dissolution and a smaller lattice parameter difference between the two cubic phases formed during the charge/discharge process.[132] We present here a systematic investigation of (i) the amount of fluorine that can be substituted for oxygen before impurity phases form or performance degradation occurs and (ii) how the chemical characteristics of the dopants (electronegativity and dopant-oxygen bond dissociation energy) affect the electrochemical performance of the cathode materials.

5.2 EXPERIMENTAL

5.2.1 Material synthesis and characterization

The cation-doped $Li_{1.1}Mn_{1.8}M_{0.1}O_4$ and $Li_{1+x}Mn_{2-2x}M_xO_4$ (M = Al, Ti, Cr, Fe, Co, and Ni) spinel oxides were synthesized and subsequently fluorinated by a solid-state reaction as described in Chapter 2. All of the samples were characterized by X-ray diffraction (XRD) with Cu Kα radiation. A JEOL JSM-5610 SEM scanning electron microscope (SEM) was used to study the morphology. The average oxidation state of manganese was determined by a redox titration involving sodium oxalate ($Na_2C_2O_4$) and potassium permanganate ($KMnO_4$). The fluorine contents were calculated based on the oxidation state of manganese, employing charge neutrality and assuming the total anion (O + F) content to be 4.0. This assumption is reasonable as the oxygen non-stoichiometric range of cation-substituted spinels is negligible.[30]

The electrochemical performance was evaluated with 2032-type coin cells fabricated as described in Chapter 2. The electrochemical data were collected between 3.5 and 4.3 V at room temperature with an Arbin battery cycler at C/5 rate. The degree of manganese dissolution was evaluated by soaking the active material for 7 days at 55 °C in an electrolyte consisting of 1 M $LiPF_6$ in 1:1 ethylene carbonate/diethyl carbonate and determining the amount of manganese dissolved in the electrolyte by inductively coupled plasma (ICP) analysis (Chapter 2). It has been shown that Mn dissolution occurs at both the charged and discharged states. Gummow *et. al.*[28] showed that Mn dissolution occurs at lower potentials due to the higher concentrations of Mn^{3+}, while Jang *et. al.*[29] demonstrated that larger amounts of Mn dissolution occur at higher states of charge (SOC) due to the oxidative reactions that occur with the conductive additive (carbon) used to make the cathode. Since the purpose of our manuscript was to understand the role of the dopants on Mn dissolution, we chose to test the Mn dissolution of the unfluorinated-doped samples in the fully discharged state.

5.3 Results and Discussion

5.3.1 Crystal structure and morphology

The XRD patterns of all the spinel oxide and oxy-fluoride samples could be indexed with the space group Fd-3m.[133] Figure 5.1 gives the XRD patterns of some representative spinel and oxy-fluoride samples. The samples tend to form LiF impurities at higher fluorine contents as can be seen in the enlarged patterns shown on the right. The fluorine content at which the LiF impurity forms depends on the substituted cation. For example, LiF impurity is seen at fluorine contents of as low as 0.09 in $Li_{1.1}Mn_{1.8}Cr_{0.1}O_{3.91}F_{0.09}$ (Figure 5.1e). Figure 5.1d shows the unlfuorinated $Li_{1.1}Mn_{1.8}Cr_{0.1}O_4$ as a reference. With other substituent cations, LiF impurity is generally formed around or

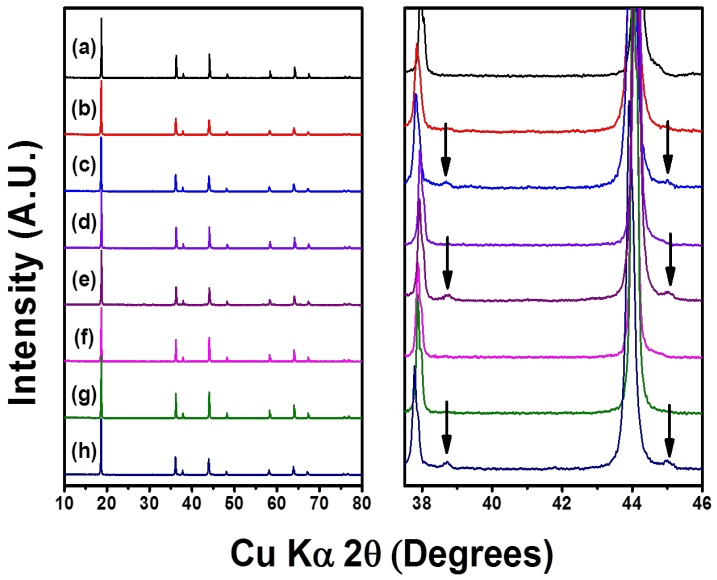

Figure 5.1. XRD patterns of (a) $Li_{1.1}Mn_{1.8}Al_{0.1}O_4$ (b) $Li_{1.1}Mn_{1.8}Al_{0.1}O_{3.83}F_{0.17}$ (c) $Li_{1.1}Mn_{1.8}Al_{0.1}O_{3.78}F_{0.22}$ (d) $Li_{1.1}Mn_{1.8}Cr_{0.1}O_4$ (e) $Li_{1.1}Mn_{1.8}Cr_{0.1}O_{3.91}F_{0.09}$ (f) $Li_{1.1}Mn_{1.8}Fe_{0.1}O_4$ (g) $Li_{1.1}Mn_{1.8}Fe_{0.1}O_{3.79}F_{0.21}$ (h) $Li_{1.1}Mn_{1.8}Fe_{0.1}O_{3.62}F_{0.38}$, with an enlargement of the pattern over a small 2θ region shown on the right. The LiF impurity peaks are indicated by the arrow.

above a fluorine content of 0.2. The unfluorinated Al-doped sample $Li_{1.1}Mn_{1.8}Al_{0.1}O_4$ (Figure 5.1a) and the oxy-fluoride sample $Li_{1.1}Mn_{1.8}Al_{0.1}O_{3.83}F_{0.17}$ with a fluorine content of 0.17 (Figure 5.1b) show no signs of LiF impurity. With increased fluorine substitution, the LiF impurity peaks are clearly seen (shown by the arrows) in the XRD pattern for the sample $Li_{1.1}Mn_{1.8}Al_{0.1}O_{3.78}F_{0.22}$ with a fluorine content of 0.22 (Figure 5.1c). A similar trend is also seen in the Fe-doped series as no LiF impurity peaks are seen in the unfluorinated spinel $Li_{1.1}Mn_{1.8}Fe_{0.1}O_4$ (Figure 5.1f) and oxy-fluoride sample

Table 5.1. Structural, chemical, and electrochemical data of the spinel manganese oxide and oxy-fluoride cathode materials.

Sample #	Composition	Mn oxidation state[a]	Initial capacity (mAh/g)	Capacity loss in 50 cycles (mAh/g)
1	$Li_{1.1}Mn_{1.8}Al_{0.1}O_4$	3.67	94.7	1.0
2	$Li_{1.1}Mn_{1.8}Al_{0.1}O_{3.99}F_{0.01}$	3.66	96.1	5.7
3	$Li_{1.1}Mn_{1.8}Al_{0.1}O_{3.89}F_{0.11}$	3.61	99.6	8.1
4	$Li_{1.1}Mn_{1.8}Al_{0.1}O_{3.86}F_{0.14}$	3.59	108.6	6.8
5	$Li_{1.1}Mn_{1.8}Al_{0.1}O_{3.83}F_{0.17}$	3.57	103	5.1
6	$Li_{1.1}Mn_{1.8}Al_{0.1}O_{3.78}F_{0.22}$ [b]	3.54	106.9	6.4
7	$Li_{1.1}Mn_{1.8}Al_{0.1}O_{3.72}F_{0.28}$	3.51	86.5	11.5
8	$Li_{1.125}Mn_{1.75}Co_{0.125}O_4$	3.71	85	0.46
9	$Li_{1.075}Mn_{1.85}Co_{0.075}O_{3.94}F_{0.06}$	3.59	111	3.8
10	$Li_{1.125}Mn_{1.75}Co_{0.125}O_{3.88}F_{0.12}$	3.65	93	1.8
11	$Li_{1.15}Mn_{1.7}Co_{0.15}O_{3.83}F_{0.17}$	3.66	91	0.9
12	$Li_{1.15}Mn_{1.7}Co_{0.15}O_{3.76}F_{0.24}$	3.62	104	1.4
13	$Li_{1.1}Mn_{1.8}Cr_{0.1}O_4$	3.67	92.8	0.78
14	$Li_{1.1}Mn_{1.8}Cr_{0.1}O_{3.98}F_{0.02}$	3.66	96.7	2.4
15	$Li_{1.1}Mn_{1.8}Cr_{0.1}O_{3.93}F_{0.07}$	3.63	96.5	2
16	$Li_{1.1}Mn_{1.8}Cr_{0.1}O_{391.}F_{0.09}$ [b]	3.62	96.6	2.9
17	$Li_{1.1}Mn_{1.8}Cr_{0.1}O_{3.87}F_{0.13}$	3.59	95.6	2.9
18	$Li_{1.1}Mn_{1.8}Cr_{0.1}O_{3.83}F_{0.17}$ [b]	3.57	109.6	13.5
19	$Li_{1.1}Mn_{1.8}Cr_{0.1}O_{3.79}F_{0.21}$ [b]	3.55	87	5.2
20	$Li_{1.1}Mn_{1.8}Fe_{0.1}O_4$	3.67	92.8	0.53
21	$Li_{1.1}Mn_{1.8}Fe_{0.1}O_{3.9}F_{0.1}$	3.61	91.7	4.1
22	$Li_{1.1}Mn_{1.8}Fe_{0.1}O_{3.82}F_{0.18}$	3.57	90.8	2.9
23	$Li_{1.1}Mn_{1.8}Fe_{0.1}O_{3.8}F_{0.2}$	3.56	93	2.2
24	$Li_{1.1}Mn_{1.8}Fe_{0.1}O_{3.77}F_{0.23}$ [b]	3.54	102	2.9
25	$Li_{1.1}Mn_{1.8}Fe_{0.1}O_{3.7}F_{0.3}$	3.5	101.6	6
26	$Li_{1.1}Mn_{1.8}Fe_{0.1}O_{3.67}F_{0.33}$ [b]	3.48	108.1	6.5
27	$Li_{1.1}Mn_{1.8}Fe_{0.1}O_{3.62}F_{0.38}$ [b]	3.46	103	10.4
28	$Li_{1.1}Mn_{1.8}Ni_{0.1}O_4$	3.72	82	0.03
29	$Li_{1.1}Mn_{1.8}Ni_{0.1}O_{3.9}F_{0.1}$	3.67	90	0.9
30	$Li_{1.1}Mn_{1.8}Ni_{0.1}O_{3.8}F_{0.2}$	3.61	104	0.9
31	$Li_{1.1}Mn_{1.8}Ni_{0.1}O_{3.71}F_{0.29}$	3.56	110	4.5
32	$Li_{1.1}Mn_{1.8}Ti_{0.1}O_4$	3.61	103	3.4
33	$Li_{1.1}Mn_{1.8}Ti_{0.1}O_{3.9}F_{0.1}$	3.56	109	11.3

[a]Calculated by assuming Li^+, Al^{3+}, Co^{3+}, Cr^{3+}, Fe^{3+}, Ni^{2+}, Ti^{4+}, and F^-.

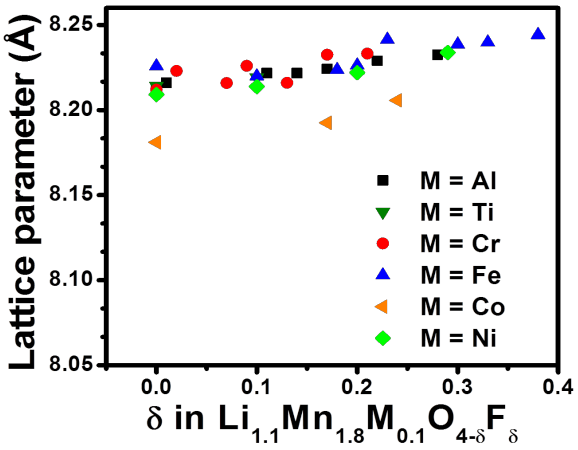

Figure 5.2. Variations of the lattice parameter with changing fluorine content in $Li_{1.1}Mn_{1.8}Al_{0.1}O_{4-\delta}F_{\delta}$ (M = Al, Ti, Cr, Fe, and Ni) and $Li_{1+x}Mn_{2-2x}M_xO_4$ (M = Co).

$Li_{1.1}Mn_{1.8}Fe_{0.1}O_{3.79}F_{0.21}$ with a fluorine content of 0.21 (Figure 5.1g), and a clear formation of impurity peaks is seen in the sample $Li_{1.1}Mn_{1.8}Fe_{0.1}O_{3.62}F_{0.38}$ with a fluorine content of 0.38 (Figure 5.1h). Not all of the samples fluorinated at or above a fluorine content of 0.2 showed evidence of LiF impurity formation although amorphous LiF could be present in small amounts on the surface due to the excess amount of fluorine precursor used to achieve the necessary substitutions. All samples that did show evidence of LiF impurity in the XRD pattern have been labeled in Table 5.1.

Figure 5.2 shows the variations of lattice parameter as a function of the fluorine content for each of the oxy-fluoride series. As seen from the shifts to lower 2θ, the lattice parameter increases with the incorporation of fluorine into the lattice. This is caused by the reduction of smaller Mn^{4+} ions (0.67 Å) into larger Mn^{3+} ions (0.79 Å) despite the replacement of larger O^{2-} ions (1.26 Å) by smaller F^{-} (1.19 Å) ions. The particle size (~ 600 nm) of the unfluorinated samples did not vary greatly with different dopants. In

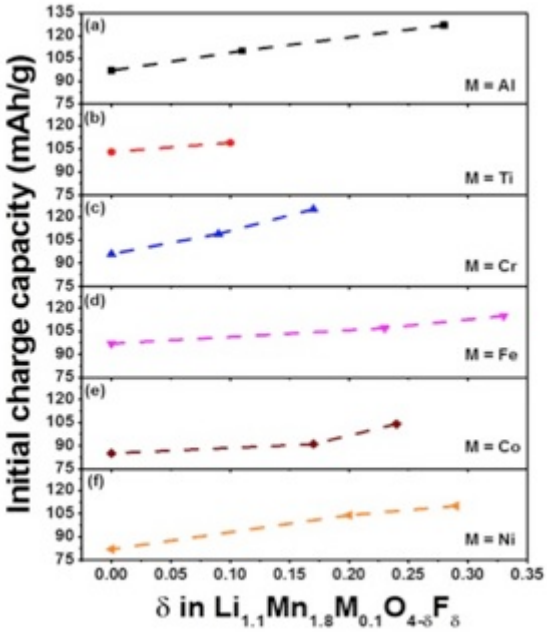

Figure 5.3. Initial charge capacity values of (a) $Li_{1.1}Mn_{1.8}Al_{0.1}O_{4-\delta}F_{\delta}$ (b) $Li_{1.1}Mn_{1.8}Ti_{0.1}O_{4-\delta}F_{\delta}$ (c) $Li_{1.1}Mn_{1.8}Cr_{0.1}O_{4-\delta}F_{\delta}$ (d) $Li_{1.1}Mn_{1.8}Fe_{0.1}O_{4-\delta}F_{\delta}$ (e) $Li_{1+x}Mn_{2-2x}Co_xO_{4-\delta}F_{\delta}$, and (f) $Li_{1.1}Mn_{1.8}Ni_{0.1}O_{4-\delta}F_{\delta}$ at room temperature with a C/5 rate.

addition, SEM data reveal that fluorine substitution did not alter the morphology or particle size of the samples.

5.3.2 Electrochemical performance

Figure 5.3 shows a general trend of increase in initial charge capacity for $Li_{1.1}Mn_{1.8}M_{0.1}O_{4-\delta}F_{\delta}$ (M = Al, Ti, Cr, Fe, and Ni) and $Li_{1+x}Mn_{2-2x}M_xO_{4-\delta}F_{\delta}$ (M = Co) as the fluorine content increases. The increase in capacity occurs due to the increase Mn^{3+} caused by the substitution of monovalent F^- for divalent O^{2-}. The maximum increase in charge capacity for each series resulting from the substitution of fluorine is 30, 6, 29, 18, 19, and 28 mAh/g, respectively, for M = Al, Ti, Cr, Fe, Co, and Ni.

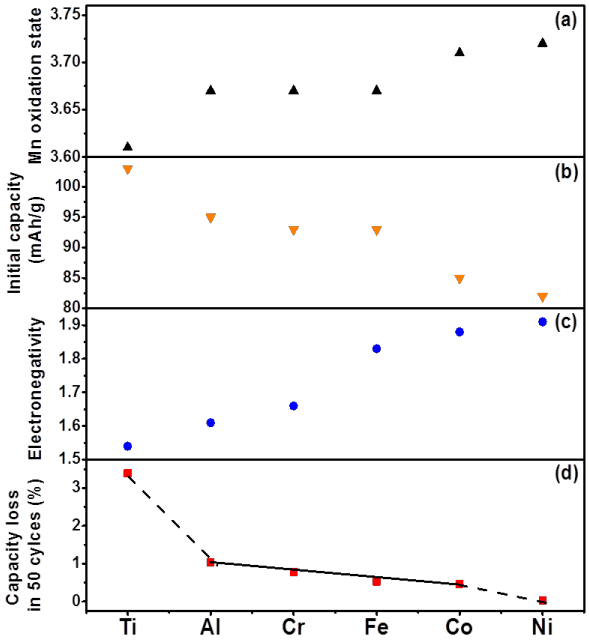

Figure 5.4. Variations of the (a) initial Mn oxidation state, (b) initial capacity, (c) electronegativity of M, and (d) capacity loss in 50 cycles of the un-fluorinated spinel cathodes $Li_{1.1}Mn_{1.8}M_{0.1}O_4$ (M = Al, Ti, Cr, Fe, and Ni) and $Li_{1+x}Mn_{2-2x}M_xO_4$ (M = Co).

Figure 5.4 summarizes the variation of manganese oxidation state, initial capacity values, electronegativity of the dopant and the capacity loss in 50 cycles for the unfluorinated samples ($Li_{1.1}Mn_{1.8}M_{0.1}O_4$ (M = Al, Ti, Cr, Fe, and Ni) and $Li_{1+x}Mn_{2-2x}M_xO_4$ (M = Co)). The initial capacity values shown in Figure 5.4b decrease as the oxidation state of manganese increases (Figure 5.4a) as a result of the decreasing oxidations state of the dopant cation M^{n+} from 4+ to 3+ to 2+. For example, $Li_{1.1}Mn_{1.8}Ti_{0.1}O_4$, $Li_{1.1}Mn_{1.8}M_{0.1}O_4$ (M = Al, Cr, and Fe), and $Li_{1.1}Mn_{1.8}Ni_{0.1}O_4$ samples show initial

capacities of, respectively, ~ 103, 95, and 82 mAh/g since Ti exists as Ti^{4+}, M = Al, Cr, and Fe exist as M^{3+}, and Ni exists as Ni^{2+}.

As seen in Figure 5.4d, the capacity fade decreases drastically on going from M = Ti to M = Al due to an increase in the Mn oxidation state. Interestingly, among the trivalent M^{3+} dopants, the capacity fade decreases with increasing electronegativity (shown in Figure 5.4c) despite the same oxidation state for Mn (Figure 5.4a). The capacity fade trend deviates again on going from the trivalent dopants to the divalent Ni^{2+} due to an increase in Mn oxidation state. Consequently, the M = Ni sample shows the least and close to zero capacity fade due to 1) a significantly higher oxidation state of Mn and 2) the highest electronegativity of Ni among the dopants investigated here.

Figure 5.5 compares the capacity fade in 50 cycle of the fluorinated samples $Li_{1.1}Mn_{1.8}M_{0.1}O_{4-\delta}F_{\delta}$ with M = Al, Cr, Fe, and Ni. Each series exhibits an "average capacity fade" (taken as the average of all samples before any significant jump occurs – represented by the dashed line in Figure 5.5) before experiencing a jump and steady increase. The "average capacity fade" in each series can be taken as a measure of the stability of the doped cathode. Figure 5.5 clearly demonstrates two important points: (i) the "average capacity fade" remains nearly constant in each series (before the jump) despite the changing manganese valence, and (ii) the "average capacity fade" value is different for each doped-series. These two points suggest that something in addition to the manganese valence plays a role in the capacity fade. Among the four series shown in Figure 5.5, the M = Al, Cr, and Fe (3+ cations) series all have different values for the "average capacity fade" despite having the same Mn valence when equally fluorinated. The M = Ni (2+ cation) series shows the lowest "average capacity fade" due to a higher Mn valence compared to the Al, Cr, and Fe series. A closer examination of the data in

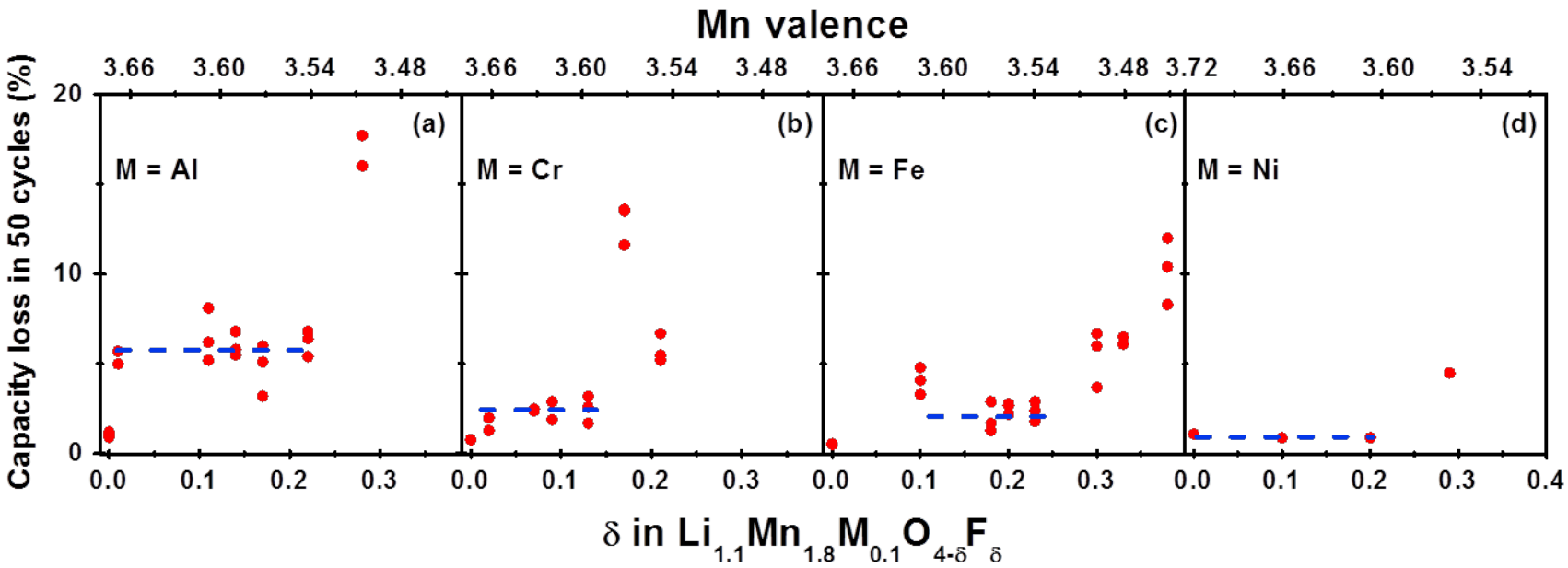

Figure 5.5. Variations of the capacity loss in 50 cycles with fluorine content in (a) $Li_{1.1}Mn_{1.8}Al_{0.1}O_{4-\delta}F_{\delta}$ (b) $Li_{1.1}Mn_{1.8}Cr_{0.1}O_{4-\delta}F_{\delta}$ (c) $Li_{1.1}Mn_{1.8}Fe_{0.1}O_{4-\delta}F_{\delta}$ and (d) $Li_{1.1}Mn_{1.8}Ni_{0.1}O_{4-\delta}F_{\delta}$.

Fig. 5 also reveals that a jump in capacity fade occurs when the Mn valence drops below about 3.6. This is consistent with our earlier study, which demonstrated that when the initial Mn valence is > 3.6, the lattice strain produced during cycling is reduced, resulting in maintenance of good structural integrity.[126]

Figure 5.6 shows the "average capacity fade" (shown with dashed line in Figure 5.5) of each series along with the variations of the electronegativity of M, bond dissociation energy of M-O, and Mn dissolution from un-fluorinated $Li_{1.1}Mn_{1.8}M_{0.1}O_4$ (M = Al, Ti, Cr, Fe, and Ni). As seen in Figure 5.6a, the "average capacity fade" decreases with increasing electronegativity (Figure 5.6b) and decreasing bond dissociation energy (Figure 5.6c). It is well established that the electronegativity of M and O can be used to describe the homolytic (symmetric) bond dissociation energy D of M-O through Pauling's equation as:

$$D[M-O] = \frac{1}{2}(D[M-M] + D[O-O] + 23(\chi[M] - \chi[O])^2 \qquad (1)$$

where the bond dissociation energy of the M-O bond is given by a covalent term and a polar term. The covalent term D[M-M] + D[O-O] expresses the ability of M and O to share their electrons, while the polar term $(\chi[M] - \chi[O])^2$ expresses the imbalanced sharing of bonding electrons between M and O. In view of Eqn. 1, we can understand the inverse relationship between the electronegativity of M (the dopant cation) and the bond dissociation energy of M-O. More simply stated, as the electronegativity of the doped cation M^{n+} increases, the metal-oxygen bond becomes more covalent. This increased covalent character can enhance the electronic conductivity. In addition, the perturbation of the Mn-Mn interaction by M (the dopant ions) along with the increased covalence of

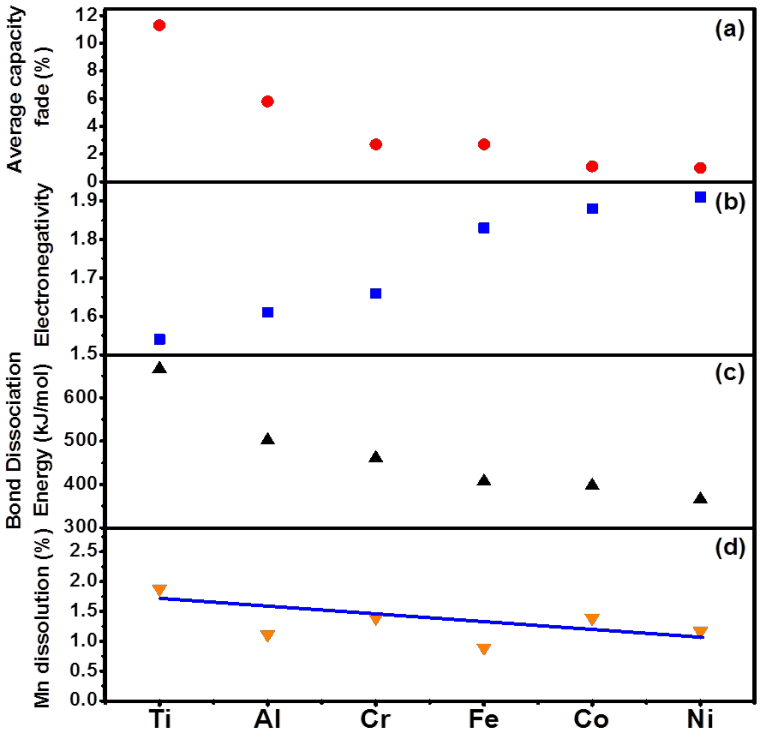

Figure 5.6. Variations of (a) average capacity fade of the oxy-fluoride spinels (values taken from the dashed line in Figure 5.5), (b) electronegativity of the dopant cation M^{n+}, (c) bond dissociation energy of the M-O bond, and (d) manganese dissolution from $Li_{1.1}Mn_{1.8}M_{0.1}O_4$ (M = Al, Ti, Cr, Fe, and Ni) and $Li_{1+x}Mn_{2-2x}M_xO_4$ (M = Co). The data in (b) and (c) were taken from the CRC Handbook of Chemistry and Physics, 91st Edition, 2010-2011.

the M-O bond could also suppress the disproportionation reaction below and thereby decrease the Mn dissolution:

$$2Mn^{3+} \rightarrow Mn^{4+} + Mn^{2+} \qquad (2)$$

Figure 5.6d provides evidence for this theory as the Mn dissolution decreases with increasing electronegativity of M (*i.e.* increasing covalence of the M-O bond, Figure 5.6b). In addition, the "average capacity fade" decreases with decreasing Mn dissolution.

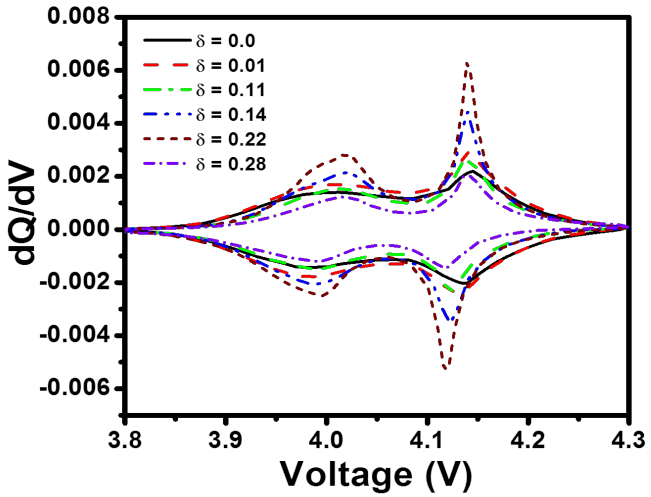

Figure 5.7. Variations of the dQ/dV vs. voltage curves of $Li_{1.1}Mn_{1.8}Al_{0.1}O_{4-\delta}F_{\delta}$ with various fluorine content. The difference between the cathode and anodic peaks increases as more fluorine is substituted into the spinel structure.

5.3.3 Kinetics

Figure 5.7 shows the dQ/dV vs. voltage plots of $Li_{1.1}Mn_{1.8}Al_{0.1}O_{4-\delta}F_{\delta}$. The peaks in the anodic region centered at ~ 4.03 and ~ 4.15 V correspond to the extraction of lithium ions from the 8a tetrahedral sites of the spinel lattice, and the peaks in the cathodic region at ~ 3.98 and ~ 4.13 V correspond to the insertion of lithium ions back into the lattice. As seen in Figure 5.7, the potential difference between the anodic and cathodic peaks increases as the fluorine content increases. Figure 5.8 plots the potential difference vs. fluorine content for the M = Al, Cr, and Fe series, and it reveals that the potential

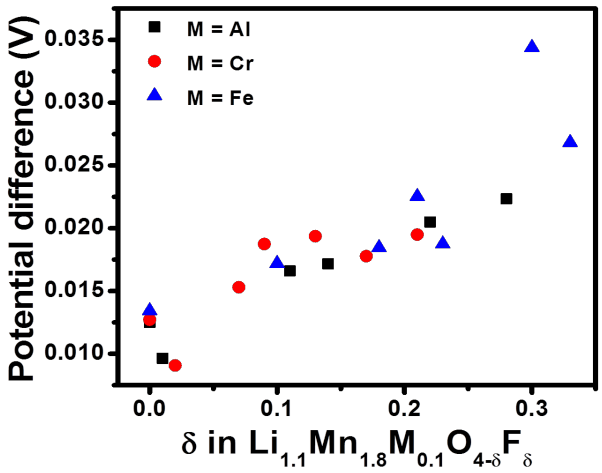

Figure 5.8. The potential difference between the anodic and cathodic peaks in the dQ/dV curves with changing fluorine content in $Li_{1.1}Mn_{1.8}Al_{0.1}O_{4-\delta}F_{\delta}$, $Li_{1.1}Mn_{1.8}Cr_{0.1}O_{4-\delta}F_{\delta}$, and $Li_{1.1}Mn_{1.8}Fe_{0.1}O_{4-\delta}F_{\delta}$.

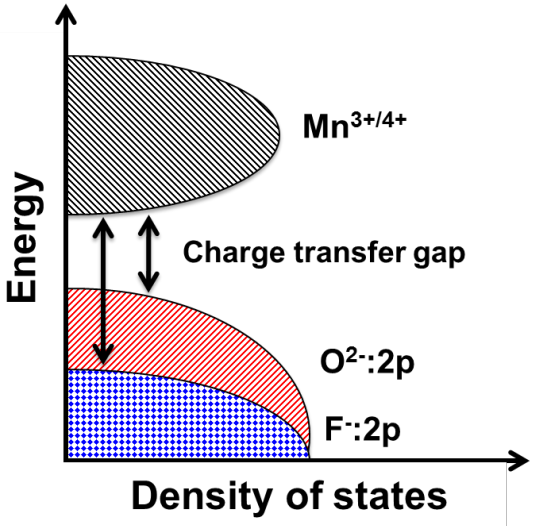

Figure 5.9. Schematic energy level diagram showing the positions of the top of the O^{2-}:2p and F^{-}:2p bands relative to that of the $Mn^{3+/4+}$:3d band.

difference increases in each series with increasing fluorine content, which suggests that the reaction kinetics worsen as the fluorine content is increased.[134] As the fluorine content increases, the degree of covalence and electronic conductivity decrease due to an increasing charge transfer gap between the anion: 2p band and the metal: 3d band (Figure 5.9), resulting in a larger polarization. Because a slight excess of the fluorine precursor was used to achieve the needed substitution, part of the polarization may be occurring due to the amorphous LiF, which may be on the surface of the particles.

5.4 CONCLUSIONS

Several oxy-fluoride spinel cathode samples $Li_{1.1}Mn_{1.8}M_{0.1}O_{4-\delta}F_{\delta}$ and $Li_{1+x}Mn_{2-2x}M_xO_{4-\delta}F_{\delta}$ with M = Al, Ti, Cr, Fe, Co, and Ni have been synthesized and characterized with an aim to understand the role of cationic and anionic dopants on the electrochemical performance. Generally, LiF begins to form as an impurity at or above a fluorine content of ~ 0.2. In each series, the capacity fade increases drastically when the Mn valence decreases below ~ 3.6. At a given dopant content of M, the capacity fade is found to decrease with (i) decreasing oxidation state of M^{n+} due to an increase in the Mn oxidation state, (ii) increasing electronegativity of M and decreasing bond dissociation energy of M-O due to the increased metal-oxygen covalence and electronic conductivity, and (iii) decreasing Mn dissolution. As the fluorine content increases, the charge-discharge kinetics worsens as indicated by an increased separation between the potentials of the charge and discharge peaks due to a decreasing metal-oxygen covalence and electronic conductivity caused by the substitution of more electronegative fluorine for oxygen. Overall, the study demonstrates how the dopant characteristics influence the electrochemical performance of spinel cathodes, which could become beneficial in choosing the appropriate dopants to maximize the electrochemical performance.

Chapter 6: Surface Segregation of Cations in Spinel Cathode Materials

6.1 INTRODUCTION

The demand for more reliable energy storage for large-scale applications continues to grow as we search for ways to utilize green energy technologies more efficiently. Lithium-ion batteries are appealing because of their higher power and energy density values when compared to other battery systems. Safety and cost are also important criteria to consider. The spinel $LiMn_2O_4$ cathode is attractive in this regard due to the lower cost and environmentally friendliness of its constituents. In addition, the spinel cathode has high rate capability facilitated by its three dimensional pathway for lithium-ion diffusion. Nevertheless, wide commercialization of the spinel cathode has not occurred on account of the severe capacity fade that occurs during cycling, especially at elevated temperatures.

The capacity fade has been attributed to various mechanisms including dissolution of Mn^{2+} ions into the electrolyte during cycling. Inert oxides have been successfully used as coatings on the surface of the particles in order to reduce the extent of dissolution. One drawback with this approach is the need for additional synthesis steps to coat the particles. Our group has recently suggested that surface segregation may improve the performance of spinel cathodes used for lithium-ion batteries.[135] The segregation of certain cations to the surface during synthesis is appealing because it would minimize the additional synthesis steps required in coating the particles with oxides. In addition, surface segregation of certain ions may aid in improving the capacity fade during cycling of the material. Accordingly, we present in this Chapter an investigation of how the processing route affects the surface segregation of dopants in $Li_{1.1}Mn_{1.8}M_{0.1}O_4$ (M = Al, Cr, Fe, Co, Ni, and Cu) spinel materials. Additionally, we examine the effect of surface segregation on the electrochemical performance. We find that the ionic radius of the

dopant with respect to Mn is what controls the amount of surface segregation. In addition, we conclude that the capacity fade of the material increases when the M/Mn ratio is further away from the expected bulk value.

6.2 EXPERIMENTAL

6.2.1 Material synthesis and characterization

The cation-doped $Li_{1.1}Mn_{1.8}M_{0.1}O_4$ (M = Al, Cr, Fe, Co, Ni, and Cu) spinel oxides were synthesized by a solid-state reaction as described in Chapter 2. Each sample was post-heated at 700 °C for an additional 96 h in air. All of the samples were characterized by X-ray diffraction (XRD) with Cu Kα radiation.

The depth profiles of elemental concentrations were determined by TOF-SIMS as described in Chapter 2.

The electrochemical performance was evaluated with 2032-type coin cells fabricated as described in Chapter 2. The electrochemical data were collected between 3.5 and 4.3 V at room temperature and at 55 °C with an Arbin battery cycler at C/5 rate.

6.2 RESULTS AND DISCUSSION

6.2.1 Elemental depth profile

All XRD peaks for the $Li_{1.1}Mn_{1.8}M_{0.1}O_4$ (M = Al, Cr, Fe, Co, Ni, and Cu) samples could be indexed with the space group Fd-3m. With TOF-SIMS analysis, the relative concentration of an element can be measured at various sputtering depths with respect to its own concentration in the bulk (*i.e.* at large sputtering times, where the secondary ion yield of the species under investigation is constant) provided that the ionization probability remains constant for most of the depth profile. The matrix effects, responsible for the ionization probability variations at the surface, are reduced to a few tens of seconds of sputtering as observed from the depth profiles of contaminants and given the

minimal change in the surface work function following the initial surface implantation of bismuth ions. Consequently, the actual surface values of all species of interest were considered after discarding the first 20 seconds of each profile to account for contamination and matrix effects. A depth profile (not shown) of each $Li_{1.1}Mn_{1.8}M_{0.1}O_4$ (M = Al, Cr, Fe, Co, Ni, and Cu) sample (pristine and annealed) was measured for 2500 seconds (where the secondary ion yield was constant) of sputtering time where the depth was estimated to be ≥ 12.5 nm.[136] The normalized depth profiles provide a semi quantitative value for surface-to-bulk normalized ratios of the secondary ion yields representing each of the cations in the doped samples as a function of sputtering time (*i.e.* bulk normalized depth profiles).[137] These secondary ion yield ratios provide a relative measure of the enhancement or depletion of an element at the surface with respect to the bulk. An absolute determination of elemental concentration was not possible due to the lack of appropriate reference samples.

A more informative way to understand how the surface concentrations in the spinel structure change with the processing is by looking at how the cation ratios at the surface compare to what is expected in the bulk (accomplished by using the collected depth profiles). Two distinct types of segregation have been identified in the literature: equilibrium and non-equilibrium.[138] The driving force for equilibrium segregation is the minimization of surface free energy.[139] Non-equilibrium segregation occurs by the diffusion of atom-vacancy (vacancies created during high temperature processing) complexes to the surface during cooling where annihilation of the vacancies occurs.[140] It has been suggested that ageing of the material and slow cooling rates can rid a sample of non-equilibrium segregation, which helps to distinguish which type of segregation is occurring. In other words, equilibrium segregation is determined by materials properties whereas non-equilibrium segregation is determined largely by experimental procedures.

Therefore, our pristine samples (800 °C – 48 h dwell) were re-heated to 700 °C with a dwell time of 96 h to determine if the amount of segregation would change, which would suggest non-equilibrium segregation is occurring. Figure 6.1 summarizes the measured dopant-to-manganese ratios at the surface of each of the samples (pristine and annealed), and the dashed pink line indicates the expected bulk ratio. As shown in Figure 6.1, in general the M/Mn ratios do not change when the sample is annealed with the exception of the Cu-doped sample. The ratios Co/Mn, Ni/Mn and Cu/Mn are higher than what is

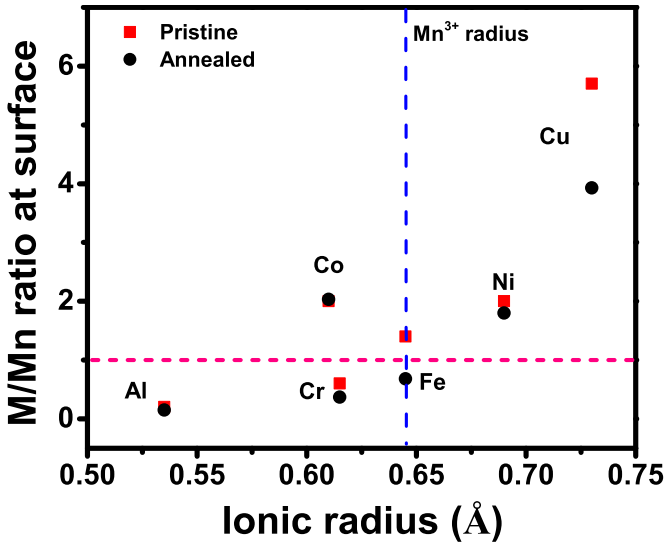

Figure 6.1. The ratio of dopant (M) to manganese in the Li1.1Mn1.8M0.1O4 samples synthesized at 800 °C for 48 h (designated as pristine) and post-heated at 700 °C for an additional 96 h (designated as annealed).

expected in the bulk. The Al/Mn and Cr/Mn ratios are slightly below the expected value while the Fe/Mn ratio is close to the expected bulk value. It is necessary to point out that because the dopant concentration is low in each sample, small changes in the distribution throughout the particle will lead to unmistakable deviations from the expected dopant-to-

Mn ratios in the bulk. With this in mind, we can conclude that in each of the samples, the dopant is enriched in varying degrees on the surface when compared to Mn. However, it is important to clarify that the term enriched refers to an increase from the expected concentration, and does not imply that the dopant is the most abundant cation in that region. Figure 6.1 also demonstrates that the M/Mn ratio increases along with the ionic radius of M, with Co being the only exception to the trend. As shown in Figure 6.1, when the ionic radius of M is smaller than the ionic radius of Mn^{3+} (indicated as blue dashed line in Figure 6.1) the M/Mn ratio is below the expected value. In contrast, when the ionic radius of M is larger than the ionic radius of Mn^{3+} the M/Mn ratio is greater than the expected value. In the sample where Fe is used as the dopant, the M/Mn ratio is near the expected value as the ionic radii of Mn and Fe are nearly the same. Therefore, we conclude that the ionic radius of the dopant controls the surface segregation amount in the spinel materials. In addition, we conclude that the concentration of M on the surface is occurring through equilibrium segregation, on account of the fact that the M/Mn ratios are not significantly changing upon annealing the materials.

6.2.2 Electrochemical performance

The electrochemical performances of the $Li_{1.1}Mn_{1.8}M_{0.1}0_4$ (M = Al, Cr, Fe, Co, Ni, and Cu) samples at room temperature and 55 °C are summarized in Figure 6.2. At room temperature, the cyclability of each of the samples appears, in general, unaffected by the differences in surface concentration of the dopant, with the Cu-doped sample being the exception. The M/Mn ratio of the Cu-doped sample was the highest and furthest from the expected bulk value. Nevertheless, it is difficult to conclude that the higher M/Mn ratio in the Cu-doped sample is causing the inferior cyclability. The cycling data at 55 °C provides added information on how the different M/Mn ratios might play a role in the

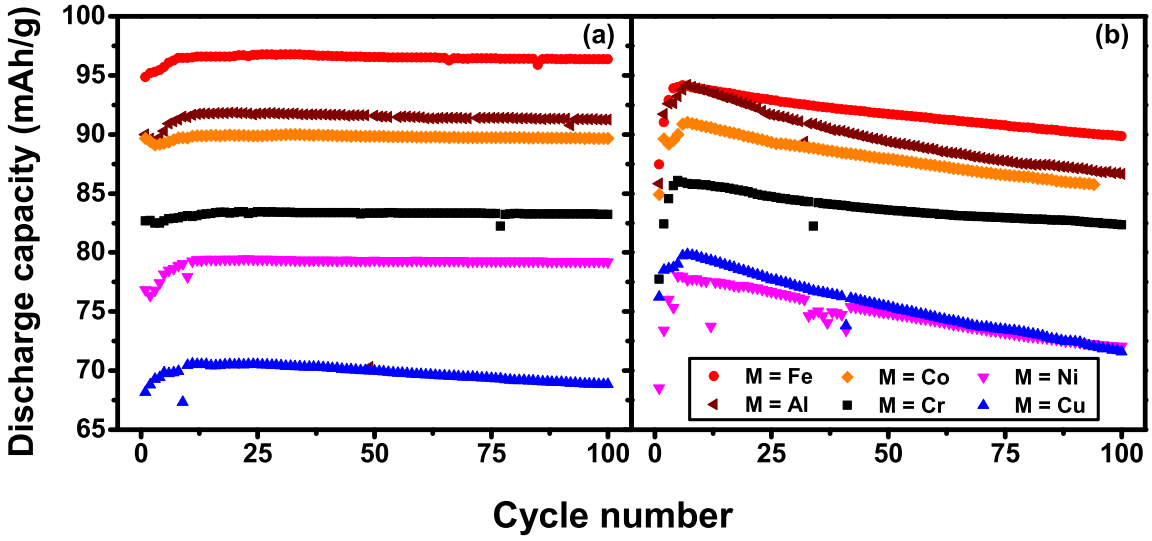

Figure 6.2. Cycling data of the pristine $Li_{1.1}Mn_{1.8}M_{0.1}O_4$ (M = Al, Cr, Fe, Co, Ni, and Cu) samples at (a) 25 °C and (b) 55 °C.

performance as the capacity fade is varying in each of the samples. The Cr, Fe, and Co-doped samples have similar capacity fade (determined by the slope of the cyclability curves) while the Al, Ni, and Cu-doped samples exhibit increased capacity fade in comparison to former samples. It is noted that the samples exhibiting higher capacity fade during cycling (Al, Ni, and Cu) also have M/Mn ratios furthest away from the expected value (see Figure 6.1).

A comparison of the cycling data at 55 °C for the pristine and annealed samples is shown in Figure 6.3. In general, the capacity fade is higher in the annealed samples as can be seen by the greater slope of the cyclability curves when compared to the pristine samples. It is not clearly understood what is causing the difference in performance, since the M/Mn ratios were similar in the pristine and annealed samples. On a closer look at the cycling data for the annealed samples, it is evident that samples with M/Mn ratios closer to the expected value perform better. For example, the capacity fade for the annealed Al,

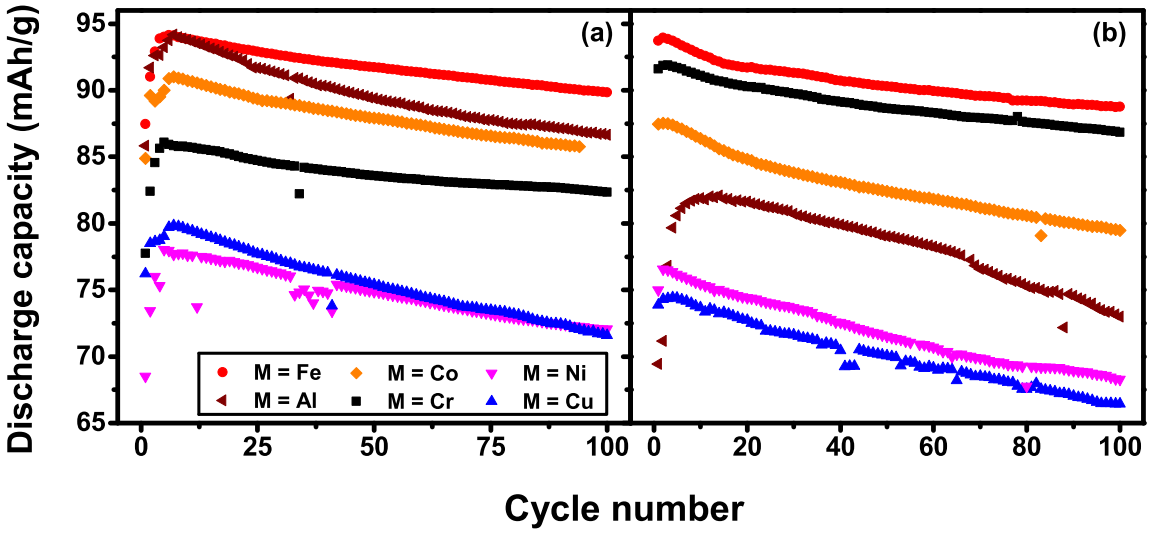

Figure 6.3. Cycling data collected at 55 °C of the $Li_{1.1}Mn_{1.8}M_{0.1}O_4$ (M = Al, Cr, Fe, Co, Ni, and Cu) samples: (a) pristine and (b) annealed samples.

Co, Ni, and Cu samples is worse than the annealed Cr and Fe samples. As shown in Figure 6.1, the M/Mn ratios for the Cr and Fe samples are closest to the expected value, indicated by the pink dashed line.

6.3 CONCLUSIONS

We presented here an investigation of how the processing of $Li_{1.1}Mn_{1.8}M_{0.1}O_4$ (M = Al, Cr, Fe, Co, Ni, and Cu) spinel oxides affects the surface concentration of M on the particles of the samples. We found that annealing the samples does not drastically change the M/Mn ratio on the surface, suggesting that the concentration of M is controlled by the tendency to reduce the surface free energy of the particles (*i.e.*, equilibrium segregation). We also concluded that the ionic radius of M, compared to the ionic radius of Mn, controls the amount of surface segregation that occurs during processing. Subsequent

electrochemical tests suggest that the cycling performance of the samples is better when the M/Mn ratio is closer to the expected bulk value.

Chapter 7: Microwave-assisted solvothermal synthesis of MV_2O_4 (M = Mg, Fe, Mn, and Co)

7.1 INTRODUCTION

The AV_2O_4 spinel oxides consisting of A^{2+} and V^{3+} ions exhibit interesting electrical and magnetic properties.[141] Particularly, their electronic properties can be tuned by altering the V-V distance across the edge-shared octahedral framework by changing the size of the A^{2+} counter cations. Of particular interest to solid state physicist and chemists is the possibility of tuning the ratio between the electronic hopping and intra-atomic Coulomb energy U by changing the size of the A^{2+} ions in AV_2O_4.[141, 142]

However, the synthesis of oxides containing lower-valent V^{3+} ions requires reactions of the component oxides in a reducing or inert gas atmosphere (*e.g.*, H_2, Ar-H_2 mixture, N_2-H_2 mixture, Ar, or N_2) or sealed tubes under vacuum at elevated temperatures (≥ 800 °C). These reactions often require prolonged reaction times (e.g., several hours to days) at high temperatures with repeated intermittent grindings as V_2O_3 is refractory with a high melting temperature.[143-145] Unfortunately, ions like Co^{2+} can get easily reduced to the metallic state (*e.g.,* Co metal) at those elevated temperatures, resulting in an inaccessibility of the spinel phase.

Interestingly microwave-assisted solvothermal (MW-ST) reactions in a suitable solvent can offer desired products at relatively lower temperatures within a short reaction time (*e.g.*, within minutes).[100, 146-155] Due to the much lower reaction temperatures involved, the MW-ST processes can also provide access to metastable phases that are otherwise inaccessible by high-temperature processes, as has been, for example, shown recently by the facile reduction of transition-metal oxides with tetraethylene glycol (TEG) as a reducing agent.[156]

We present here a rapid MW-ST process in TEG medium employing precursor solutions for synthesizing the AV_2O_4 (Mg, Fe, Fe, and Co) spinel oxides within a short time of 30 min at a low temperature of 300 °C. The method exploits the reducing strength of TEG and the low energy levels of the cations in solution before the formation of the AV_2O_4 crystals. Subsequent post-heat treatment of the AV_2O_4 samples in an inert or reducing atmosphere at elevated temperatures demonstrates the advantage of the low-temperature MW-ST method as oxides like CoV_2O_4 gets reduced to give Co metal at high temperatures.

7.2 EXPERIMENTAL

AV_2O_4 (M = Mg, Fe, Mn, and Co) samples were prepared via a microwave-assisted solvothermal process as described in Chapter 2.

The chemical compositional analysis was carried out by inductively coupled plasma (ICP) analysis as described in Chapter 2. X-ray powder diffraction (XRD) data were collected with a Rigaku Ultima IV instrument with Cu Kα radiation. Scanning electron microscopy (SEM) images and elemental dot maps were carried out with a Hitachi S5500 SEM/STEM microscope with energy dispersive spectroscopic (EDS) capability.

7.3 RESULTS AND DISCUSSION

7.3.1 Microwave-assisted synthesis

Conventional heating is a slow and inefficient method for transferring energy to a reaction mixture because it depends on convective heating and on the thermal conductivity of the precursors and products involved in the reaction. On the other hand, microwave-assisted synthesis is efficient at uniformly heating the whole liquid volume through two main mechanisms: dipolar polarization and ionic conduction.[157] The

molecular dipoles in the solvent realign themselves with the oscillating electric field and lose energy in the form of heat through molecular friction and dielectric loss. In a similar fashion, under the influence of an oscillating electric field, charged particles collide with atoms and molecules in the solution and generate heat.

The loss tangent (tan δ) of a material or solvent quantifies its ability to convert microwave energy into heat. A solvent with a high loss tangent value is required for efficient heating but solvents with moderate to low microwave absorptivity can also be used for synthesis. When choosing a solvent for microwave synthesis other relevant properties must also be considered. Several solvents were investigated in the synthesis of AV_2O_4 (Mg, Mn, Fe, and Co) to demonstrate this: deionized (DI) water, polyethylene glycol (PEG), and TEG. Although the hydrothermal process is the most commonly used method to generate oxides in solvent-based reactions,[157] the use of deionized water as the solvent resulted in a mixture of cobalt and vanadium oxide phases (*e.g.*, V_6O_{13}, and Co_3O_4). The mixed cobalt and vanadium oxides that formed were higher valent oxides of vanadium as indicated by the above formulas, suggesting that water is not a strong enough reducing agent under these conditions to obtain the desired V^{3+} oxides. In addition, the maximum temperature achieved when using DI water was 240 °C, which may have played a role in the inability to successfully form AV_2O_4. Polyethylene glycol (PEG) has also been used to assist in the formation of transition-metal oxides in microwave-assisted processes.[158, 159] Even though a higher reaction temperature was achieved (300 °C) when using PEG as the solvent, the solid that formed during the reaction was amorphous.

The higher boiling point (> 300 °C) and reducing strength of TEG combined to facilitate the formation of the lower-valent vanadium spinel oxides AV_2O_4. Figure 7.1a shows the XRD patterns of AV_2O_4 (A = Mg, Mn, Fe, and Co) synthesized in TEG at 300

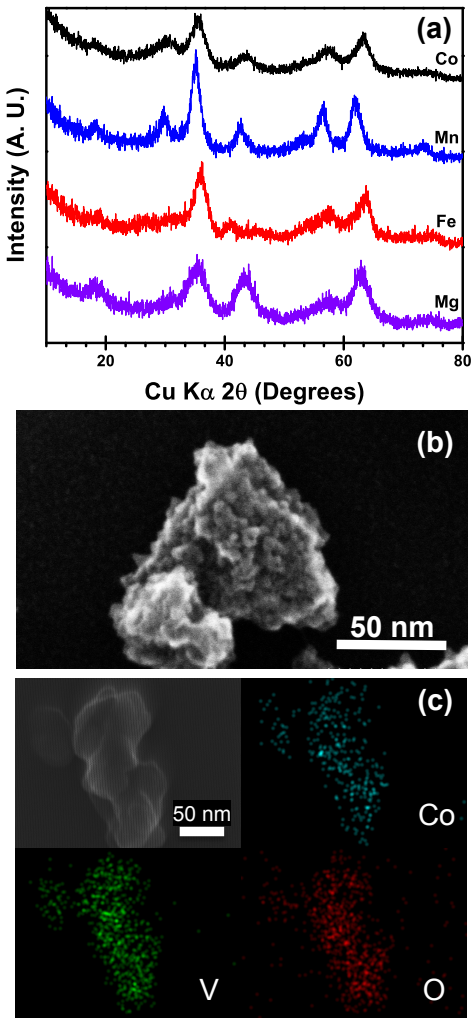

Figure 7.1. (a) XRD patterns of AV_2O_4 (A = Mg, Mn, Fe, and Co) synthesized by the MW-ST method at 300 °C for 30 min in TEG solvent; (b) SEM image representing the morphology of each of the AV_2O_4 samples synthesized by the MW-ST method at 300 °C for 30 min in TEG; (c) EDS mapping of elements on CoV_2O_4, showing a homogenous distribution.

°C for 30 min. The broad peaks are a result of the small crystallite size (Figure 7.1b). The samples formed secondary particles in the range of 75 – 100 nm made up of primary

particles between 5 - 10 nm in diameter. With the exception of the FeV_2O_4 sample, all peaks in the samples could be indexed to Fd-3m. The XRD pattern of the intended FeV_2O_4 sample showed impurity phases, in which Fe and V were in higher valence states (Fe_2O_3 and VO_2), in addition to the peaks for FeV_2O_4. We mapped several particles in each of the samples and found the distribution of the elements to be homogenous (Figure 7.1c). The ICP analysis (Table 7.1) indicated the elemental ratios in each of the samples were near the expected values.

Table 7.1. Elemental ratios obtained from ICP analysis

Sample	V/A[a]
MgV_2O_4	1.99
MnV_2O_4	2.01
FeV_2O_4	1.97
CoV_2O_4	1.98

[a]Error in ICP ratios is estimated to be around 2 – 3 %

Our group has demonstrated previously that the ability to reduce transition-metal oxide (solid) suspensions in a solvent through a microwave-assisted method is dependent on the location of the highest occupied molecular orbital (HOMO) of the solvent in reference to the energy of the redox couple in the oxide.[156] The current work exploits the energy of the cations in solution, which is lower than that in solids, before they combine to form AV_2O_4. Figure 7.2a provides a schematic of how the energy levels shift due to larger electrostatic potentials (Madelung energy) that arise when ions are brought together to form the crystal solid. The Madelung potential is approximated by treating the

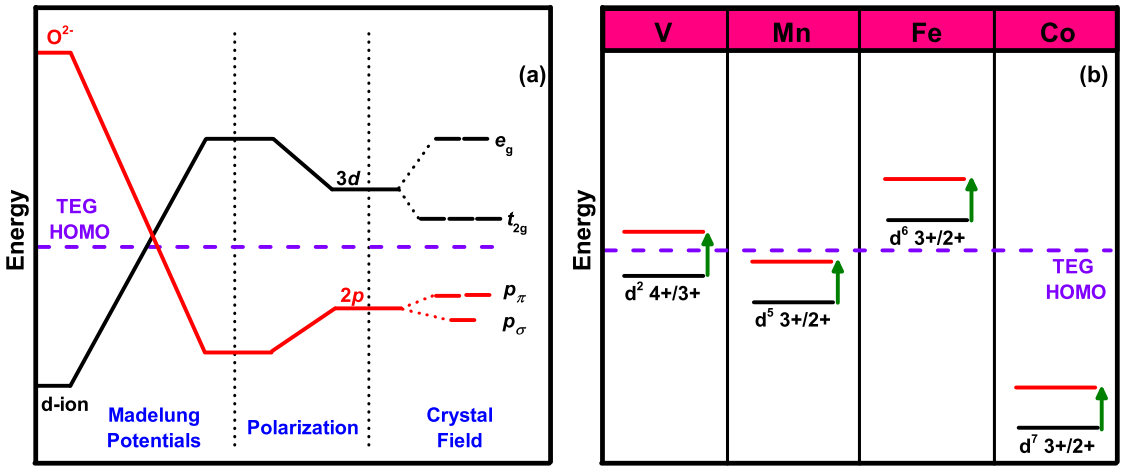

Figure 7.2. (a) Qualitative energy diagram summarizing the parameters that influence the M:3*d* and O:2*p* energy levels, with the energy levels of the ions in solution shown on the left of the diagram. (b) Energy diagram depicting the location of the cation energy levels in reference to the HOMO in TEG in solution (black line) and after the crystalline solid is formed (red line).

ions in the lattice as point charges. The negative charge on the oxide ions produces a *repulsive* Madelung potential at the cation sites, which decreases the effective ionization energy (raises the energy level) of the electrons in the cation. The positive charge on the cations provides an *attractive* Madelung potential at the oxygen site, which lowers the energy level of the oxygen below that of the cations. The effect of polarization brings the energy levels closer together as shown. When the crystal is formed, the oxide ions surrounding the cations constitute a crystal field around the cations and split the d-orbitals into t_{2g} and e_g levels. The oxide ions experience an axial crystal field and the *p*-orbitals of oxygen are classified as either sigma (p_σ) or pi (p_π) bonding.

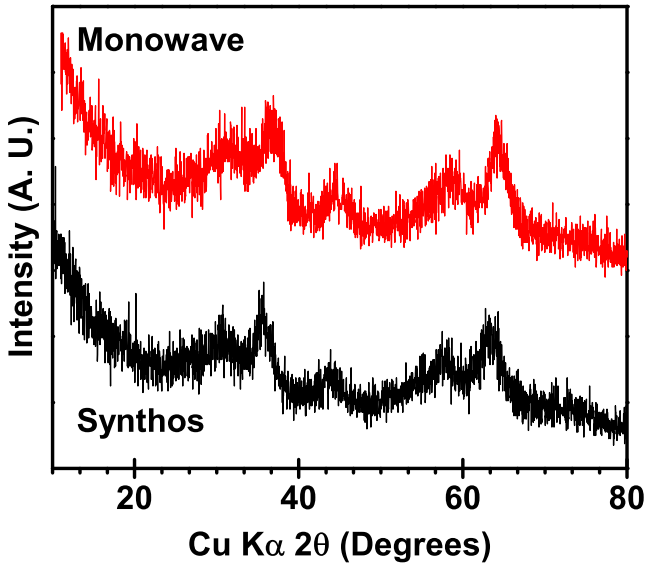

Figure 7.3. XRD patterns of CoV_2O_4 synthesized in the Synthos 3000 and Monowave 300 microwave reactor systems at 300 °C and held for 30 min.

Figure 7.2b depicts the energy levels of the cations in solution and in the solid with respect to the HOMO in TEG. The $V^{3+/4+}$ and $Mn^{2+/3+}$ couples are similar in energy as evidenced by our recent work in vanadium-doped phosphate cathode materials, where the redox potential of $V^{3+/4+}$ and $Mn^{2+/3+}$ were shown to be the same (~ 4.1 vs. Li/Li^+).[85] As described above, the energy level for $V^{3+/4+}$ in solution is slightly lower than the HOMO in TEG, which allows access to V^{3+} and the formation of AV_2O_4. After the crystal structure forms, the $V^{3+/4+}$ energy level shifts above the HOMO in TEG making the 3+/4+ couple inaccessible in the solid as has been shown previously by our group.[156] The $Mn^{2+/3+}$ and $Co^{2+/3+}$ energy levels lie below the HOMO in TEG for both the solid and solution as both redox couples are accessible in the solid[156] and in solution (this work). Even with the shift to a lower energy in solution, the $Fe^{2+/3+}$ couple is above the HOMO, making it

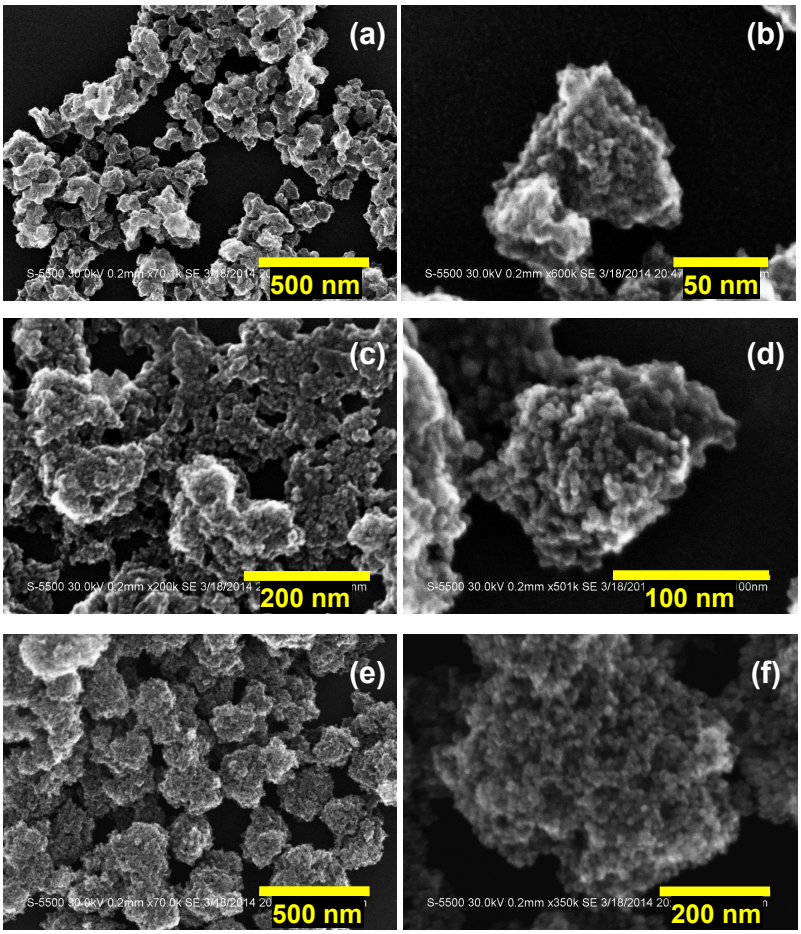

Figure 7.4. SEM images for CoV_2O_4 synthesized in the Synthos 3000 microwave reactor system at 300 °C and held for various times: (a and b) 30 min, (c and d) 2 h, and (e and f) 4 h. The images in b, d, and f are at higher magnifications for the samples, respectively, in a, c, and e.

inaccessible as evidenced by the difficulty in obtaining the pure FeV_2O_4 phase directly from the MW-ST synthesis; it consisted of the impurity phases Fe_2O_3 and VO_2.

We attempted to improve the crystallinity of the samples obtained by the MW-ST process by increasing the hold time for the MW-ST reaction. Due to the safety limits

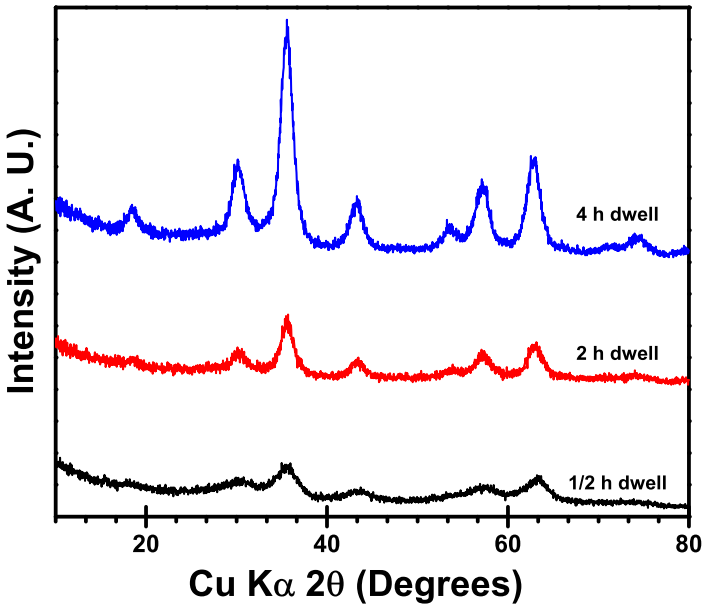

Figure 7.5. XRD patterns of CoV_2O_4 synthesized in the Synthos 3000 microwave reactor system at 300 °C and held for different dwell times.

inherent to the Monowave 300 reactor system, longer dwell times (> 30 min) at 300 °C are not possible. Therefore, the experiments for testing the effect of dwell time of the reaction were carried out in a Synthos 3000 microwave reactor. A preliminary run was carried out to ensure that comparable results would occur in each of the reactors. The similar XRD patterns and morphology (respectively, Figure 7.3 and 7.4) for CoV_2O_4 synthesized at 300 °C for 30 min in the Synthos and Monowave systems suggest that any differences are negligible.

The AV_2O_4 samples were synthesized in the Synthos at 300 °C with a hold time of 30 min, 2 h, and 4 h. As seen in Figure 7.5, the XRD peaks for the samples are sharper and more easily resolved as the dwell time increases. The size of the secondary particles for the material also grew with increasing dwell time. Nevertheless, there is no further growth of the primary particles as they remain between 5 – 10 nm in diameter (Figure

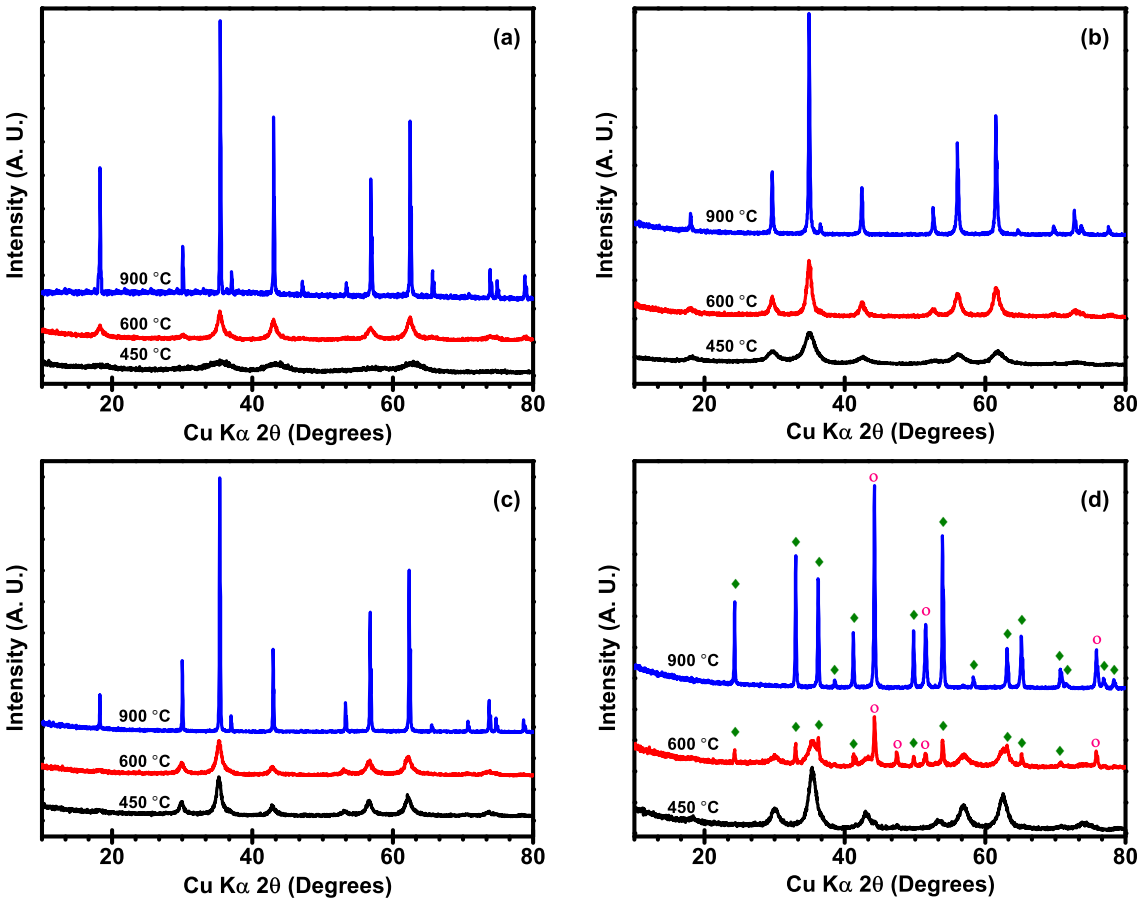

Figure 7.6. XRD patterns of (a) MgV_2O_4, (b) MnV_2O_4, (c) FeV_2O_4, and (d) CoV_2O_4 post-heated to 450 °C, 600 °C, and 900 °C in 5% H_2 – 95 % Ar for 12 h. The ◆ indicates V_2O_3 impurity and o indicates cobalt impurity.

7.4) even when the dwell time was increased eight times longer than the shortest dwell time (4 h vs. 30 min). Several studies have demonstrated that microwave irradiation accelerates both the nucleation and crystal growth of materials,[160, 161] but with a more pronounced effect on the nucleation stage.[160] Our results provide further validation that microwave heating is more efficient in the nucleation stage compared to crystal growth, as the primary particles remained unchanged by the longer dwell time.

7.3.2 Post-heat treatment

Each of the AV_2O_4 samples (synthesized in the Monowave 300 reactor) was also subjected to post-heat treatments to improve the crystallinity. The first treatment was carried out under 5 % H_2 – 95 % Ar atmosphere for 12 h at 450 °C, 600 °C, and 900 °C (Figure 7.6). As expected, the XRD peaks became sharper at higher temperatures. The MgV_2O_4, MnV_2O_4, and FeV_2O_4 samples remained pure phase even at 900 °C while the CoV_2O_4 sample began to disproportionate into Co metal and V_2O_3 at temperatures as low as 600 °C. By 900 °C, no spinel peaks were observed in the CoV_2O_4 (Figure 7.6d) sample. The as prepared MgV_2O_4, MnV_2O_4, and FeV_2O_4 samples were also heated at 900 °C for 3 h. All XRD peaks (Figure 7.7) could be indexed to the spinel structure for MnV_2O_4, but the FeV_2O_4 and MgV_2O_4 samples had V_2O_3 impurity phase present with the shorter dwell time of 3 h at 900 °C.

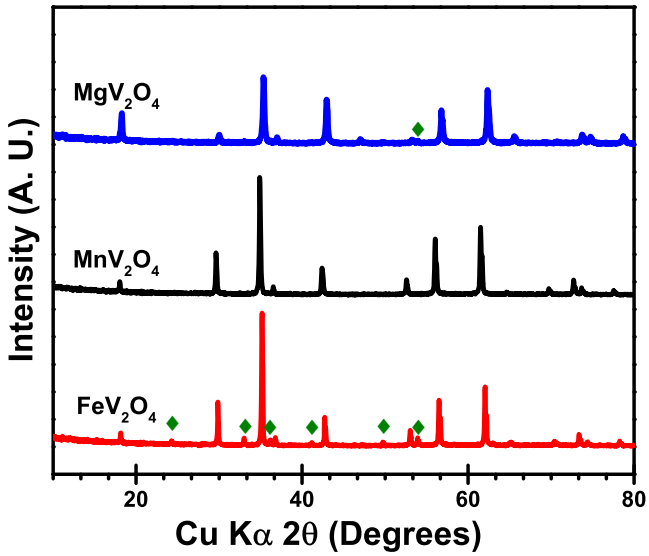

Figure 7.7. XRD patterns of AV_2O_4 (A = Mg, Mn, and Fe) post-heated in argon atmosphere to 900 °C and held for 3 h. The ◆ indicates peaks due to V_2O_3 impurity phase.

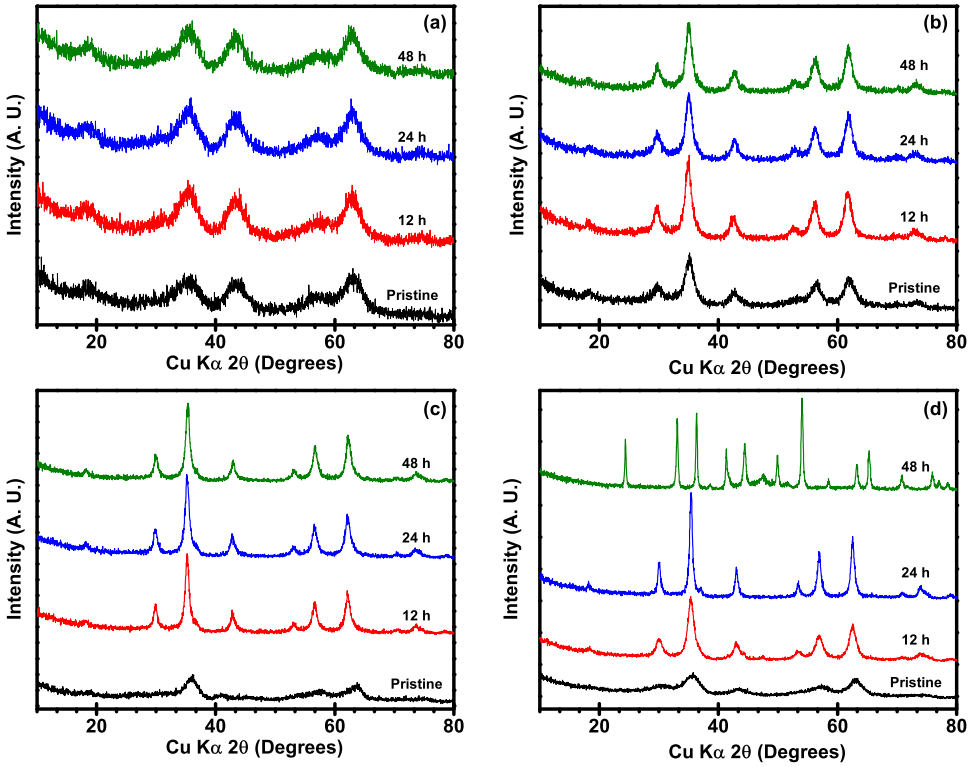

Figure 7.8. XRD patterns of (a) MgV_2O_4, (b) MnV_2O_4, (c) FeV_2O_4, and (d) CoV_2O_4 post-heated to 450 °C in 5% H_2 – 95 % Ar and held for 12, 24, and 48 h. The XRD pattern of the as prepared samples is provided as a reference to the change in crystallinity after post heating.

Additional post-heating experiments were carried out on AV_2O_4 (Mg, Mn, Fe, and Co) under 5 % H_2 – 95 % Ar atmosphere at 450 °C with hold times of 12, 24, and 48 h. The XRD peaks for AV_2O_4 (Mg, Mn, and Fe) did not increase in sharpness by extending the dwell time at 450 °C (Figure 7.8). In contrast, the sharpness of the XRD peaks for the CoV_2O_4 sample held for 12 h did improve as is evidenced by the ability to resolve the (222) peak (36.8°), which is hidden in the broadness of the (311) peak (~ 35°) in both the pristine sample and the sample held for 12 h at 450 °C. CoV_2O_4 breaks down into Co and

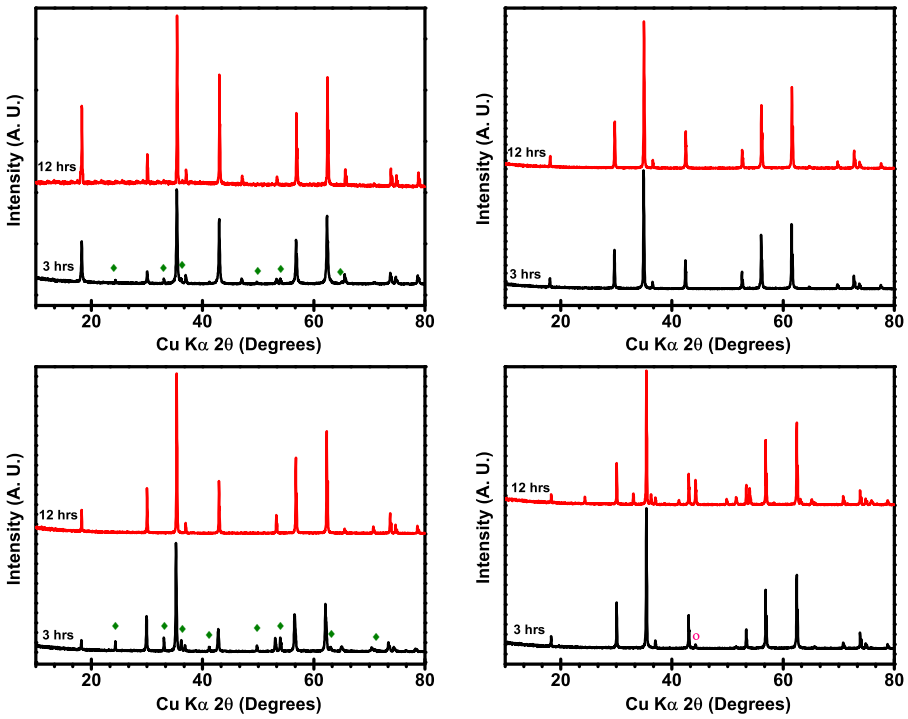

Figure 7.9. XRD patterns of (a) MgV_2O_4, (b) MnV_2O_4, (c) FeV_2O_4, and (d) CoV_2O_4 post-heated to 900 °C in 100 % Ar and held for 3 and 12 h. The ◆ in (a) and (b) indicate V_2O_3 impurity. The o in (d) indicates cobalt impurity.

V_2O_3 upon extending the dwell time to 48 h at 450 °C. The disproportionation of CoV_2O_4 under 5 % H_2 – 95 % Ar atmosphere at 900 °C – 12 h and 450 °C – 48 h suggests the environment is too reducing for Co^{2+} in CoV_2O_4.

In the interest of determining the effect of the atmosphere used in the post-heating step, each of the AV_2O_4 samples was also heated at 900 °C and held for 3 and 12 h under Ar atmosphere (Figure 7.9). The MgV_2O_4 and FeV_2O_4 samples held for 3 h had V_2O_3 impurity phase present as seen in the XRD patterns (Figure 7.9a and 7.9c). The amount of impurity phase present in the Fe sample appears to be greater than that in the Mg sample

(determined by the relative intensities of the peaks). With the loss of V from the FeV_2O_4 phase to form V_2O_3, the sample forms Fe_3O_4 spinel along with FeV_2O_4 spinel. A dwell time of 12 h was needed to obtain pure phase MgV_2O_4 and FeV_2O_4. In contrast, a pure phase MnV_2O_4 sample (Figure 7.9b) was obtained in as little as 3 h at 900 °C in Ar atmosphere. The MnV_2O_4 sample remained pure phase on extending the dwell time to 12 h.

The CoV_2O_4 phase was still present after heating to 900 °C (Figure 7.9d) in argon unlike the total disintegration of the spinel structure into Co and V_2O_3 under H_2 – Ar atmosphere. Nevertheless impurities were still present at both dwell times under argon atmosphere. The sample held for 3 h at the peak temperature had a small amount of Co impurity present. Upon extending the dwell time to 12 h, V_2O_3 precipitated out of the sample and the amount of Co impurity increased. CoV_2O_4 was also heated to 700 °C and 800 °C under argon atmosphere for 3 h in an attempt to avoid the formation of cobalt metal impurity phase, but the impurity phase remained. The results confirm the difficulty of synthesizing CoV_2O_4 at high temperatures because of the ease with which Co^{2+} is reduced to Co metal. This demonstrates the importance of employing a low-temperature synthesis process for CoV_2O_4.

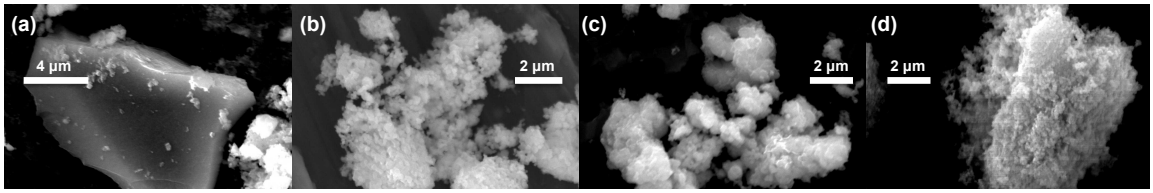

Figure 7.10. SEM images of (a) MgV_2O_4, (b) MnV_2O_4, (c) FeV_2O_4, and (d) CoV_2O_4 post-heated to 900 °C for 12 h.

Figure 7.10 shows the morphology of each of the AV_2O_4 samples post-heated to 900 °C. The Mn, Fe, and Co samples formed into secondary particles made up of the primary particles while the Mg sample formed very large primary particles. The differences in the morphology of the post-heated samples may be caused by the differences in the melting temperature of the A^{2+} cations (Mg: ~ 650 °C vs. Fe, Mn, and Co: > 1200 °C).

7.4 CONCLUSIONS

We have demonstrated the use of a novel microwave-assisted solvothermal process for the synthesis of AV_2O_4 (Mg, Fe, Mn, and Co). This method is remarkably effective in reducing the synthesis time and energy use due to the efficiency of dielectric heating compared to conventional heating, which depends on convective currents and on the thermal conductivity of the constituents involved in the reaction. The ability to access V^{3+} is facilitated by the relative positions of the energy levels of the cations in solution, which is lower than that in the solid, combined with the use of a strong reducing solvent like TEG. The study also demonstrates that some spinel oxides like CoV_2O_4 are unstable at higher temperatures, so the MW-ST method presented here becomes valuable to access such metastable phases. The access to these spinel oxides by the MW-ST process provides an opportunity to tune systematically the V-V distance with solid solutions like $Co_{1-x}A_xV_2O_4$ (A = Mg, Mn, or Fe) with our future work and understand the role of V-V distance on localized to itinerant electron transition.

Chapter 8: Summary

With an aim at developing a fundamental understanding of the factors influencing the electrochemical performance of cathode materials used in lithium-ion batteries, spinel and polyanion cathodes were systematically investigated. The use of a low-temperature microwave-assisted process facilitated the synthesis of metastable phosphate materials for lithium-ion batteries. The low-temperature technique was extended to the synthesis of lower-valent transition-metal oxides that are known to exhibit interesting physical properties.

First, a guide was provided to understand how the $M^{2+/3+}$ redox energies in polyanion cathodes are affected by the inductive effect and through structural features in polyanion compounds. It was determined that the magnitude of the voltages delivered by the polyanion cathodes can be predicted based simply on the coordination of the transition-metal ion. Additionally, it was demonstrated that edge sharing with LiO_4 polyhedra in the silicates raises the $M^{2+/3+}$ redox energy, while edge sharing with PO_4 polyhedra in the phosphates lowers the $M^{2+/3+}$ redox energy. Furthermore, the difference in voltage delivered by the phosphates and pyrophosphates was explained by considering the resonance structures within the polyanion unit and its contribution to the covalency of the polyanion.

Second, a low-temperature microwave-assisted solvothermal process was used to substitute 20 atom % V^{3+} for Mn^{2+} in $LiMnPO_4$. It was shown that the solubility of vanadium in $LiMnPO_4$ decreases upon heating the doped samples to ≥ 575 °C where impurity phases composed of vanadium begin to form, demonstrating the importance of employing a low-temperature process. It was further demonstrated that by increasing the vanadium content in the material, the discharge capacity in the first cycle can be

increased without any additional carbon coating. The discharge capacity was further improved on post-heating (525 °C) the as-prepared sample, possibly due to an improvement in the cation ordering/crystallinity of the sample. Lastly, the overall kinetics of the material was improved by means of lowering the charge-transfer impedance and increasing the lithium-ion diffusion coefficient upon vanadium substitution. Subsequent X-ray absorption spectroscopy data revealed that the better performance was facilitated by enhanced Mn-O hybridization upon incorporating vanadium into the lattice.

Third, several oxy-fluoride spinel cathode samples $Li_{1.1}Mn_{1.8}M_{0.1}O_{4-\delta}F_{\delta}$ and $Li_{1+x}Mn_{2-2x}M_xO_{4-\delta}F_{\delta}$ with M = Al, Ti, Cr, Fe, Co, and Ni were synthesized and characterized with an aim to understand the role of cationic and anionic dopants on the electrochemical performance. The solubility limit of fluorine in the spinel lattice was determined to be ~ 0.2 as LiF begins to form as an impurity at higher fluorine contents. The capacity fade of the material was shown to increase drastically when the Mn valence decreases below ~ 3.6. Furthermore, at a given dopant content of M, the capacity fade was found to decrease with (i) decreasing oxidation state of M^{n+} due to an increase in the Mn oxidation state, (ii) increasing electronegativity of M and decreasing bond dissociation energy of M-O due to the increased metal-oxygen covalence and electronic conductivity, and (iii) decreasing Mn dissolution. The charge-discharge kinetics of the fluorinated samples worsened as the fluorine content increased due to a decreasing metal-oxygen covalence and electronic conductivity caused by the substitution of more electronegative fluorine for oxygen.

Fourth, the effect of the processing route for $Li_{1.1}Mn_{1.8}M_{0.1}O_4$ (M = Al, Cr, Fe, Co, Ni, and Cu) spinel oxides on the surface concentration of M was investigated. It was determined that annealing the samples does not drastically change the M/Mn ratio on the surface, suggesting that the concentration of M is controlled by the tendency to reduce

the surface free energy of the particles (*i.e.*, equilibrium segregation). The extent of surface segregation that occurred during processing was governed by the ionic radius of M, compared to the ionic radius of Mn. Subsequent electrochemical tests suggest that the cycling performance of the samples is better when the M/Mn ratio is closer to the expected bulk value.

Finally, a novel microwave-assisted solvothermal process was used for the synthesis of AV_2O_4 (Mg, Fe, Mn, and Co). The method is remarkably effective in reducing the synthesis time and energy use due to the efficiency of dielectric heating compared to conventional heating, which depends on convective currents and on the thermal conductivity of the constituents involved in the reaction. The ability to access V^{3+} was facilitated by the relative positions of the energy levels of the cations in solution, which is lower than that in the solid, and the use of a strong reducing solvent like TEG. Subsequent post-heating of the samples demonstrated that some spinel oxides like CoV_2O_4 are unstable at higher temperatures, so the microwave-assisted method presented is valuable to access such metastable phases.

The MW-ST process provides an opportunity to tune systematically the V-V distance with solid solutions like $Co_{1-x}A_xV_2O_4$ (A = Mg, Mn, or Fe) with our future work and understand the role of V-V distance on localized to itinerant electron transition. In addition, the MW-ST process can be extended to dope tetravalent cations, such as Ti^{4+}, for Mn in $LiMnPO_4$ to study the effect on the electrochemical performance.

References

1. R. Selim and P. Bro, *Journal of The Electrochemical Society*, 1974, **121**, 1457-1459.
2. V. R. Koch and J. H. Young, *Journal of The Electrochemical Society*, 1978, **125**, 1371-1377.
3. I. Yoshimatsu, T. Hirai and J.-i. Yamaki, *Journal of The Electrochemical Society*, 1988, **135**, 2422-2427.
4. K. Mizushima, P. C. Jones, P. J. Wiseman and J. B. Goodenough, *Solid State Ionics*, 1981, **3–4**, 171-174.
5. D. W. Murphy and P. A. Christian, *Science*, 1979, **205**, 651-656.
6. M. S. Whittingham, *Science*, 1976, **192**, 1126-1127.
7. K. Xu, *Chemical Review*, 2004, **104**, 4304-4417.
8. J. M. Tarascon, *Philosophical transactions. Series A, Mathematical, physical, and engineering sciences*, 2010, **368**, 3227-3241.
9. A. Manthiram and J. B. Goodenough, *Journal of Solid State Chemistry*, 1987, **71**, 349-360.
10. A. Manthiram and J. B. Goodenough, *Journal of Power Sources*, 1989, **26**, 403-408.
11. A. K. Padhi, V. Manivannan and J. B. Goodenough, *Journal of The Electrochemical Society*, 1998, **145**, 1518-1520.
12. A. K. Padhi, K. S. Nanjundaswamy and J. B. Goodenough, *Journal of The Electrochemical Society*, 1997, **144**, 1188-1194.
13. M. M. Thackeray, *Mater. Res. Bull.*, 1982, **17**, 785-793.
14. M. M. Thackeray, W. I. F. David, P. G. Bruce and J. B. Goodenough, *Mater. Res. Bull.*, 1983, **18**, 461-472.
15. M. M. Thackeray, P. J. Johnson, L. A. de Picciotto, P. G. Bruce and J. B. Goodenough, *Mater. Res. Bull.*, 1984, **19**, 179-187.
16. M. M. Thackeray, *Progrees in Solid State Chemistry*, 1997, **25**, 1-71.
17. M. M. Thackeray, *Journal of The Electrochemical Society*, 1995, **142**, 2558-2563.
18. R. Fong, U. von Sacken and J. R. Dahn, *Journal of The Electrochemical Society*, 1990, **137**, 2009-2013.
19. J. Vetter, P. Novák, M. R. Wagner, C. Veit, K. C. Möller, J. O. Besenhard, M. Winter, M. Wohlfahrt-Mehrens, C. Vogler and A. Hammouche, *Journal of Power Sources*, 2005, **147**, 269-281.
20. Z. Chen, Y. Cao, J. Qian, X. Ai and H. Yang, *Journal of Materials Chemistry*, 2010, **20**, 7266.
21. P. Poizot, S. Laruelle, S. Grugeon, L. Dupont and J. M. Tarascon, *Nature*, 2000, **407**, 496-499.
22. R. Marom, S. F. Amalraj, N. Leifer, D. Jacob and D. Aurbach, *Journal of Materials Chemistry*, 2011, **21**, 9938.

23. A. S. Arico, P. G. Bruce, B. Scrosati, J. M. Tarascon and W. V. Schalkwijk, *Nature materials*, 2005, **4**, 366-377.
24. A. Manuel Stephan and K. S. Nahm, *Polymer*, 2006, **47**, 5952-5964.
25. A. Lewandowski and A. Świderska-Mocek, *Journal of Power Sources*, 2009, **194**, 601-609.
26. P. Knauth, *Solid State Ionics*, 2009, **180**, 911-916.
27. P. Arora and Z. Zhang, *Chemical Review*, 2004, **104**, 4419-4462.
28. R. J. Gummow, A. deKock and M. M. Thackeray, *Solid State Ionics*, 1994, **69**, 59-67.
29. D. H. Jang, Y. J. Shin and S. M. Oh, *Journal of The Electrochemical Society*, 1996, **143**.
30. J. M. Paulsen and J. R. Dahn, *Chemistry of Materials*, 1999, **11**, 3065-3079.
31. R. Qiao, T. Chin, S. J. Harris, S. Yan and W. Yang, *Current Applied Physics*, 2013, **13**, 544-548.
32. J. J. Jia, T. A. Callcott, J. Yurkas, A. W. Ellis, F. J. Himpsel, M. G. Samant, J. Stohr, D. L. Ederer, J. A. Carlisle, E. A. Hudson, L. J. Terminello, D. K. Shuh and R. C. C. Perera, *Rev. Sci. Instrum.*, 1995, **66**, 1394-1397.
33. A. R. Armstrong, N. Kuganathan, M. S. Islam and P. G. Bruce, *J Am Chem Soc*, 2011, **133**, 13031-13035.
34. N. Kuganathan and M. S. Islam, *Chemistry of Materials*, 2009, **21**, 5196-5202.
35. C. A. J. Fisher, V. M. H. Prieto and M. S. Islam, *Chemistry of Materials*, 2008, **20**, 5907-5915.
36. V. V. Politaev, A. A. Petrenko, V. B. Nalbandyan, B. S. Medvedev and E. S. Shvetsova, *Journal of Solid State Chemistry*, 2007, **180**, 1045-1050.
37. A. R. Armstrong, C. Lyness, M. Ménétrier and P. G. Bruce, *Chemistry of Materials*, 2010, **22**, 1892-1900.
38. G. Rousse, J. Rodriguez-Carvajal, S. Patoux and C. Masquelier, *Chemistry of Materials*, 2003, **15**, 4082-4090.
39. O. Garcia-Moreno, M. Alvarez-Vega, F. Garcia-Alvarado, J. Garcia-Jaca, J. M. Gallardo-Amores, M. L. Sanjuan and U. Amador, *Chemistry of Materials*, 2001, **13**, 1570-1576.
40. F. Kubel, *Zeitshrift fur Kristallographie*, 1994, **209**, 755.
41. S. Lee and S. S. Park, *Chemistry of Materials*, 2012, **24**, 3550-3557.
42. H. Kim, S. Lee, Y.-U. Park, H. Kim, J. Kim, S. Jeon and K. Kang, *Chemistry of Materials*, 2011, **23**, 3930-3937.
43. L. Adam, A. Guesdon and B. Raveau, *Journal of Solid State Chemistry*, 2008, **181**, 3110-3115.
44. A. K. Padhi, K. S. Nanjundaswamy, C. Masquelier, S. Okada and J. B. Goodenough, *Journal of The Electrochemical Society*, 1997, **144**, 1609.
45. Y. Song, P. Y. Zavalij, M. Suzuki and M. S. Whittingham, *Inorganic chemistry*, 2002, **41**, 5778-5786.
46. M. E. Arroyo-de Dompablo, J. M. Gallardo-Amores and U. Amador, *Electrochemical and Solid-State Letters*, 2005, **8**, A564.

47. A. Manthiram, A. Vadivel Murugan, A. Sarkar and T. Muraliganth, *Energy & Environmental Science*, 2008, **1**, 621.
48. D. Choi, D. Wang, I. T. Bae, J. Xiao, Z. Nie, W. Wang, V. V. Viswanathan, Y. J. Lee, J. G. Zhang, G. L. Graff, Z. Yang and J. Liu, *Nano letters*, 2010, **10**, 2799-2805.
49. K. Amine, H. Yasuda and M. Yamachi, *Electrochem. Solid State Lett.*, 2000, **3**, 178-179.
50. J. Wolfenstine and J. Allen, *Journal of Power Sources*, 2004, **136**, 150-153.
51. F. Zhou, M. Cococcioni, K. Kang and G. Ceder, *Electrochemistry Communications*, 2004, **6**, 1144-1148.
52. A. Yamada, N. Iwane, Y. Harada, S. Nishimura, Y. Koyama and I. Tanaka, *Advanced materials*, 2010, **22**, 3583-3587.
53. J. C. Kim, C. J. Moore, B. Kang, G. Hautier, A. Jain and G. Ceder, *Journal of The Electrochemical Society*, 2011, **158**, A309.
54. V. Legagneur, Y. An, A. Mosbah, R. Portal, A. Le Gal La Salle, A. Verbaere, D. Guyomard and Y. Piffard, *Solid State Ionics*, 2001, **139**, 37-46.
55. D.-H. Seo, Y.-U. Park, S.-W. Kim, I. Park, R. A. Shakoor and K. Kang, *Physical Review B*, 2011, **83**.
56. S.-i. Nishimura, M. Nakamura, R. Natsui and A. Yamada, *Journal of The American Chemical Society*, 2010, **132**, 13596-13597.
57. M. Tamaru, P. Barpanda, Y. Yamada, S.-i. Nishimura and A. Yamada, *Journal of Materials Chemistry*, 2012, **22**, 24526.
58. C. Sirisopanaporn, C. Masquelier, P. G. Bruce, A. R. Armstrong and R. Dominko, *J Am Chem Soc*, 2011, **133**, 1263-1265.
59. R. Dominko, *Journal of Power Sources*, 2008, **184**, 462-468.
60. C. Lyness, B. Delobel, A. R. Armstrong and P. G. Bruce, *Chemical Communications*, 2007, 4890.
61. A. Nyten, S. Kamali, L. Haggstrom, T. Gustafsson and J. O. Thomas, *Journal of Materials Chemistry*, 2006, **16**, 2266.
62. S. Aono, T. Tsurudo, K. Urita and I. Moriguchi, *Chem Commun (Camb)*, 2013, **49**, 2939-2941.
63. Z. L. Gong, Y. X. Li and Y. Yang, *Journal of Power Sources*, 2007, **174**, 524-527.
64. M. E. Arroyo-de Dompablo, M. Armand, J. M. Tarascon and U. Amador, *Electrochemistry Communications*, 2006, **8**, 1292-1298.
65. M. S. Islam, R. Dominko, C. Masquelier, C. Sirisopanaporn, A. R. Armstrong and P. G. Bruce, *Journal of Materials Chemistry*, 2011, **21**, 9811.
66. L.-X. Yuan, Z.-H. Wang, W.-X. Zhang, X.-L. Hu, J.-T. Chen, Y.-H. Huang and J. B. Goodenough, *Energy & Environmental Science*, 2011, **4**, 269.
67. N. Furuta, S.-i. Nishimura, P. Barpanda and A. Yamada, *Chemistry of Materials*, 2012, **24**, 1055-1061.
68. M. S. Islam, D. J. Driscoll, C. A. J. Fisher and P. R. Slater, *Chemistry of Materials*, 2005, **17**, 5085-5092.

69. Y. Z. Dong, Y. M. Zhao, Z. D. Shi, X. N. An, P. Fu and L. Chen, *Electrochimica Acta*, 2008, **53**, 2339-2345.
70. C. J. Malerich, *Journal of Chemical Education*, 1987, **64**, 403.
71. R. J. P. Corriu, C. Guerin, B. J. L. Henner and W. W. C. Wong Chi Man, *Organometallics*, 1988, **7**, 237-238.
72. J. Klebe, *Journal of The American Chemical Society*, 1968, **90**, 5246-5251.
73. J. Hinze, M. A. Whitehead and H. H. Jaffe, *Journal of The American Chemical Society*, 1963, **85**, 148-154.
74. R. G. Pearson and J. Songstad, *Journal of The American Chemical Society*, 1967, **89**, 1827-1836.
75. T. Muraliganth and A. Manthiram, *Journal of Physical Chemistry C*, 2010, **114**, 15530-15540.
76. J. J. Zuckerman, *Journal of Chemical Education*, 1965, **42**, 315-317.
77. A. Hauser, *Advances in Polymer Science*, 2004, **233**, 49-58.
78. H. Huang, S. C. Yin and L. F. Nazar, *Electrochemical and Solid-State Letters*, 2001, **4**, A170.
79. A. Yamada, S. C. Chung and K. Hinokuma, *Journal of The Electrochemical Society*, 2001, **148**, A224.
80. S. Y. Chung, J. T. Bloking and Y. M. Chiang, *Nature materials*, 2002, **1**, 123-128.
81. P. S. Herle, B. Ellis, N. Coombs and L. F. Nazar, *Nature materials*, 2004, **3**, 147-152.
82. K. Zaghib, A. Mauger, J. B. Goodenough, F. Gendron and C. M. Julien, *Chemistry of Materials*, 2007, **19**, 3740-3747.
83. X. J. Chen, G. S. Cao, X. B. Zhao, J. P. Tu and T. J. Zhu, *Journal of Alloys and Compounds*, 2008, **463**, 385-389.
84. C.-Y. Chiang, H.-C. Su, P.-J. Wu, H.-J. Liu, C.-W. Hu, N. Sharma, V. K. Peterson, H.-W. Hsieh, Y.-F. Lin, W.-C. Chou, C.-H. Lee, J.-F. Lee and B.-Y. Shew, *The Journal of Physical Chemistry C*, 2012, **116**, 24424-24429.
85. K. L. Harrison, C. A. Bridges, M. P. Paranthanam, C. U. Segre, J. Katsoudas, V. A. Maroni, J. C. Idrobo, J. B. Goodenough and A. Manthiram, *Chemistry of Materials*, 2013, **25**, 768-781.
86. J. Hong, C. S. Wang, X. Chen, S. Upreti and M. S. Whittingham, *Electrochemical and Solid-State Letters*, 2009, **12**, A33.
87. J. Ma, B. Li, H. Du, C. Xu and F. Kang, *Journal of The Electrochemical Society*, 2011, **158**, A26.
88. F. Omenya, N. A. Chernova, S. Upreti, P. Y. Zavalij, K.-W. Nam, X.-Q. Yang and M. S. Whittingham, *Chemistry of Materials*, 2011, **23**, 4733-4740.
89. F. Omenya, N. A. Chernova, Q. Wang, R. Zhang and M. S. Whittingham, *Chemistry of Materials*, 2013, **25**, 2691-2699.
90. M. Wagemaker, B. L. Ellis, D. Lutzenkirchen-Hecht, F. M. Mulder and L. F. Nazar, *Chemistry of Materials*, 2008, **20**, 6313-6315.
91. G. Yang, C. Jiang, X. He, J. Ying and F. Cai, *Ionics*, 2011, **18**, 59-64.

92. L.-L. Zhang, G. Liang, A. Ignatov, M. C. Croft, X.-Q. Xiong, I. M. Hung, Y.-H. Huang, X.-L. Hu, W.-X. Zhang and Y.-L. Peng, *The Journal of Physical Chemistry C*, 2011, **115**, 13520-13527.
93. C. S. Sun, Z. Zhou, Z. G. Xu, D. G. Wang, J. P. Wei, X. K. Bian and J. Yan, *Journal of Power Sources*, 2009, **193**, 841-845.
94. G. Chen, A. K. Shukla, X. Song and T. J. Richardson, *Journal of Materials Chemistry*, 2011, **21**, 10126.
95. C. Delacourt, L. Laffont, R. Bouchet, C. Wurm, J. B. Leriche, M. Morcrette, J. M. Tarascon and C. Masquelier, *Journal of The Electrochemical Society*, 2005, **152**, A913.
96. V. Aravindan, J. Gnanaraj, Y.-S. Lee and S. Madhavi, *Journal of Materials Chemistry A*, 2013, **1**, 3518.
97. G. Chen, J. D. Wilcox and T. J. Richardson, *Electrochemical and Solid-State Letters*, 2008, **11**, A190.
98. J.-W. Lee, M.-S. Park, B. Anass, J.-H. Park, M.-S. Paik and S.-G. Doo, *Electrochimica Acta*, 2010, **55**, 4162-4169.
99. T. Shiratsuchi, S. Okada, T. Doi and J.-i. Yamaki, *Electrochimica Acta*, 2009, **54**, 3145-3151.
100. K. L. Harrison and A. Manthiram, *Chemistry of Materials*, 2013, 130402103645008.
101. K. L. Harrison and A. Manthiram, *Inorganic chemistry*, 2011, **50**, 3613-3620.
102. L. Qiao, H. Y. Xiao, S. M. Heald, M. E. Bowden, T. Varga, G. J. Exarhos, M. D. Biegalski, I. N. Ivanov, W. J. Weber, T. C. Droubay and S. A. Chambers, *Journal of Materials Chemistry C*, 2013, **1**, 4527.
103. T. Yamamoto, *X-Ray Spectrometry*, 2008, **37**, 572-584.
104. H. T. Kuo, N. C. Bagkar, R. S. Liu, C. H. Shen, D. S. Shy, X. K. XIng, J. F. Lee and J. M. Chen, *Journal of Physical Chemistry B*, 2008, **112**, 11250-11257.
105. J. Wong, R. P. Messmer and D. H. Maylotte, *Physical Review B*, 1984, **30**, 5596-5610.
106. S. K. Martha, J. Grinblat, O. Haik, E. Zinigrad, T. Drezen, J. H. Miners, I. Exnar, A. Kay, B. Markovsky and D. Aurbach, *Angewandte Chemie*, 2009, **48**, 8559-8563.
107. D. Wang, C. Ouyang, T. Drézen, I. Exnar, A. Kay, N.-H. Kwon, P. Gouerec, J. H. Miners, M. Wang and M. Grätzel, *Journal of The Electrochemical Society*, 2010, **157**, A225.
108. D. Morgan, A. Van der Ven and G. Ceder, *Electrochemical and Solid-State Letters*, 2004, **7**, A30.
109. P. Gibot, M. Casas-Cabanas, L. Laffont, S. Levasseur, P. Carlach, S. Hamelet, J. M. Tarascon and C. Masquelier, *Nature materials*, 2008, **7**, 741-747.
110. J. Xu, G. Chen, Y.-J. Teng and B. Zhang, *Solid State Communications*, 2008, **147**, 414-418.
111. N. Meethong, Y.-H. Kao, S. A. Speakman and Y.-M. Chiang, *Advanced Functional Materials*, 2009, **19**, 1060-1070.

112. Y. Zhu, Y. Xu, Y. Liu, C. Luo and C. Wang, *Nanoscale*, 2013, **5**, 780-787.
113. V. Ramar and P. Balaya, *Physical chemistry chemical physics : PCCP*, 2013, **15**, 17240-17249.
114. X. Liu, J. Liu, R. Qiao, Y. Yu, H. Li, L. Suo, Y. S. Hu, Y. D. Chuang, G. Shu, F. Chou, T. C. Weng, D. Nordlund, D. Sokaras, Y. J. Wang, H. Lin, B. Barbiellini, A. Bansil, X. Song, Z. Liu, S. Yan, G. Liu, S. Qiao, T. J. Richardson, D. Prendergast, Z. Hussain, F. M. de Groot and W. Yang, *J Am Chem Soc*, 2012, **134**, 13708-13715.
115. F. de Groot and A. Kotani, *Core Level Spectroscopy of Solids*, CRC Press Taylor & Francis Group, Boca Raton, FL, USA, 2008.
116. C. Delacourt, A. Kwong, X. Liu, R. Qiao, W. L. Yang, P. Lu, S. J. Harris and V. Srinivasan, *Journal of the Electrochemical Society*, 2013, **160**, A1099-A1107.
117. N. P. W. Pieczonka, Z. Liu, P. Lu, K. L. Olson, J. Moote, B. R. Powell and J.-H. Kim, *The Journal of Physical Chemistry C*, 2013, **117**, 15947-15957.
118. Y. Talyosef, B. Markovsky, G. Salitra, D. Aurbach, H. J. Kim and S. Choi, *Journal of Power Sources*, 2005, **146**, 664-669.
119. D. Aurbach, B. Markovsky, Y. Talyossef, G. Salitra, H.-J. Kim and S. Choi, *Journal of Power Sources*, 2006, **162**, 780-789.
120. F. de Groot, M. Grioni, J. Fuggle, J. Ghijsen, G. Sawatzky and H. Petersen, *Physical Review B*, 1989, **40**, 5715-5723.
121. H. Huang, C. A. Vincent and P. G. Bruce, *Journal of the Electrochemical Society*, 1999, **146**, 3649-3654.
122. M. M. Thackeray, Y. Shao-Horn, A. J. Kahaian, K. D. Kepler, J. T. Vaughey and S. A. Hackney, *Electrochem. Solid State Lett.*, 1998, **1**, 7-9.
123. H. Yamane, T. Inoue, M. Fujita and M. Sano, *Journal of Power Sources*, 2001, **99**, 60-65.
124. A. Manthiram, J. Choi and W. Choi, Factors limiting the electrochemical performance of oxide cathodes, 2006.
125. Y. J. Shin and A. Manthiram, *Journal of Power Sources*, 2004, **126**, 169-174.
126. Y. J. Shin and A. Manthiram, *Journal of the Electrochemical Society*, 2004, **151**, A204-A208.
127. J. M. Tarascon, E. Wang, F. K. Shokoohi, W. R. McKinnon and S. Colson, *Journal of The Electrochemical Society*, 1991, **138**, 2859-2864.
128. G. Pistoia, A. Antonini and R. Rosati, *Chemistry of Materials*, 1997, **9**, 1443-1450.
129. L. Guohua, H. Ikuta, T. Uchida and M. Wakihara, *Journal of The Electrochemical Society*, 1996, **143**, 178-182.
130. Y. Gao and J. R. Dahn, *Journal of The Electrochemical Society*, 1996, **143**, 100-114.
131. Q. Luo and A. Manthiram, *Journal of The Electrochemical Society*, 2009, **156**, A84.
132. W. Choi and A. Manthiram, *Electrochemical and Solid-State Letters*, 2006, **9**, A245.

133. K. E. Sickafus, J. M. Wills and N. W. Grimes, *Journal of The American Chemical Society*, 1999, **82**, 3279-3292.
134. J. Liu and A. Manthiram, *Journal of Physical Chemistry C*, 2009, **113**, 15073-15079.
135. D. W. Shin, C. A. Bridges, A. Huq, M. P. Paranthaman and A. Manthiram, *Chemistry of Materials*, 2012, **24**, 3720-3731.
136. K. R. Chemelewski, W. Li, A. Gutierrez and A. Manthiram, *Journal of Materials Chemistry A*, 2013, **1**, 15334.
137. A. P. Nayak, A. Dolocan, J. Lee, H.-Y. Chang, T. Pandhi, M. Holt, L. I. Tao and D. Akinwande, *Nano*, 2013, 1450002.
138. R. G. Faulkner, *Journal of Materials Science* 1981, **16**, 373-383.
139. J. Nowotny, C. C. Sorrell and T. Bak, *Surface and Interface Analysis*, 2005, **37**, 316-324.
140. D. R. Harries and A. D. Marwick, *Philosophical Transactions of the Royal Society A: Mathematical, Physical and Engineering Sciences*, 1980, **295**, 197-207.
141. A. Manthiram and J. B. Goodenough, *Canadian Journal of Physics*, 1987, **65**, 1309-1317.
142. Y. Kato, G.-W. Chern, K. A. Al-Hassanieh, N. B. Perkins and C. D. Batista, *Physical Review Letters*, 2012, **108**.
143. S. H. Baek, K. Y. Choi, A. P. Reyes, P. L. Kuhns, N. J. Curro, V. Ramanchandran, N. S. Dalal, H. D. Zhou and C. R. Wiebe, *Journal of Physics: Condensed Matter*, 2008, **20**, 135218.
144. S. G. Ebbinghaus, J. Hanss, M. Klemm and S. Horn, *Journal of Alloys and Compounds*, 2004, **370**, 75-79.
145. A. Kismarahardja, J. S. Brooks, H. D. Zhou, E. S. Choi, K. Matsubayashi and Y. Uwatoko, *Physical Review B*, 2013, **87**.
146. S. Komarneni, *Current Science*, 2003, **85**, 1730-1734.
147. V. Polshettiwar, M. N. Nadagouda and R. S. Varma, *Australian Journal of Chemistry*, 2009, **62**, 16-26.
148. K. J. Rao, B. Vaidhyanathan, M. Ganguli and P. A. Ramakrishnan, *Chemistry of Materials*, 1999, **11**, 882-895.
149. C. Leonelli and W. Lojkowski, *Chemistry Today*, 2007, **25**, 34-38.
150. S. Balaji, D. Mutharasu, N. Sankara Subramanian and K. Ramanathan, *Ionics*, 2009, **15**, 765-777.
151. C. Nethravathi and M. Rajamathi, *Carbon*, 2008, **46**, 1994-1998.
152. I. Bilecka and M. Niederberger, *Nanoscale*, 2010, **2**, 1358.
153. T. Muraliganth, A. V. Murugan and A. Manthiram, *Journal of Materials Chemistry*, 2008, **18**, 5661.
154. T. Muraliganth, K. R. Stroukoff and A. Manthiram, *Chemistry of Materials*, 2010, **22**, 5754-5761.
155. A. Vadivel Murugan, T. Muraliganth and A. Manthiram, *Journal of The Electrochemical Society*, 2009, **156**, A79.

156. Z. Moorhead-Rosenberg, K. L. Harrison, T. Turner and A. Manthiram, *Inorganic chemistry*, 2013, **52**, 13087-13093.
157. M. Baghbanzadeh, L. Carbone, P. D. Cozzoli and C. O. Kappe, *Angewandte Chemie*, 2011, **50**, 11312-11359.
158. X.-H. Liao, J.-J. Zhu, J.-Z. Xu, H.-Y. Chen and J.-M. Zhu, *Chemical Communications*, 2001, 937-938.
159. X. Liao, J. Zhu, W. Zhong and H.-Y. Chen, *Materials Letters*, 2001, **50**, 341-346.
160. S. H. Jhung, T. Jin, Y. K. Hwang and J. S. Chang, *Chemistry*, 2007, **13**, 4410-4417.
161. D. P. Serrano, M. A. Uguina, R. Sanz, E. Castillo, A. Rodrı´guez and P. Sánchez, *Microporous and Mesoporous Materials*, 2004, **69**, 197-208.

Vita

Arturo Gutierrez was born in 1978 in Texas. He served in the U.S. Army as a Radio and Communications Repairman from 1997-99. He received his B.S. degree in Materials Science and Engineering from Boise State University in 2009. He entered the Graduate School at The University of Texas at Austin in June 2009.

Email Address: arturogutierrez7@utexas.edu

This dissertation was typed by the author.